Probe of Coherent and Quantum States in Narrow-Gap Based Semiconductors in the Presence of Strong Spin-Orbit Coupling

Matthew A. Frazier

Dissertation submitted to the Faculty of the

Virginia Polytechnic Institute and State University

in partial fulfillment of the requirements for the degree of

Doctor of Philosophy

in

Physics

Giti A. Khodaparast

James R. Heflin

Rahul Kulkarni

Jean Heremans

September 3 2010

Blacksburg, Virginia

Keywords: Circular photo-galvanic effect, Magneto-optical Kerr effect, Spin polarized current, Narrow gap semiconductors

Probe of Coherent and Quantum States in Narrow-Gap Based Semiconductors in the Presence of Strong Spin-Orbit Coupling

Matthew A. Frazier

(ABSTRACT)

The goal of this project was to study some unexplored optical and magneto-optical properties of the newest member of III-V ferromagnetic structures, InMnSb, as well as InSb films and InSb/AlInSb quantum wells. The emphasis was on dynamical aspects such as charge and spin dynamics in order to address several important issues of the spin-related phenomena. The objectives in this project were to: 1) understand charge/spin dynamics in NGS with different confinement potentials, 2) study phenomena such as interband photo-galvanic effects, in order to generate spin polarized current, 3) probe the effect of magnetic impurities on the spin/charge dynamics. This thesis describes three experiments: detection and measurement of spin polarized photocurrents in InSb films and quantum wells arising from the circular photogalvanic effect, and measurements of the carrier and spin relaxation in InSb and InMnSb structures by magneto-optical Kerr effect and differential transmission. The samples for our studies have been provided by Prof. Heremans at Virginia Tech, Prof. Santos at the University of Oklahoma, and Prof. Furdyna at the University of Notre Dame.

This work received support from the National Science Foundation, the Air Force Office of Scientific Research, Advance VT, and Jeffress Trust Fund.

Acknowledgments

I would like to thank my advisor, Prof. Giti Khodaparast, for being a driving force behind this work, keeping me focused on completing this dissertation, giving advice and guidance and assistance, teaching me to be a good researcher. I would also like to thank my other committee members, Prof. Jean Heremans, Prof. Rahul Kulkarni, and Prof. Randy Heflin, for their time, effort, and assistance throughout my research effort. I am grateful to have worked in a wonderful group; my thanks goes to Dr. Rajeev Kini, for working with me through portions of my experiments, being a great teacher and collaborator, and to Kanokwan Nontapot, Aliya Gifford, Travis Merritt, and Mithun Bhowmick, for their cherished friendship and invaluable assistance as fellow group members.

I am thankful for the assistance of Christa Thomas, for being supportive and helpful and for guiding me through the necessary steps to graduate. Many thanks to Melvin Shaver, Scott Allen, John Miller and all of the staffs from the machine shop for their assistances in building many necessary parts and for letting me borrow their tools and knowledge. Also, many thanks to the physics department faculty and staff for the wonderful environment

in which I learned and researched. Many many thanks to my wonderful family, for all of their love, support, and patience. Without them, I would not be where I am now, and I am very blessed and grateful to have them. Thanks to all of my friends, fellow graduate students who have endured and survived with me and given me wonderful memories. Finally, this project would not have been possible without the financial support received from the National Science Foundation, the Air Force Office of Scientific Research, Advance VT, and Jeffress Trust Fund. For their support, I am grateful.

Contents

List of Figures

List of Tables

Chapter 1

Introduction

1.1 Overview

Semiconductor based information-processing devices have been among the most complex high-performance structures. The advancement of electronics has been focused on making faster, more dense structures in order to represent information as currents, using the spatial degrees of freedom and charge of electrons. Alternative methods of information processing such as metallic spintronic devices used as hard disk read heads and magnetic random access memory (MRAM) were examples of the most successful technological advances of the past decade [1, 2, 3]. The spin degree of freedom was largely ignored, until the discovery of the Giant Magneto-Resistance (GMR) and the eventual development of GMR-based devices [2, 4]. GMR devices work by changing the alignment of spins in ferromagnetic materials,

which changes the spin-dependent scattering, changing the resistance from low (parallel spins) to high (anti-parallel) and vice versa. The GMR effect arises from the imbalance of the spin population at the Fermi energy in ferromagnetic materials, due to the density of states being shifted relative to each other; this results in a polarization of electrons at the Fermi surface [2, 4].

Semiconductor Spintronic device physics has been developing along a similar path to the metallic Spintronics and has demonstrated remarkable success in the past decade [5, 6]. Ferromagnetic and Narrow Gap Semiconductors (NGS) are two important structures in developing spin based devices and spin polarized sources [7, 8, 9]. One of the most direct and powerful methods of generating and probing the spin polarization is optical manipulation. Recently, there have been several studies on ultrafast spin dynamics in ferromagnets such as nickel, cobalt, iron, and CoPt3 [11, 12, 13] but only few time-dependent optical studies of (III,Mn)V ferromagnets and InSb based NGS have been reported.

The goal of this project was to study some unexplored optical and magneto-optical properties of the newest member of III-V ferromagnetic structures, InMnSb, as well as InSb films and InSb/AlInSb quantum wells. The emphasis was on dynamical aspects such as charge and spin dynamics in order to address several important issues of the spin-related phenomena. The objectives in this project were to: 1) understand charge/spin dynamics in NGS with different confinement potentials, 2) study phenomena such as interband photo-galvanic effects, in order to generate spin polarized current, 3) probe the effect of magnetic impurities on the spin/charge dynamics.

For many years, InSb has been considered an ideal narrow-gap semiconductor. It was first recognized by Kane [10] that the small band gap in this material resulted in strong non-parabolicity in the dispersion relation. There have been numerous experimental and theoretical works to explore the characteristics of bulk InSb. Since the proposal by Datta and Das [7] of a spin transistor based on spin precession controlled by an external electric field via Spin-Orbit (SO) coupling, and in light of the current interest in spin-related phenomena, there has been growing activity in understanding and manipulating SO interactions in NGS structures. In particular, spin splitting in heterostructures caused by bulk inversion asymmetry (BIA – the Dresselhaus splitting [19]) and structural inversion asymmetry (SIA – often called the Rashba splitting)[17] has attracted much attention.

The significance of this work stems from the synergy between semiconductor epitaxy and characterization of optical and magneto-optical properties of unique and less explored NGS systems where strong SO interaction plays an important role. The impacts of the research activities can help in a better understanding of the quantum states and dynamics of confined, or strongly driven electrons in semiconductor structures with strong SO interaction.

The chapters of this dissertation are organized according to the measurements they present. Different spin relaxation mechanisms that are important in NGS systems as well as Magneto-Optical Kerr Effect (MOKE) are discussed in Chapter 2. Chapter 3 presents the experimental methods utilized in the generation of spin-polarized currents in InSb based structures and Chapter 4 covers the differential transmission measurements in these material systems. The samples for this work have been provided by groups of Prof. Furdyna (Univ. of Notre Dame),

Prof. Santos (Univ. Of Oklahoma), and Prof. Heremans (Virginia Tech.).

The studied pursued in this work have been published in the following journals:

1- M. Frazier, J. G. Cates, J. A. Waugh, J. J. Heremans, M. B. Santos, X. Liu, and G. A. Khodaparst," Photoinduced spin-polarized current in InSb -based structures, J. App. Phys. 106, 103513 (2009).

2- **Invited Paper**: Giti A. Khodaparast, M. Bhowmick, Matthew Frazier, Rajeev N. Kini, Kanowkan Nontapot, Tetsuya D. Mishima, Michael B. Santos, Bruce W. Wessels, Probe of Coherent and Quantum States in Narrow-Gap Semiconductors in the presence of strong Spin-Orbit Coupling. Proceedings of SPIE Vol. 7608, 76080O (2010).

3- M. Frazier, Nontapot K., Kini R., Khodaparast G. A., Wojtowicz T., Liu X., Furdyna J. K," Time Resolved Magneto-Optical Studies of Ferromagnetic InMnSb Films", Appl. Phys. Lett., 92, 061911 (2008).

4- G. A. Khodaparast., R. N. Kini, K. Nontapot., M. Frazier, E. C. Wade, J. J. Heremans, S. J. Chung, N. Goel, M. B. Santos, T. Wojtowicz, X. Liu, J. K. Furdyna "Control and Probe of Carrier and Spin Relaxations in InSb-Based Structures", Springer Proc. Phys. Series, 13th Intern. Conf. of NGS. P15-18 (2008).

1.2 Summary of Chapter 2

Spin-orbit interaction caused by structural inversion asymmetry leads to spin splitting even without an applied magnetic field, making NGS structures important for developing spin-based devices. One can take advantage of subband splitting in k-space to study phenomena such as the spin-galvanic effect (SGE) and the circular photo-galvanic effect (CPGE)[1], which generate spin polarized current via two different microscopic mechanisms. In the (CPGE), spin photocurrents are generated by optical excitation with circularly polarized light. The photon angular momentum transfers into the directed motion of a free carrier. The combination of spin splitting and the optical selection rules results in an unbalanced occupation of the k+ and k- states and therefore generates a spin-polarized current, as we will show in Fig. 1.1a. The current direction depends on the polarity of the circularly polarized light. The microscopic origin of the spin galvanic current (SGE) is asymmetric spin-flip relaxation of spin-polarized electrons in systems with bulk or structural inversion asymmetry, as illustrated in Fig. 1.1b. If one spin subband is preferentially occupied, asymmetric spin-flip scattering results in a current which in this case is in the x direction.

In Chapter 2, experiments measuring the CPGE-generated spin current were performed on InSb/GaAs and InSb/InP, and InSb quantum wells that were symmetrically- and asymmetrically doped. Generation of the CPGE photocurrent was through optical excitation with light from a Ti-sapphite laser, with the polarization adjusted by passage through a photo-elastic modulator. This allowed us to measure the photocurrent as a function of the

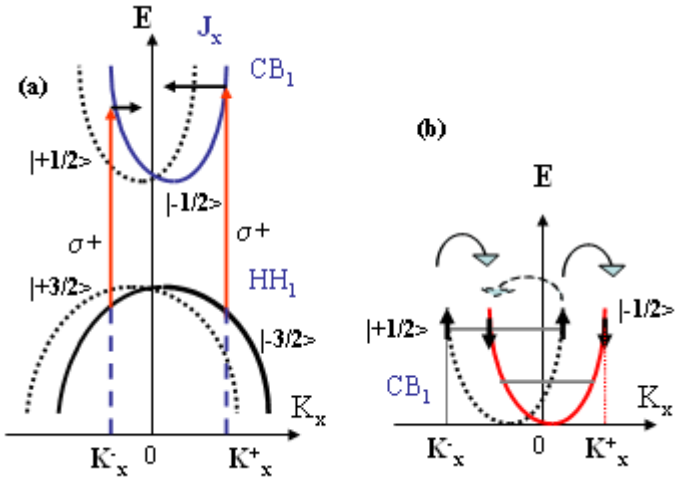

Figure 1.1: Microscopic pictures: a) The interband circular photo-galvanic effect: spin splitting and optical selection rules lead to unbalanced occupation of k_+ and k_- states, resulting in a spin polarized current . b) The spin galvanic effect: after inter-subband excitation, the non-equilibrium distribution of electrons in CB2 relaxes quickly due to phonon emission, and a current can be caused by asymmetric spin-flip scattering in CB1. The arrows show several possible spin-flip scattering.

retardation induced by the PEM. Measurement of the photocurrent was through electrical contacts on the surface of the samples, with the current amplified by a current amplifier and detected by a lock-in amplifier. Due to symmetry arguments, CPGE is not expected in bulk InSb; however, uniaxial strain breaks the symmetry and allows CPGE; the thin films tested had differing amounts of strain, and both showed photocurrent. The symmetry breaking in the quantum wells also allowed CPGE; a spin current was expected and observed in the asymmetric quantum well, but not in the symmetric well.

1.3 Summary of Chapter 3

As the switching rates in electronic and optoelectronic devices are pushed to higher frequencies, it is crucial to probe carrier dynamics in semiconductors on femtosecond time-scales. Understanding the dynamical behavior of nonequilibrium carriers created by intense laser pulses can provide important information about different scattering mechanisms. Time resolved spectroscopy will allow us to understand the relaxation of photoexcited carriers after the initial photoexcitation, where the nonequilibrium population of electrons and holes relax by a series of of scattering processes including carrier-carrier and carrier-phonon scattering. The reported carrier scattering rates in semiconductors range from a few to thousands of femtoseconds.

In Chapter 3 several differential transmission schemes to probe carrier/spin dynamics in the InSb films will be presented. As an example, Figure 1.2 demonstrates the schematic diagram

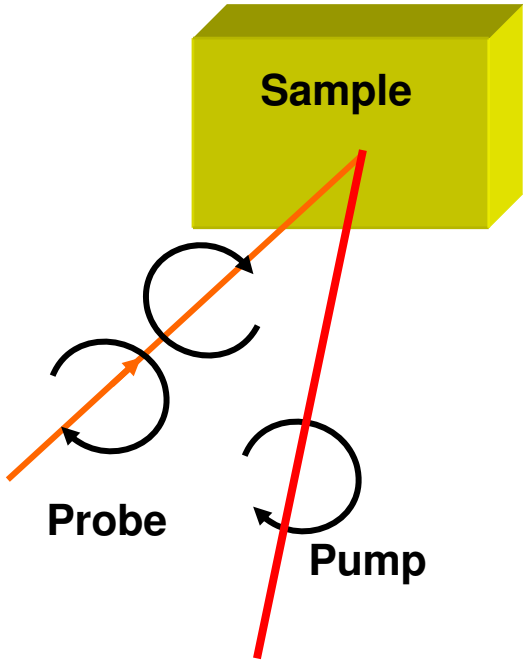

Figure 1.2: Polarization Resolved Differential Transmission measures the change in Transmission when pump and probe have same and opposite polarizations.

of polarization resolved differential transmission where spin polarization can be measured.

1.4 Summary of Chapter 4

Chapter 4 consists of a basic review of spin polarization and relaxation mechanisms. Two methods by which photo-excited spins possibly can relax: Elliot-Yafet (E-Y) [12] and D'yakonov-Perel (D-P) [16] are presented. In E-Y, the wavefunctions are linear combinations of the spin eigenstates, allowing scattering interactions to flip the spin orientation with nonzero probability. E-Y is important for materials with large spin splitting, as the relaxation time

increases as the the spin splitting increases. In D-P, inversion asymmetry of the material lifts the spin degeneracy, acting as an effective, k-dependent magnetic field about which the spins precess. Momentum scattering changes k, which changes the field about which the spins precess, leading to spin dephasing. The inversion asymmetry arises in two forms: bulk inversion asymmetry (BIA), and structure inversion asymmetry (SIA).

One means to determine the spin relaxation of photo-excited carriers is to measure the Kerr rotation. As shown in Fig. 1, the Kerr rotation is the change in the polarization of light upon reflection from a material possessing a magnetization. The Kerr rotation arises from the different optical coefficients for left-handed and right-handed circularly polarized lights. In Chapter 4, MOKE on three InMnSb films with different growth conditions and Mn concentrations are presented.

The $In_{1-x}Mn_xSb$ films, for this study, were grown using an MBE system at the University of Notre Dame. To avoid the large parallel conductance that occurs in thick InSb buffers grown at high temperature, the growth was performed on closely lattice matched (001) hybrid CdTe/GaAs substrates grown by MBE at the Institute of Physics of the Polish Academy of Sciences (group of Prof. Wojtowicz) prior to film deposition. In addition, a 100 nm low-temperature InSb buffer layer was grown at 210 °C, which provided a flat substrate surface with improved lattice matching for subsequent deposition. The substrate was then cooled to 170 °C for the growth of a 230-nm-thick LT-$In_{1-x}Mn_xSb$ (x¡0.03). The samples provided for this project are p-type ferromagnetic structures with hole densities of $1 - 2x10^{19}cm^{-3}$ and Curie temperatures of $\sim$ 9 K.

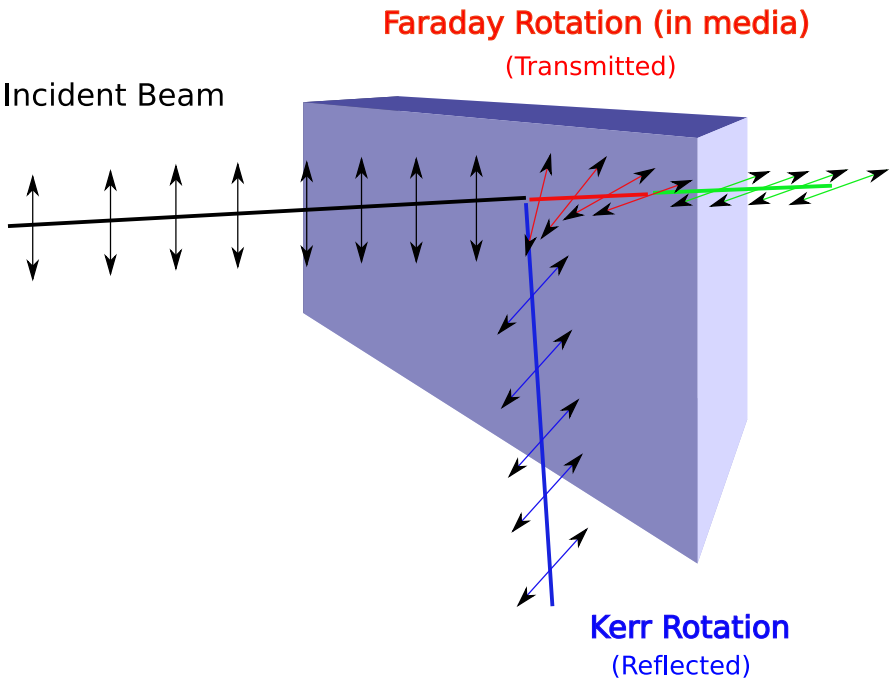

Figure 1.3: Rotation of polarization of light transmitted (Faraday) and reflected (Kerr) from a material. For transmitted light, The plane of polarization is rotated through an angle dependent on field strength and path length through the material. Reflected light experiences a Kerr rotation analogous to the Faraday rotation.

We investigated the effect of magnetic ordering on the MOKE response, by aligning the magnetic moments of the sample with an external magnetic field and comparing the resultant measurements to an earlier case, where the Mn ions were randomly oriented. Our measurements showed no change in the relaxation due to aligning the magnetic field, as well as no temperature dependence; instead, we uncovered a wavelength dependence in the carrier relaxation. Our measurements were motivated by earlier work by Nontapot *et al.* [14] indicating the absence of a strong temperature dependence in the spin relaxation of

the ferromagnetic InMnSb. This fact was attributed to lack of Mn ions' interaction with the photo-excited carriers; a similar observation was reported in a study by Kimel *et al.* [18] in GaMnAs. Therefore, both groups attributed the observed photo-induced carrier/spin dynamics entirely to the relaxation of photo-excited electrons in the conduction band.

In III-Mn-V ferromagnetic semiconductors the s-d coupling with the localized Mn ions is significantly weaker than p-d exchange coupling characterizing the valence band. This effect may have important consequences for applications of InMnSb in developing spin based devices, since this alloy has much higher hole mobility than the other III-Mn-V ferromagnetic semiconductors.

Bibliography

[1] Stuart A. Wolf and Daryl Treger, IEEE TRANSACTIONS ON MAGNETICS, **36**, 5, (2000)

[2] http://www.research.ibm.com/research/gmr.html

[3] http://en.wikipedia.org/wiki/Giant_magnetoresistive_effect

[4] Gary A. Prinz, Science **282**,1660 (1998).

[5] D. D. Awschalom, D. Loss, and N. Samarth, Semiconductor Spintronics and Quantum Computation (Springer, Berlin, 2002).

[6] A. Cho, Science **296**, 246 (2002).

[7] S. Datta and B. Das, Appl. Phys. Lett. **56**, 665 (1990).

[8] G. A. Khodaparast, R. E. Doezema, S.J. Chung, K. Goldammer, and M. B. Santos, Phys. Rev.B **70**, 155322 (2004).

[9] T. Wojtowicz, G. Cywinski, W. L. Lim, X. Liu, M. Dobrowolska, J. K. Furdyna, K. M. Yu, W. Walukiewicz, G. B. Kim, M. Cheon, X. Chen, S. M. Wang, and H. Luo, Appl. Phys. Lett. **82**, 4310 (2003).

[10] E. O. Kane, J. Phys. Chem. Solids 1, 249 (1957).

[11] B.Koopmans, M. van Kampen, J. T. Kohlhepp, and W. J. M. de Jonge, Phys. Rev. Lett. bf 85, 844 (2000).

[12] E. Beaurepaire, M. Maret, V. Halte,J. C. Merle, A. Daunois, and J.-Y. Bigot, Phys. Rev. B **58**, 12134 (1998).

[13] J. Gudde, U. Conrad, V. Jahnke, J. Hohlfeld, and E. Matthias, Phys. Rev. B bf 59, R6608 (1999).

[14] V. Beĺkov, S. D. Ganichev, Petra Schneider, C. Back, M. Oestreich, J. Rudolph, D. Hägele, L. E. Golub, W. Wegscheider, and W. Prettl, Solid State Commun. **128**, 283 (2003).

[15] G. F. Dresselhaus, Phys. Rev. **100**, 580 (1955).

[16] M. I. Dýakonov and V. I. Perel', Pis. Zh. Eksp. Teor. Fiz., **13**, 206 (1971)(Engl. transl. Sov. Phys. JETP **13**, 144 (1971)).

[17] K. Nontapot,R. N. Kini, A. Gifford,T. R. Merritt, G. A. Khodaparast, T. Wojtowicz, X. Liu, J. K. Furdyna, Appl. Phys. Lett. 90, 143109 (2007).

[18] A. V. Kimel, G. V. Astakhov, G. M. Schott, A. Kirilyuk, D. R. Yakovlev, G. Karczewski, W. Ossau, G. Schmidt, L. W. Molenkamp, and Th. Rasing, Phys. Rev. Lett. **92**, 237203 (2004).

[19] R. J. Elliot, Phys. Rev.**96**, 266 (1954).

[20] S D Ganichev and W Prettl, J. Phys.:Condens. Matter **15** (2003) R935-R983

Chapter 2

Circular Photogalvanic Effect (CPGE) in InSb Structures

2.1 Introduction

Indium Antimonide based semiconductors are important material systems for developing spin-based devices due in part to the unique material properties they possess. Of III-V binary semiconductors, InSb has the smallest bandgap (0.24 eV), smallest effective mass (0.014 m_e), largest g-factor (-51), largest spin splitting, highest room temperature intrinsic mobility, and most non-parabolic band structure. The large g-factor and large spin splitting make this material system an ideal candidate for spin-dependent phenomena. Our measurements take advantage of the large spin splitting to generate a spin-polarized photocurrent via the

Circular Photogalvanic Effect (CPGE). Earlier measurements in other III-V semiconductors by Ganichev *et al.* [1], Yang *et al.* [3], Cho *et al.* [4] [5], and Zhang *et al.* [6] demonstrated the creation of spin photocurrent by CPGE, with significant dependence on the sample structures, strain, and symmetry. The measurements performed herein probed CPGE in InSb thin films on different substartes and InSb quantum wells with symmetric and asymmetric confinements.

2.2 Theory

2.2.1 Spin Splitting and Spin Photocurrent – a simplified picture

A simplified picture of CPGE to generate spin-polarized current is presented in Fig. 2.1. The combination of spin splitting and the optical selection rules can result in an unbalanced occupation of the k_+ and k_- states and therefore generating a spin-polarized current. It is important to note that the CPGE current decays with the momentum relaxation time and the direction of the current depends on the polarity of the circularly polarized light. The splitting in k space can originate from the bulk inversion asymmetry (BIA), known as the Dresselhaus splitting [19], as well as the structural inversion asymmetry (SIA), known as the Rashba term [20]. The Dresselhaus term is reflected in a k^3 term and SIA as a k term in the Hamiltonian in the presence of spin-orbit coupling. Averaging the cubic term in two dimensional (2D) systems along the quantization axis, when only the lowest subband is

occupied [18], results in a linear term in k. In addition, in a 2D system, both BIA and SIA can contribute to the photo-current with predicted non equal contributions [21].

Spin polarized current can be generated via the spin galvanic effect (SGE) where non-equilibrium distribution of electrons in second conduction band can relax quickly due to phonon emissions, and a current can be caused by asymmetric spin-flip scattering in the first conduction band [2]. The observation of SGE in our structures requires excitation pulses above 20 μm that can be only achieved using free electron lasers.

In order to estimate the magnitude of the spin-polarized current originating from CPGE it is easier to consider the scenario where the splitting originates from a k linear term. In this case, the net electron velocity in the conduction band is given by [2].

$$v_e = \frac{2(\beta m_{hh} - \alpha m_e)}{[\hbar(m_{hh} + m_e)]} \tag{2.1}$$

where β and α are the parameters representing the splitting of the valence and conduction bands in k-space, respectively, and m_{hh} and m_e are the heavy hole and electron effective masses.

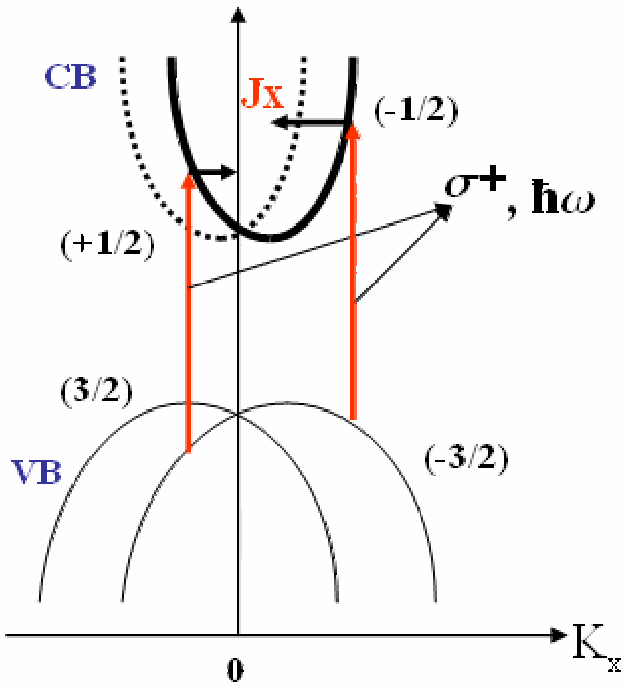

Figure 2.1: Microscopic picture of CPGE for interband absorption of circularly polarized light with photon energy $\hbar\omega$. When circularly polarized light for a given photon energy induces optical transitions between the valence band (VB) and the conduction band (CB), the combination of spin splitting and the optical selection rules can result in an unbalanced occupation of the k_+ and k_- states generating a spin-polarized current. The current direction depends on the polarization of the incident radiation [2].

2.2.2 Effects of symmetries on photocurrent

Point Groups and Inversion Symmetry

Point groups are defined by transformations that leave a point invariant; these transformations applied to a crystal structure leave the crystal unchanged. Symmetry operations include rotations, reflections, and inversions.

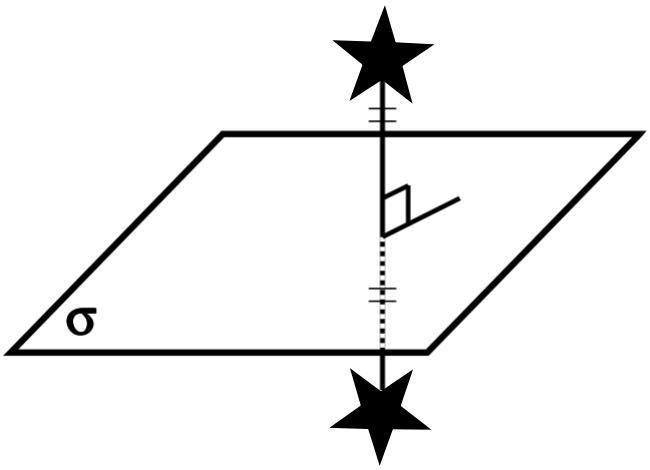

Figure 2.2: The C_s point group; reflection through a plane. Adapted from Manijeh Razeghi, *Fundamentals of Solid State Engineering*, 3rd Edition (Springer, 2002)

The C_s point group (Fig. 2.2)represents simple reflection through a plane. The only members of this group are the reflection operation (labeled as σ) and the identity($\hat{\mathbf{1}}$): an even number of reflections about the same plane leaves things untouched, as $\sigma^2 = \hat{\mathbf{1}}$.

The C_n point group (Fig. 2.3)is defined by a rotation about an axis by some amount $2\pi/n$ with n integer. For crystals, n is limited to [1,2,3,4,6], representing rotations of the possible

structures. The C_{nh} point group is defined by a C_n rotation, and a reflection through a plane perpendicular to the rotation axis. The C_{nv} consists of a C_n rotation and a reflection through a plane containing the rotation axis. C_{nv} can be described as a combination of C_n and C_s (ref. to Fig 2.4) . [7]

Current and spin-orbit coupling terms

As a function of retardation phase, the photocurrent can be expressed by

$$j_l = \sum_m \gamma_{lm} \hat{e}_m E_0^2 sin2\varphi \tag{2.2}$$

where γ_{lm} is a second-rank pseudotensor. Similarly, the spin-orbit contribution to the Hamiltonian of such a system has the form

$$\hat{H}' = \sum_{lm} \beta_{lm} \sigma_l k_m \tag{2.3}$$

where β_{lm} is also a rank 2 pseudotensor. Both γ and β are constants defined by the sample and its structure; their nonzero elements are related to the particular point group / inversion

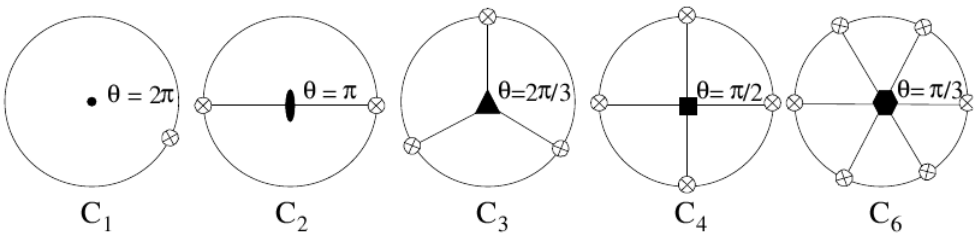

Figure 2.3: The C_n point groups; rotations about an axis. Adapted from Manijeh Razeghi, *Fundamentals of Solid State Engineering*, 3rd Edition (Springer, 2002)

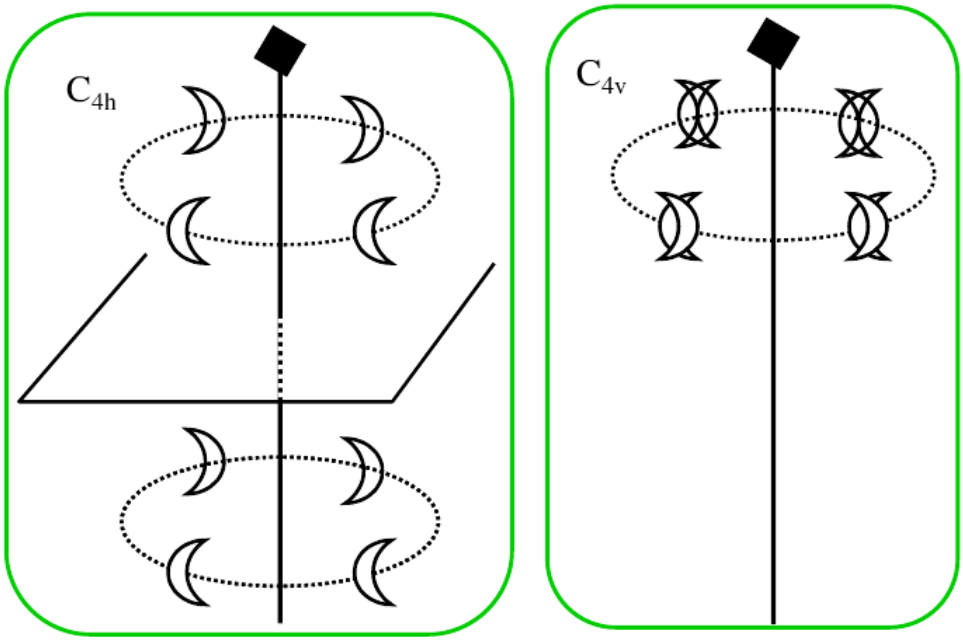

Figure 2.4: The C_{nh} and C_{nv} point groups; rotations about an axis with reflection through plane perpendicular (a) or coincident (b) to axis. Adapted from Manijeh Razeghi, *Fundamentals of Solid State Engineering*, 3rd Edition (Springer, 2002)

symmetry of the sample and the coordinate system definition. For C_{2v} symmetry, in [001] grown samples, Ganichev *et al.* [1] defines the coordinate system as $x\|[1\bar{1}0], y\|[110], z\|[001]$; z is along the growth direction while x and y are in the plane of reflection for the point group. This leaves nonzero components β_{xy} and β_{yx}, which for C_{2v} are not equal; they can be split into symmetric and asymmetric parts. The symmetric part corresponds to the contribution from bulk inversion asymmetry; the antisymmetric part comes from structure inversion asymmetry. Splitting into symmetric and asymmetric parts, the Hamiltonian can be represented as:

$$\hat{H}_{BIA} = \beta^s_{xy}(\sigma_x k_y + \sigma_y k_x)$$

$$\hat{H}_{SIA} = \beta^a_{xy}(\sigma_x k_y - \sigma_y k_x)$$

As γ shares the same symmetry as β, $\gamma_{xy} \neq \gamma_{yx}$. This gives for the x- and y- components of the current as following:

$$\begin{aligned} j_x &= \gamma_{xy}\hat{e}_y E_0^2 P_{circ} \\ j_y &= \gamma_{xy}\hat{e}_x E_0^2 P_{circ} \end{aligned}$$

$\hat{e}_m$ is the unit vector in the direction of the incident light. In both equations, j is perpendicular to this unit vector; the current flows perpendicularly to the incident light. For normal incidence $\hat{e}$ is along [0 0 1], $\hat{e}_x = \hat{e}_y = 0$, and there is no generated current; a photocurrent

arises only with oblique incident light. For samples with C_s symmetry, with growth direction [113], the defined coordinates are $x \| [1\bar{1}0], y \| [33\bar{2}], z \| [113]$. Here x is normal to the reflection plane, with z the growth direction. This gives an extra term $\hat{H}' = \beta_{zx}\sigma_z k_x$. The extra term β_{zx} is mirrored in γ, giving an extra term to the current, which takes the form

$$
\begin{aligned}
j_x &= [\gamma_{xy}\hat{e}_y + \gamma_{xz}e_z]E_0^2 P_{circ} \\
j_y &= \gamma_{xy}\hat{e}_x E_0^2 P_{circ}
\end{aligned}
$$

At normal incidence, $\hat{e}_z = 1$ and the current is $j = \gamma_{xz}\hat{e}_z E_0^2 P_{circ} \neq 0$; for the lower symmetry C_s systems a current is generated for light at normal incidence.

2.2.3 Earlier Measurements

Ganichev *et al.* [1] investigated CPGE in GaAs, InAs, and SiGe heterostructures with structures belonging to the point groups C_{2v} and C_s. The GaAs structures consisted of 4-20 nm thick n- and p-type GaAs active layers bounded with AlGaAs barriers. The InAs QWs consisted of 15 nm thick n-type InAs active layers with AlGaSb barriers. the SiGe structures were grown as asymmetric wells. Excitation was performed using a TEA-CO_2 laser for mid-IR wavelengths and a molecular FIR laser, covering a band from 9.2 μm to 496 μm. Polarization of the laser pulses was accomplished using a Fresnel Rhomb for MIR and quarter-waveplates for FIR wavelengths. The current was detected via voltage drop over a

50 Ω resistor, measured with a lock-in amplifier In the InAs QW structure (C_{2v} structure), a

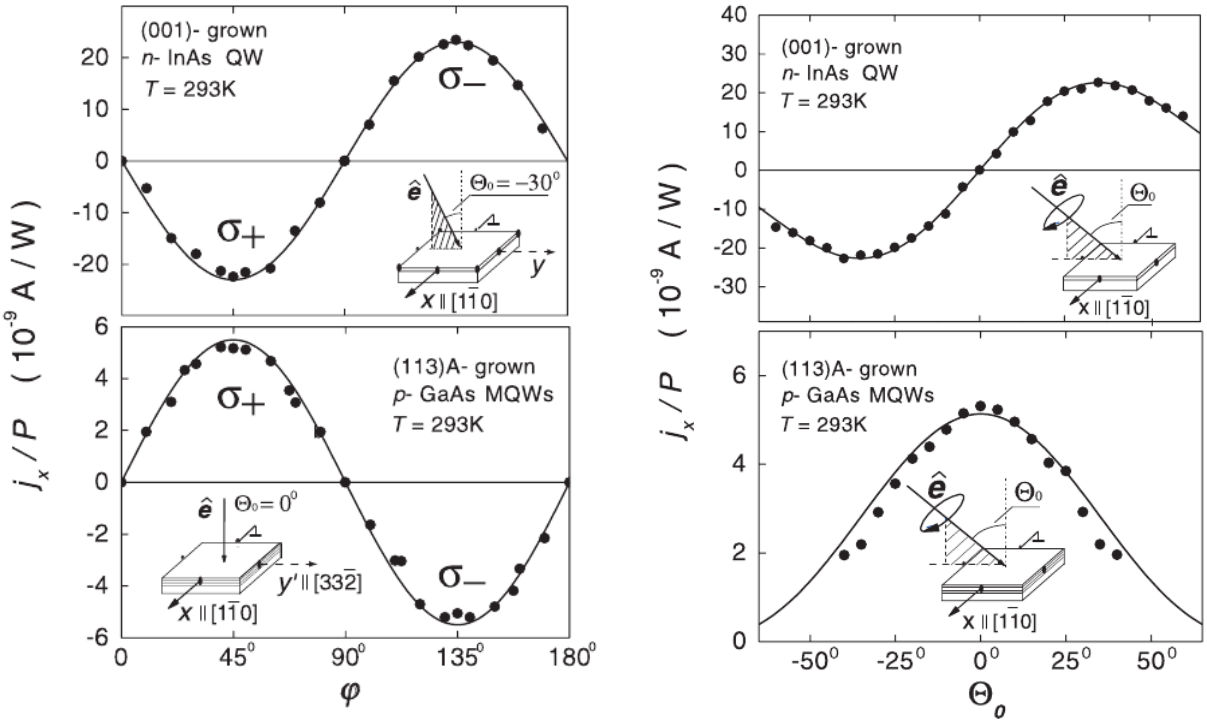

Figure 2.5: Photocurrents measured in an n-InAs/AlGaSb QW and p-GaAs/AlGaAs MQW at $\lambda = 76\mu m$, T = 293 K. The left figure shows the current as a function of retardation phase and the right figure demonstrates the current as a function of incidence angle. Figures adapted from: S D Ganichev and W Prettl, J. Phys. Condensed Matter 15, R935-R983 (2003).

maximum current of 20 nA/W was observed. The photocurrent had the sinusoidal behavior characteristic of a spin-polarized current. The GaAs MQW structure (C_s) had a similar magnitude, reaching a maximum current of 6 nA/W, at the normal incidence, dropping off to near zero at high incidence angle. In the InAs sample, the angular dependence appears sinusoidal, zero at normal incidence and maximizing at $\theta = 30°$. The SiGe QW showed a

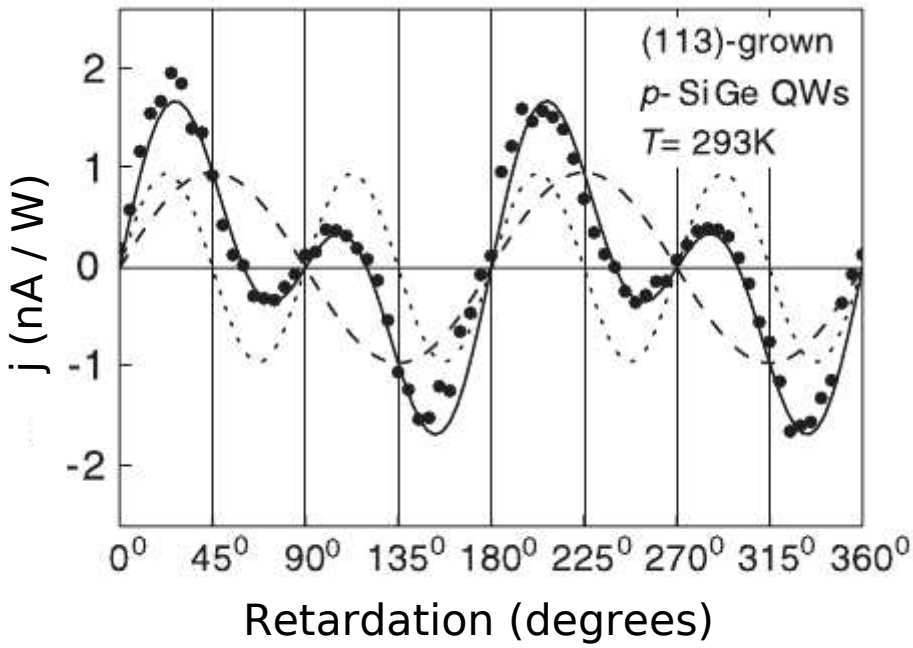

Figure 2.6: Photocurrent in an SiGe (113) QW at normal incidence, $\lambda = 280\mu m$, T = 293 K; fit indicating components of both CPGE and linear photo-galvanic effect (plotted alongside $j \propto sin2\varphi$ and $j \propto sin2\varphi cos2\varphi$. Figure adapted from: S D Ganichev and W Prettl, J. Phys. Condensed Matter 15, R935-R983 (2003).

photocurrent of $\sim$ 2 nA / W, with a pattern indicating contributions of the $sin2\varphi$ (from CPGE) and $sin2\varphi cos2\varphi$ (arising from linear photo-galvanic effect).

2.2.4 CPGE in InGaAs - Yang *et al.*

Yang *et al.* [3] investigated spin polarized current in InGaAs/InAlAs two-dimensional electron gas structures (2DEGS), using a tunable Ti-Sapphire femtosecond laser. To generate the

desired polarization a photoelastic modulator or a waveplate was used. Shubnikov-de Hass measurements, shown in Fig. 2.8, demonstrating the zero field spin-splitting and the carrier concentrations. At $T = 10K, \lambda = 880nm$, Fig. 2.7 shows an asymmetry in the photocurrent generated in one their samples, with a maximum current of $\sim$ 1-5 nA/W. The observed current demonstrates an angular dependence, with the maximum at the incident angle of $\theta \sim 45°$.

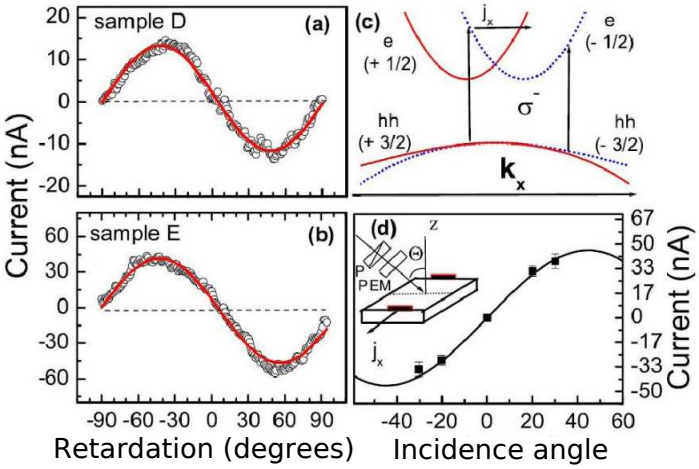

Figure 2.7: a) and b) Spin photocurrent measured in the two samples as a function of retardation phase, at $\theta = 30°, \lambda = 880nm, P_{laser} = 100mW, T = 10K$. c) Spin splitting in the band structure that allowing the generation of a spin photocurrent. d) Spin photocurrent measured as a function of incidence angle; inset shows the experimental schematic. Adapted from: C. L. Yang, H. T. He, Lu Ding, L. J. Cui, Y. P. Zeng, J. N. Wang, and W. K. Ge, Phys. Rev. Lett. 96, 186605 (2006).

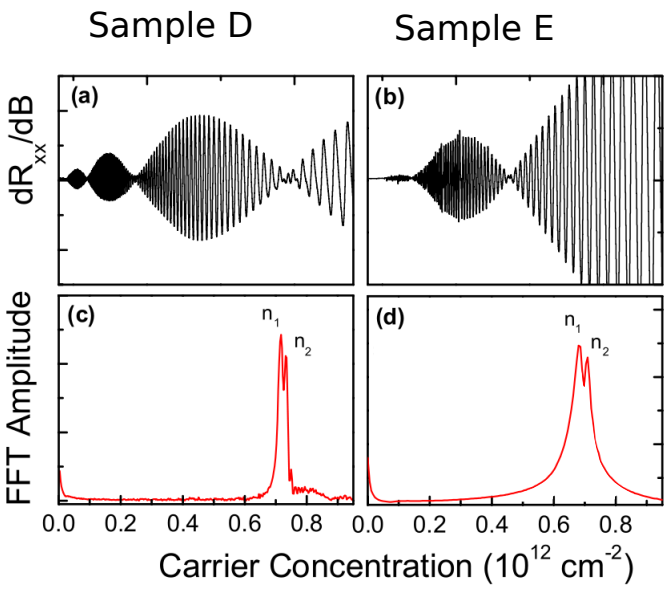

Figure 2.8: Shubnikov-de Haas oscillations in the InGaAs 2DEG samples at T = 1.6 K [a) and b)] and calculated carrier concentrations [c) and d)]. Adapted from: C. L. Yang, H. T. He, Lu Ding, L. J. Cui, Y. P. Zeng, J. N. Wang, and W. K. Ge, Phys. Rev. Lett. 96, 186605 (2006).

2.2.5 CPGE in GaN - Cho *et al.*

Cho *et al.* [4] performed CPGE measurements two Si-doped AlGaN/GaN heterostructures, each consisting of a 1 μm undoped GaN layer $[E_g = 3.42eV]$ with a 10 nm Si-doped AlGaN spacer and 20 nm Si-doped AlGaN barrier, grown on Al_2O_3 substrate. The two samples differed in doping concentrations (A - $3 \times 10^{18}/cm^3$, B - $8 \times 10^{17}/cm^3$). Shubnikov-de Haas measurements, shown in Fig. 2.9, indicated the presence of zero field spin-splitting. Each sample was optically pumped at $\lambda = 325nm, \hbar\omega = 3.82eV$ by a He-Cd laser. As seen in Fig. 2.10, a maximum current of $\sim$ 2.1 nA/W was observed, at an angle of incidence $\theta = 50°$, falling away as θ approaches 0° or 90°.

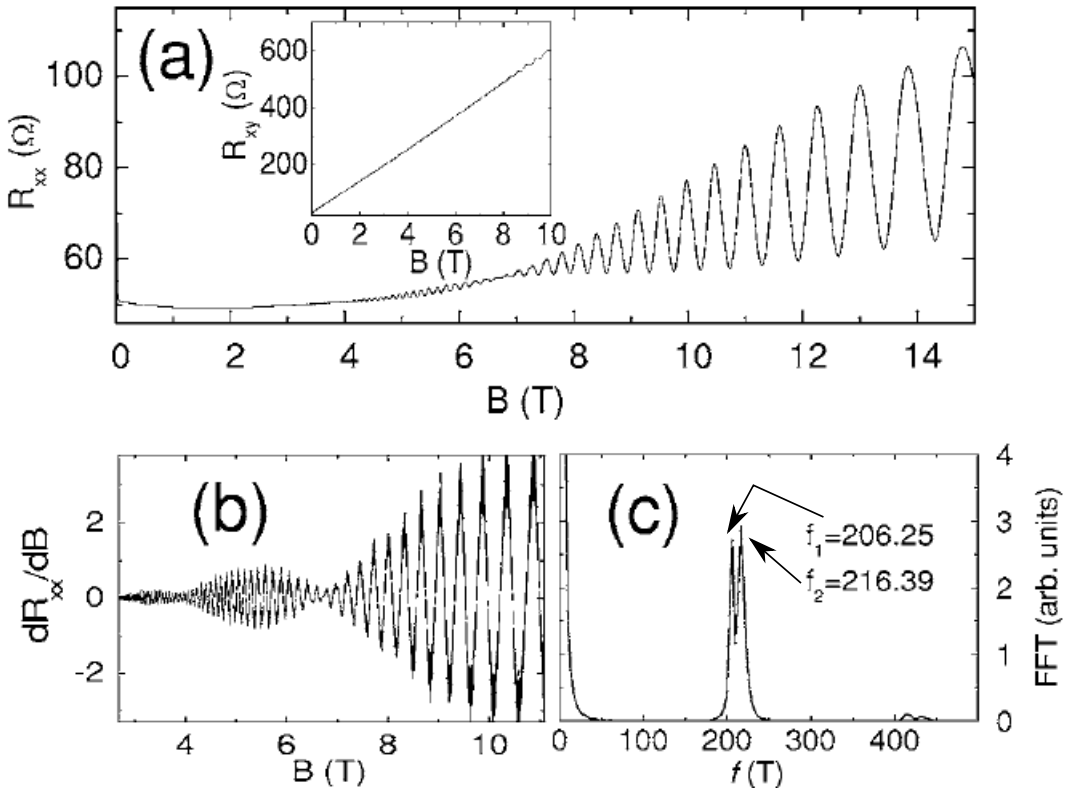

Figure 2.9: SdH measurements at T = 0.3 K in a AlGaN/GaN heterostructure, inset showing the Hall measurement at 4.2 K. Source: K.S. Cho, C.-T. Liang, and Y.F. Chen, Adapted from Phys. Rev. B 75, 085327 (2007).

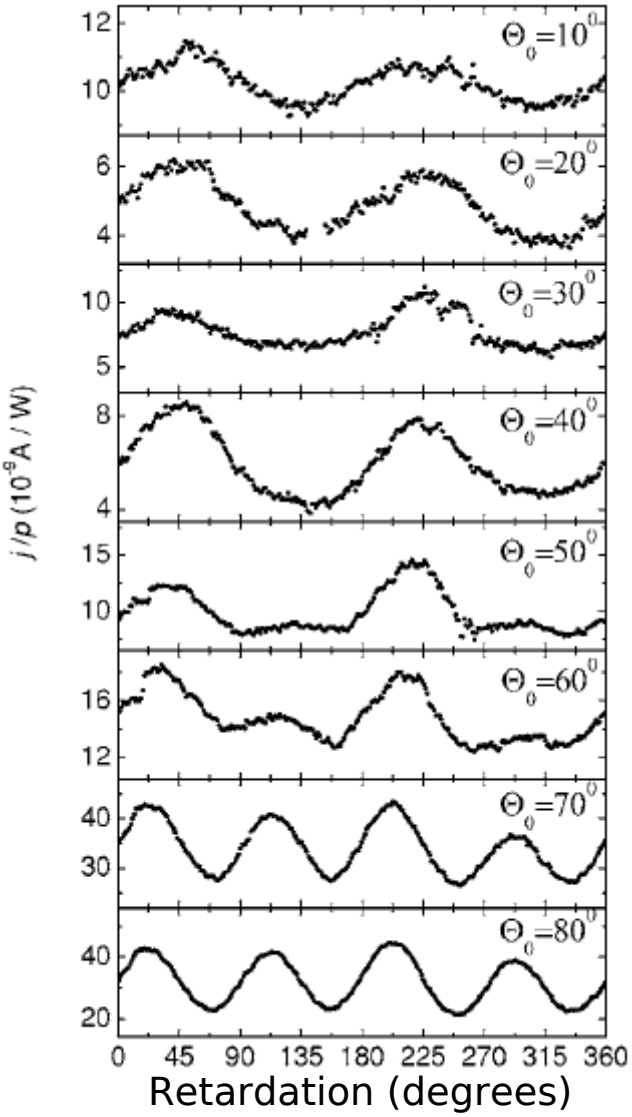

Figure 2.10: Photocurrent in the AlGaN/GaN heterostructure, as a function of retardation phase, plotted for various angles of incidence. Adapted from: K.S. Cho, C.-T. Liang, and Y.F. Chen, Phys. Rev. B 75, 085327 (2007).

Cho *et al.* [5] also investigated CPGE in an Mg-doped AlGaN/GaN multiple quantum well structure consisting of fifty, 3 nm GaN wells [$E_g = 3.42eV$], with magnesium doping around $3 \times 10^{17}/cm^3$, interlaced with 3 nm AlGaN barriers grown on Al_2O_3 substrate. Their sample was optically pumped with a He-Cd laser at $\lambda = 325nm, \hbar\omega = 3.82eV$. Detection of the current was employed by measuring a voltage drop across a 50 Ω resistor using a lock-in amplifier. As seen in Fig. 2.11, the maximum measured current was of the order of 1.2 μA / W at room temperature. There is not an obvious temperature or angular dependence and the current appears to arise from both a CPGE and LPGE contributions, as reported earlier

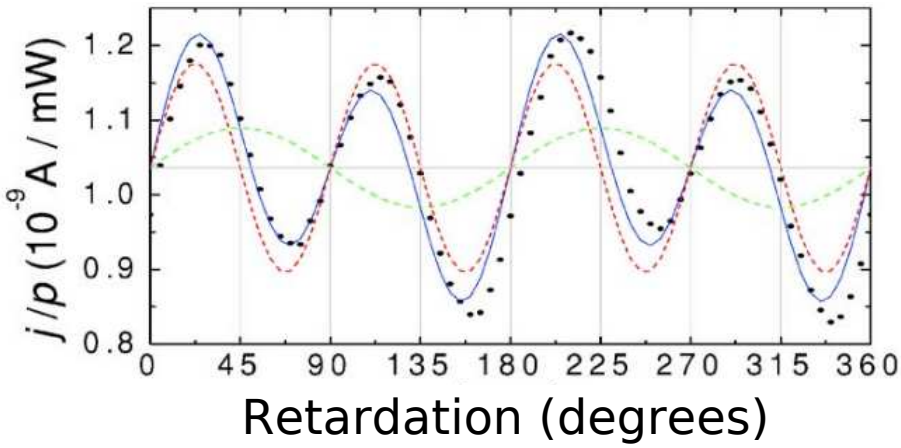

Figure 2.11: A spin photocurrent measured in an AlGaN/GaN superlattice. The measured current is $\sim$ 1.2 μA / W. Adapted from: K.S. Cho, Y.F. Chen, Y.Q. Tang and B. Shen, Appl. Phys. Lett. 90, 041909 (2007).

by Ganichev *et. al* [1] in SiGe QW.

2.2.6 CPGE In InN - Zhang *et al.*

Zhang *et al* [6] performed CPGE experiments in two samples of bulk indium nitride, with thicknesses 600 nm and 1200 nm, with strain induced on the sample by mechanically deforming the sample. Their measurements, as seen in Fig. 2.12 indicate the presence of both CPGE and LPGE contributions, as seen by Ganichev *et. al* [1] in SiGe QW and Cho*et. al* [4] MQW. In addition the CPGE terms, there is an LPGE term which takes the following form:

$$j_{LPGE} = \chi \hat{e} E_0^2 sin2\varphi cos2\varphi \tag{2.4}$$

with χ being a third-rank tensor.

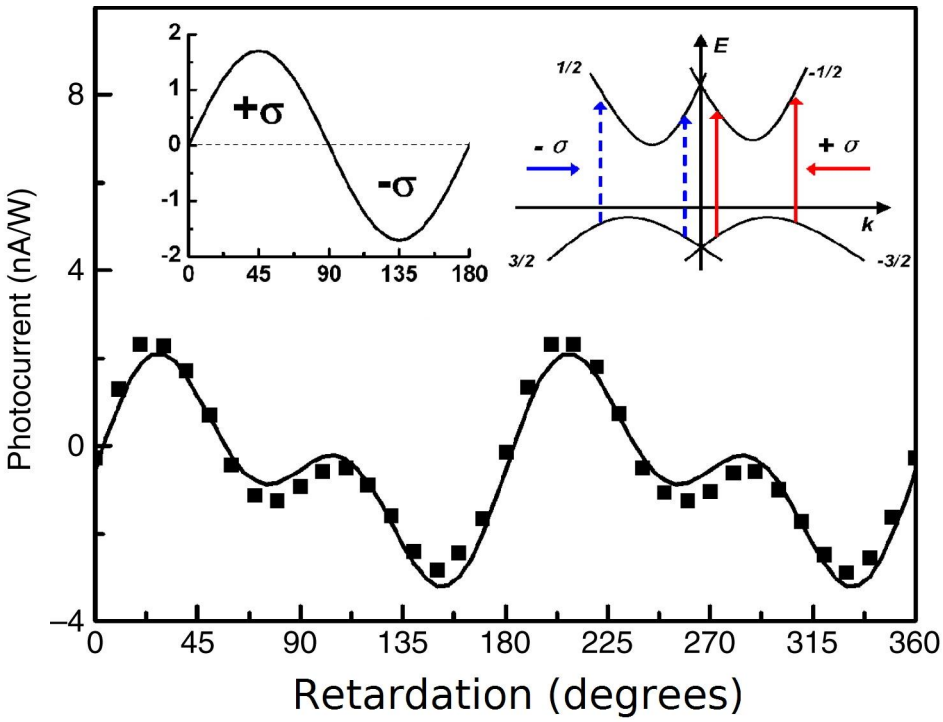

Figure 2.12: A spin photocurrent, on the order of 2 nA / W, observed in an InN thin film in which uniaxial strain is induced. The signal shows both CPGE and LPGE components, appearing as terms proportional to $sin2\varphi$ and $sin2\varphi cos2\varphi$ ($\phi = 45°, 135°$, etc) Adapted from: Z. Zhang, R. Zhang, Z.L. Xie, B. Liu, M. Li, D.Y. Fu, H.N. Fang, X.Q. Xiu, H. Lu, Y.D. Zheng, Y.H. Chen, C.G. Tang, and Z.G. Wang Solid State Communications 149, 1004 1007 (2009).

The current shows a linear dependence on the induced strain, as indicated in fig. 2.13. Theoretical analysis supports the contribution of strain in generation the photocurrent due to structure inversion asymmetry (SIA). The SIA photocurrent can be formulated as:

$$j_{SIA} = b[E_s + P_{un}\frac{\varepsilon_{yy}}{\varepsilon_{InN}}]$$

where P_{un} is the piezoelectric polarization and ε_{InN} the dielectric constant.

2.3 Our Experimental Approach

To modulate the laser's polarization a photo-elastic modulator (PEM) was used. A PEM takes linearly polarized light and retards one component of the polarization by means of an oscillating birefringent medium. The polarized beams are made incident upon the sample, mounted in a cryostat where the angle of incidence can be adjusted. The current is measured through pairs of contacts on the sample, passing through a distribution box which allowed for selecting contacts to a current amplifier. The current amplifier converts the small current into a measurable voltage which is detected with a lock-in amplifier, triggered by the oscillation frequency of the PEM. The experimental setup and approach are described in a more detailed in the following sections.

Photo-Elastic Modulator (PEM)

The polarization of the incident beam was modulated using a Hinds Instruments PEM-90 photoelastic modulator (PEM). A PEM takes advantage of the photoelastic effect, in which

mechanical stresses in a material induce birefringence. The optical element of the PEM consists of a rectangular bar of fused silica which is tuned to oscillate at frequency of 50 kHz by a quartz piezoelectric transducer. These vibrations generate birefringence at the center of the bar at the same frequency, proportional to the amplitude of the vibrations. When the plane of polarization is rotated 45° with respect to the bar, one polarization component will pass through the bar faster than the other, leading to an elliptically polarized pulse. The retardation (the phase difference between the components) is given by

$$A(t) = z[n_x(t) - n_y(t)]$$

where z is the bar thickness and n(t) is the index of refraction in the given direction. The helicity of the elliptically-polarized pulse is given by

$$P_{circ} = sin(2\varphi)$$

where φ is the retardation in fractions of a wavelength.

The PEM has frequency outputs proportional to f and 2f, which are used to trigger a lock-in amplifier. The f output, which is used in our measurements, corresponds to the frequency of the oscillation of the polarization, with pulses coinciding with only the positive retardation. The 2f output operates at twice the oscillation frequency, with pulses coinciding to both positive and negative retardations. Triggering the lock-in amplifier with the f output ensured the detection of the signals originating only from the desired retardation. The PEM is limited to one retardation at any wavelength where:

$$\lambda(nm) \times \varphi(fractionsofwavelength) = 500$$

This fact effectively limits the range of the wavelengths; for example; at 800 nm, the maximum retardation is just over half a wavelength.

Cryostat

The sample was housed in a Cryo-Industry cryostat which allowed for rotating the sample *in situ* and controlling the temperature. The optical windows were fused silica and the measurements were performed typically at 4 K, 77 K, and 290 K, with incidence angles ranging from 0° to 50°.

Current amplifier

A low-noise current preamplifier (Stanford Research Systems model SR570) was connected to the contacts through the distribution box to amplify the current before the measurements. The current preamplifier detects an input current and output a voltage at a ratio determined by the sensitivity (ranging from 1 mA / V to 1 pA / V). For these measurements, a sensitivity of 1 μA / V was used.

Lock-in Amplifier

Detection of the amplified voltage was performed using a lock-in amplifier (Stanford Research Systems, model SR830). The lock-in amplifier can detect the small AC voltage from the current preamplifier using a reference provided by the laser power supply. A sinusoidal

reference wave was generated from the reference pulses from the laser, and then multiplied with the amplified signal from the current preamplifier. The result of this multiplication is two AC signals at the sum and difference frequencies of the signal and reference. Passing these two signals through a low-pass filter removes all the signals for which the signal frequency is different from the reference frequency. The remaining signal, where the frequencies are equal, is a DC signal

$$V_{out} \propto V_{signal} cos(\Delta\phi)$$

where $\Delta\phi$ is the difference in phase between the signal and reference. This process of multiplying and filtering is known as phase-sensitive detection (PSD). Performing PSD on the output with a new reference 90° out of phase with the original reference will remove the phase dependency, giving by:

$$\begin{aligned} X &= V_{signal} cos(\phi_{signal}) \\ Y &= V_{signal} sin(\phi_{signal}) \\ R &= \sqrt{X^2 + Y^2} \end{aligned}$$

2.3.1 Connecting to the Current Amplifier

The connection between the samples and the current amplifier was performed using a distribution box. The box provided a BNC connector for each contact on the sample and up to four contacts were utilized on the sample. To form a complete circuit, one contact was connected to the current amplifier by a BNC cable, while another contact was connected to

chassis ground by a shorted BNC cable The current path was from the current amplifier to a contact, across the sample between contacts, from the second contact to chassis ground, and returning to the chassis ground of the amplifier. The current amplifier acted as a common ground, with the chassis ground from the lock-in amplifier and the distribution box and cryostat connected to it.

2.4 Samples

In these measurements, we studied two InSb films and two 30 nm wide InSb QWs. Table I summarizes the sample's characteristics at different temperatures. The first film, InSb/GaAs (LA679) consists of a 0.2 μm undoped InSb buffer layer grown on GaAs substrate (100), followed by a 1.3 μm, 2.6x10^{16} cm^{-3} Te-doped InSb active layer, capped by a 0.05 μm, 1.5x10^{17} cm^{-3} Te-doped InSb contacting layer. The second InSb film, InSb/InP was grown by MBE with a similar layer structures of the first film. The sample consists of 0.18 μm InSb buffer layer grown on InP (001) substrate following by a 1.2 μm Si-doped InSb active layer capped by a 40 nm layer of Si-doped InSb. The lattice constant of InP [5.868Å] is closer to that of InSb [6.47Å] than the lattice constant of GaAs [5.654Å].

The QWs studied in this work both are 30 nm wide, S360 has $\sim$ 35 nm of $Al_xIn_{1-x}Sb$ and a single Si-δ doped layer above the InSb layer; whereas, S710 has 210 nm thick of $Al_xIn_{1-x}Sb$ and three δ doped layers above the well. The detailed growth conditions of the InSb QW samples were described previously [25, 13]. In a 30 nm wide asymmetric InSb/$Al_{0.09}In_{0.91}Sb$

QW such as S360, a doping density of $\sim 2.0\times10^{11}$ cm^{-2} can result in an in built electric field of 3.3×10^{6} V/m corresponding to an effective magnetic field of ~ 0.2 mT [26].

In general, bulk semiconductors with zinc blende lattice structures are non-gyrotropic and CPGE is considered to be forbidden; however, the structures can become gyrotropic in the presence of uniaxial strain or quantum confinement[23, 2]. Therefore, CPGE can contribute to the generation of spin polarized currents in QWs. To probe a possible contribution of strain to CPGE in the InSb films, we monitored x-ray reflections from (004) and (335) planes of the InSb/GaAs film. From these measurements, we could deduce the out-of-plane lattice constant ($c = 6.4832 \pm 0.0021$ Å) and the average in-plane lattice constant ($a_L = 6.4756 \pm 0.0023$Å). If the InSb layer was fully relaxed, a_L and c would both be 6.4794 Å. If the InSb layer was fully strained on the GaAs substrate, a_L and c would be 5.6533 and 7.3041 Å; respectively. Since c only slightly larger than a_L in this sample, the layer is only slightly strained. From the usual definition of percentage relaxation, $R = (6.4756 - 5.6533)/(6.4797 - 5.6533)$, the film is 99.54% relaxed. A similar result is expected for the InSb/InP film. The lack of strain and the observation of CPGE in these films are suggesting other mechanisms responsible for the generation of the spin polarized currents in non-gyrotropic structures.

2.5 Observations and Discussion

Examples of our measurements on InSb films and QWs are presented here. Figure 3 shows the currents at 290 K in InSb/GaAs film, for several θ as a function of retardation, indicating the sensitivity of the CPGE photocurrent to the helicity of the incident radiation. The helicity can be expressed as:

$$P_{circ} = \frac{I_{\sigma_+} - I_{\sigma_-}}{I_{\sigma_+} + I_{\sigma_-}} = \sin 2\varphi \tag{2.5}$$

P_{circ} can vary from -1 to +1 for σ_- and σ_+ polarization, respectively and φ is the phase angle between the x and y components of the light electric field. Therefore, as shown in 2.18, the variation in the wavelength retardation can result in a period of π in the current. The current direction changes sign depends on the polarization of the incident radiation. As shown in 2.18, the magnitude of the current is maximum at $\theta = 50°$, tailing off from $\sim$ 1μA/W to zero below $\theta = 10°$.

This fact was tested and demonstrated in Fig. 2.19a, by reversing the connections to a specific pair, the polarity of the voltage changes but clearly the size of the voltage is independent of direction for($\varphi < 0$); instead, the observed asymmetry for positive retardation ($\varphi > 0$) is much larger than for negative($\varphi < 0$). Several trials with newly-soldered and annealed contacts mitigated some of the differences; however, the observed asymmetry could not be eliminated entirely by improvements to the contacts' quality. In a study by Yang *et al.* [3], an asymmetry in the measured spin polarized photo-current was also evident. The magnitude of the current in one of their samples (Sample E) for the negative retardation was smaller

than for the positive retardation.

Fig. 2.19b demonstrates the reproducibility of the measurements for $\theta = 45°$ and $\theta = 30°$ at 77 K. The contacts' configuration was switched back and forth across the sample from [1 $\rightarrow$ 3] to [2 $\rightarrow$ 4], and identical traces were measured in each case. In addition, we examined any possible contribution from the cryostat's window (Fused Silica) to the signals. As shown in Fig.2.19c at T = 290 K and $\theta = 45°$, two measurements were taken with and without the window for [1 $\rightarrow$ 3] pins configuration. The traces appear nearly identical, indicating no birefringence effect induced by the window.

Examples of the temperature dependence currents in InSb/GaAs film for $\theta = 45°$ are plotted in Fig. 2.5a. As shown in Fig. 2.5b, in order to calculate the currents, the measured voltages across the samples and the sample's resistance (obtained from a 4-contact measurement) were used. The asymmetry in the traces is more significant at 4 K; however, the maximum voltage at $-\lambda/4$, for all the traces is almost identical. In addition, for a given laser fluence, we observe strong dependence of the photo-current to the orientation of the contacts. This fact can be realized by comparing the magnitude of the current at 77 K in Fig.2.19b for [1 $\rightarrow$ 3] configuration and the measurements presented in Fig.2.5a for [2 $\rightarrow$ 4].

The observation in the InSb/GaAs film, motivated us to grow the second InSb film on InP substrate. A series of measurements on an InSb/InP film at 77 K and 290 K resulted in similar observations as the first film. Fig. 2.21 demonstrates examples of these measurements for two different contact configurations as a function of retardation. The maximum current (converted from the voltage measurements) at 290 K and 77 K at $\theta = 45°$ for [1 $\rightarrow$ 3]

configuration, is $\sim 20\mu$A/W; comparable to the measurements on the InSb/GaAs film at 77 K. As shown in Fig. 2.21a and Fig. 2.21b, the currents for the $[1 \rightarrow 3]$ configuration are larger compared to the measurements for $[2 \rightarrow 4]$, presented in Fig. 2.21c. Not shown here, the magnitude of the current for $[2 \rightarrow 4]$ in the InSb/InP film at 77 K increased by about a factor of 2 compared to the measurements at 290 K. The asymmetry in the traces and the large differences in the signal with respect to contacts' directions are similar to those seen in the InSb/GaAs film.

The natural extension of our studies was to probe InSb QWs. Fig. 2.22 demonstrates the generation of spin polarized currents in an asymmetric InSb QW (S360) at 77 K for $[1 \rightarrow 3]$ configuration. The signal falls to zero at $\theta = 30°$ from a maximum at $\theta = 40°$. Symmetry analysis shows that the helicity-dependent photocurrent in (001) QW structures can be induced only at oblique incident radiation and in the zinc-blende-type structures resulting in an electric current in the plane of QWs [8, 1]. This fact could explain the absence of current for the $[2 \rightarrow 4]$ pin configuration in this QW. Unlike the InSb based films and several other reported measurements [1], no photocurrent was observed at room temperature in S360. Under the same experimental conditions for S360, a series of measurements on two different pieces of the symmetric sample (S710) at different temperatures and angles of laser incidence θ, suggested the absence of any spin-polarized current. This fact could be due to the lack of asymmetry in the confinement potential of S710 or the thicker layer above the well in S710 compared to S360. The absorbtion length in these heterostructures (in the wavelength region used in this study) is about 0.5 μm ; therefore, the excitation wavelength can create

carriers in the $Al_xIn_{1-x}Sb$ barrier layer as well as in the QWs. An earlier measurement on an undoped InSb MQW demonstrated the generation of high density photo-excited carriers in the wells using 800 nm pulses. Selective probe of the conduction band demonstrated carrier relaxation time of $\sim$ 200 ps [9].

2.6 Summary

We measured large spin-polarized photocurrents in InSb thin films and asymmetric QWs via CPGE. Our setup utilized circularly polarized laser pulses, taking advantage of spin-splitting and selection rules to generate excess spin-polarized carriers with non-zero momentum, resulting in a current. Observation of CPGE-induced spin currents in the thin films is thought to be due to strain, as CPGE requires inversion asymmetry. In the QWs, we see CPGE in the asymmetric well, but not in the symmetric well. In the next chapter, we explain measurements of the spin relaxation time of spin-polarized carriers excited by circularly polarized light, as done in this experiment. We use measurement of the magneto-optical Kerr effect (MOKE) resultant from the excited carriers to determine a spin relaxation time.

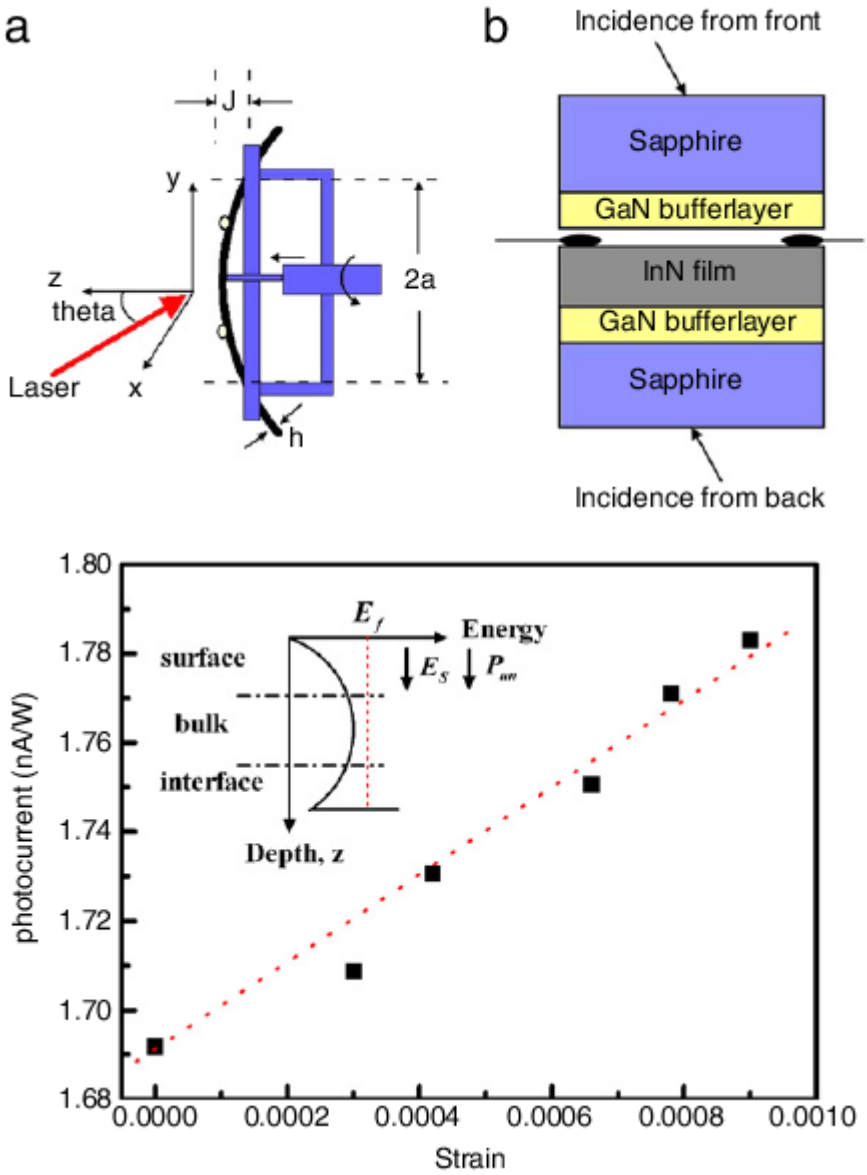

Figure 2.13: (above) The experimental setup for measuring the CPGE photocurrent and inducing strain in the InN samples. (below)Photocurrent as a function of sample strain for the InN sample. Adapted from: Z. Zhang, R. Zhang, Z.L. Xie, B. Liu, M. Li, D.Y. Fu, H.N. Fang, X.Q. Xiu, H. Lu, Y.D. Zheng, Y.H. Chen, C.G. Tang, and Z.G. Wang Solid State Communications 149, 1004 1007 (2009).

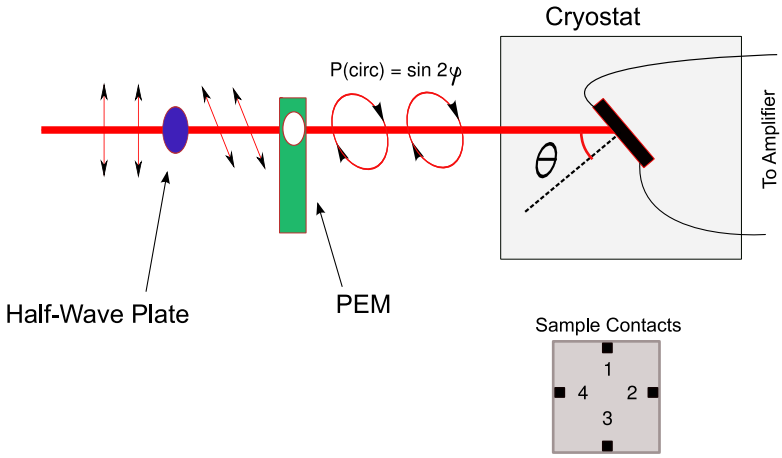

Figure 2.14: Diagram of the setup for the spin-photocurrent measurements. Linearly polarized light is modulated by a photoelastic modulator to an elliptical polarization, which is then focused on a sample, with the resultant current measured through indium contacts on the sample.

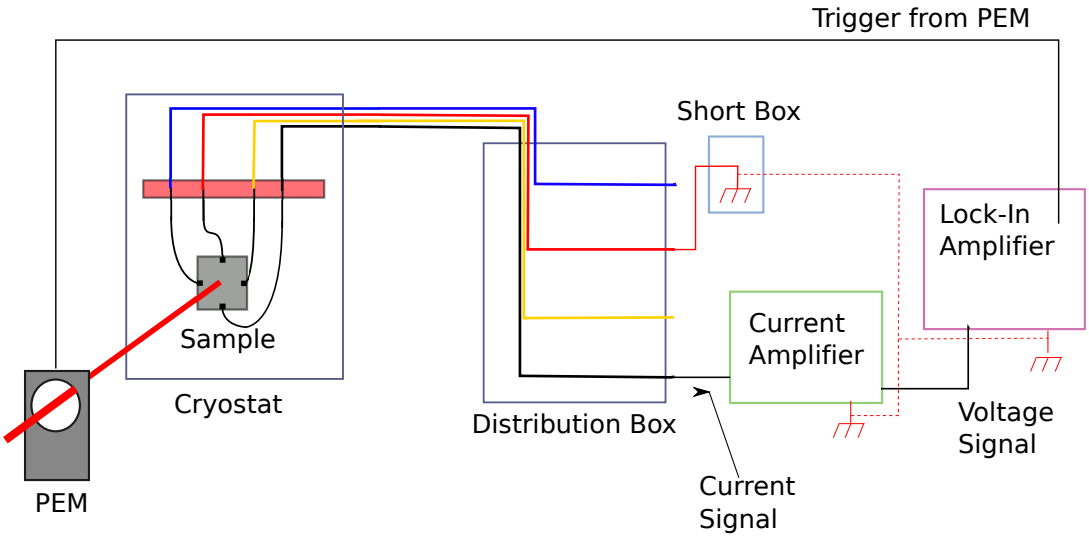

Figure 2.15: Schematic of the method used to detect the spin-polarized current. Each contact on the sample is wired to a BNC connection on the distribution box. Pairs of connections are chosen corresponding to the direction in which current is measured; one connection is to the current amplifier, while the other connection is connected to chassis ground, in common wiht the current amplifier. The current amplifier outputs a voltage which is detected by the lock-in amplifier, triggered by the PEM.

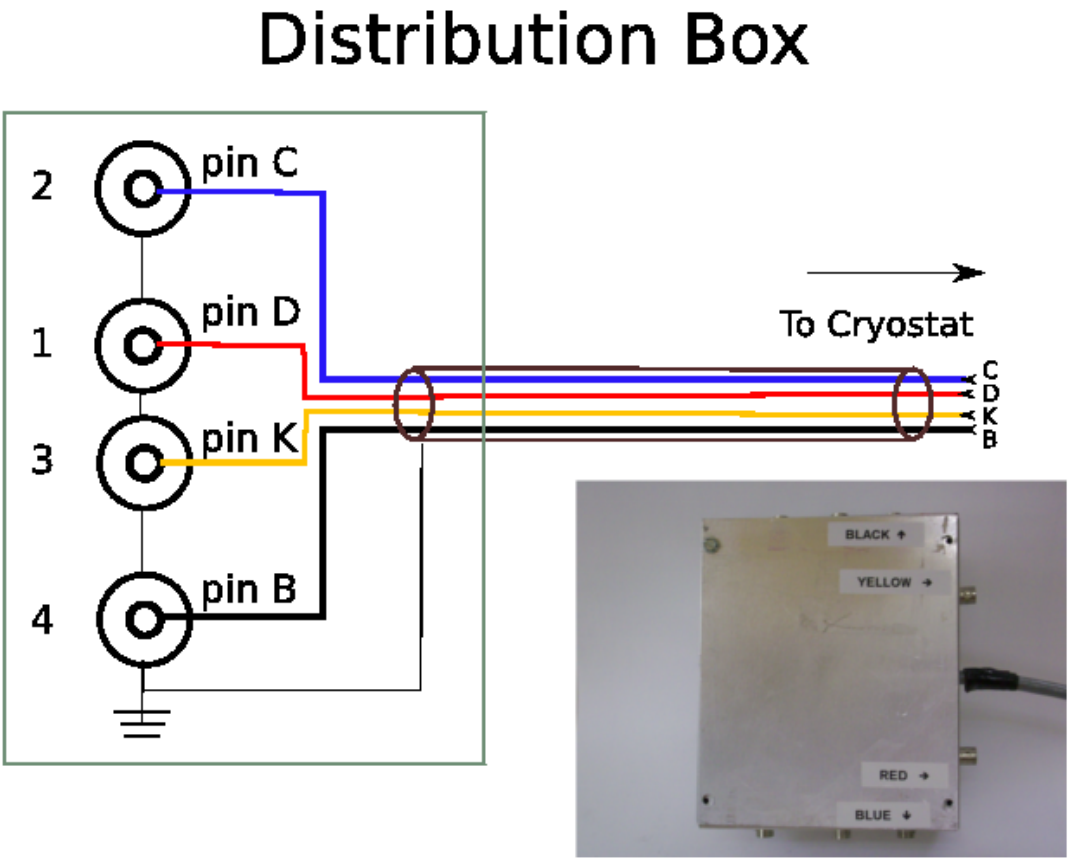

Figure 2.16: Schematic diagram of the box used to connect the amplifier to the sample. All four pins from the contacts are connected to the center conductor of the BNC connections. The outside conductors of the BNC connections are connected to chassis ground.

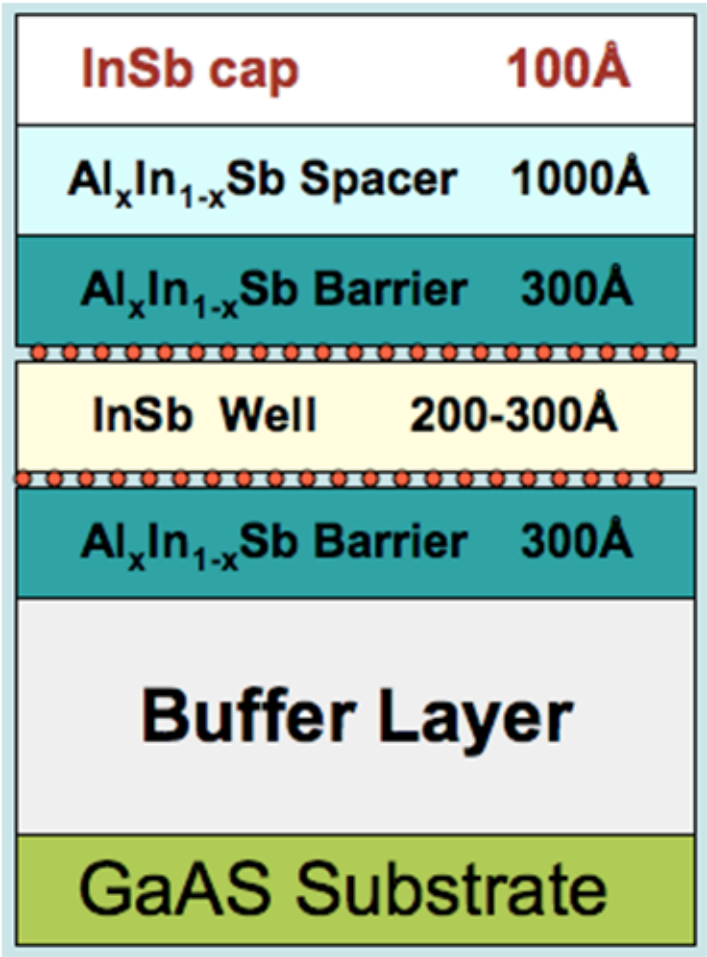

Figure 2.17: Diagram of the layer structure of sample S360, an asymmetric InSb quantum well. Provided by Prof. Santos' group, Univ. of Oklahoma.

	Sample's Temperature (K)	Density (cm^{-3})	Mobility (cm^2/Vs)	E_F meV
InSb/GaAs Film	300	2.6×10^{16}	45,500	22
	100-250	6×10^{15}	58,500	8
	77	6×10^{15}	57,000	8
	4	6.2×10^{15}	40,320	8
InSb/InP Film	300	3.5×10^{16}	2100	27.8
	77	1×10^{15}	100	2.6
	Sample's Temperature (K)	Density (cm^{-2})	Mobility (cm^2/Vs)	E_F meV
InSb QW (S360)	300	6.4×10^{11}	20,000	109
	77	3.4×10^{11}	61,000	58
	4	2.2×10^{11}	73,000	38
InSb QW (S710)	300	4.9×10^{11}	18,000	75
	77	8.0×10^{10}	38,000	12
	4	8.0×10^{10}	23,000	12

Table 2.1: The electron density, mobility, and Fermi energy (E_F) of the samples at different temperatures.

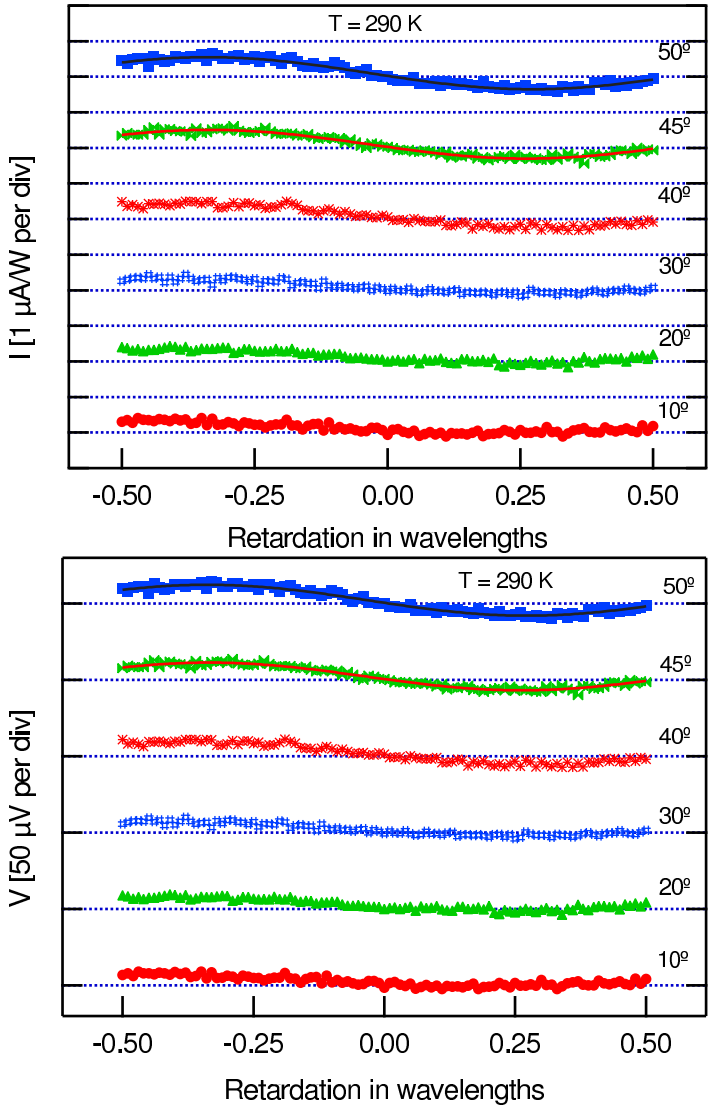

Figure 2.18: Traces of the photo-induced current at 290 K in InSb/GaAs film for several θ as a function of retardation with step size of 0.01λ. The voltages from $[2 \rightarrow 4]$ were measured and converted into the current. The magnitude of the current $\sim 1\mu$A/W at $\theta = 50°$, tailing off to a very small signal at $\theta = 10°$. Adopted from M. Frazier *et al.*, J. Appl. Phys. 106, 103513 (2009)

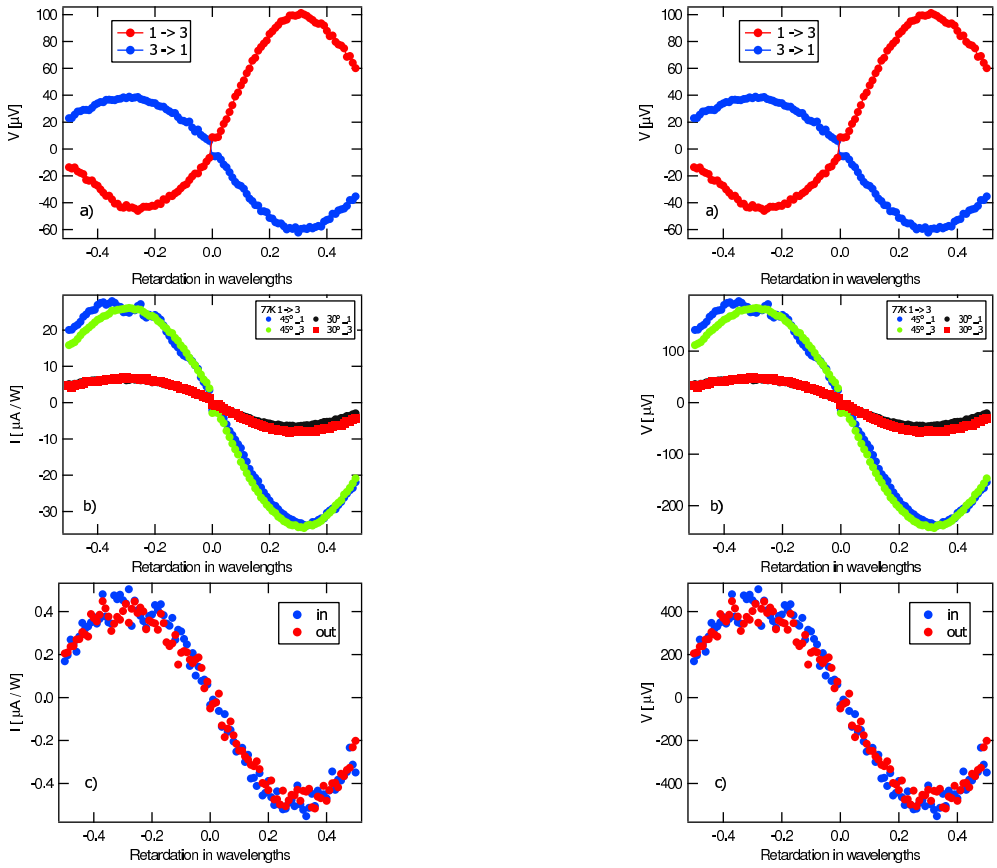

Figure 2.19: a) Probe of the asymmetry in the traces and the contacts' quality. Measurements were performed on the InSb/GaAs film at T = 290 K and $\theta = 45°$. Dependence of the asymmetry on the direction (rectification). The traces presented here are indicating that the asymmetric pattern is independent of direction; rather, positive retardation ($\varphi > 0$) generates a larger signal than negative retardation ($\varphi < 0$). b) Repeatability of the measurements with changing the contacts' configurations: a series of measurements were performed by interchanging horizontal and vertical contacts resulting in reproducible measurements. c) To probe possible effects from the cryostat's window: traces with and without the window were taken resulting in identical traces. Adopted from M Frazier *et al.*, J. Appl. Phys. 106, 103513 (2009)

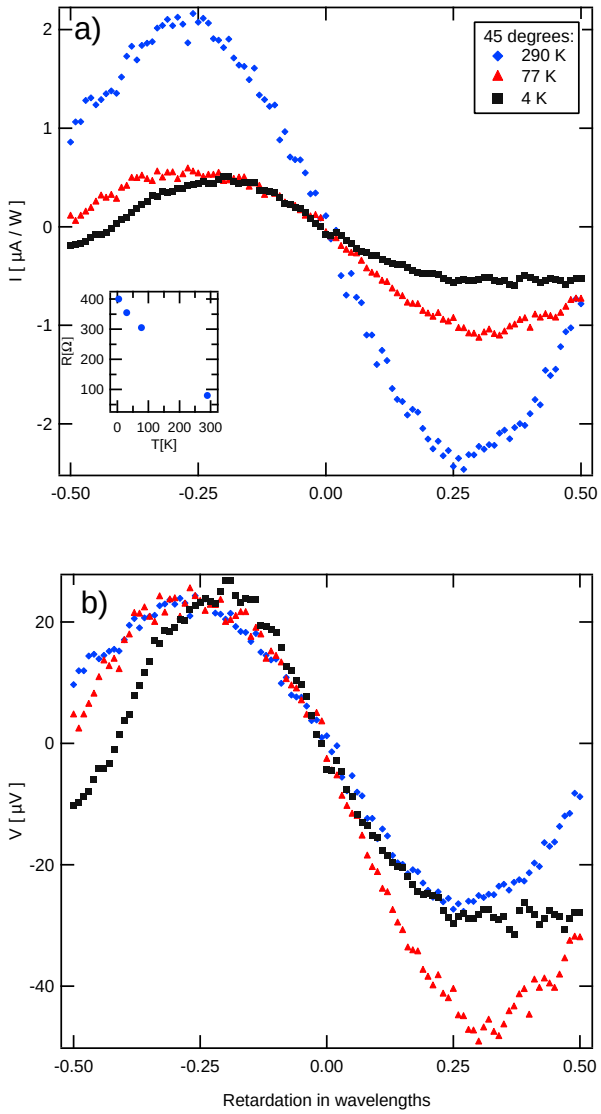

Figure 2.20: a) The temperature dependence of photo-induced currents. The inset shows the sample resistance obtained from a 4-contact measurement. b) photo-induced voltages were used to calculate the currents presented in a). Our measurements demonstrate photo-induced currents with a maximum of about 2μA/W at 290 K for $[2 \rightarrow 4]$ pins configuration. Adopted from M Frazier *et al.*, J. Appl. Phys. 106, 103513 (2009)

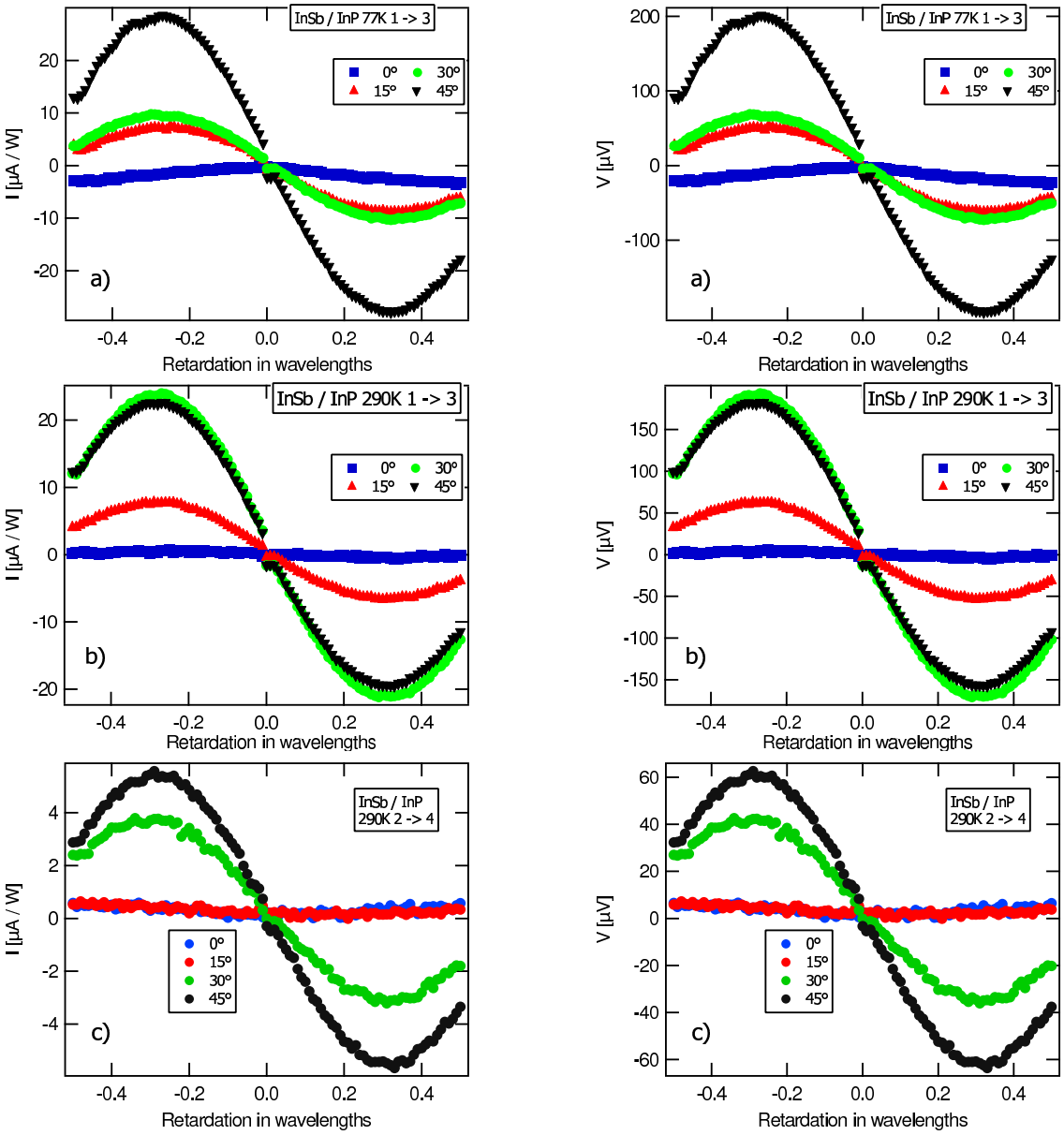

Figure 2.21: Photo-induced currents in InSb grown on InP substrate at a) 77 K and b) 290 K. The maximum signal occurs at a $\theta = 45°$ tailing to zero at smaller incident angles. c) Using contacts perpendicular to those in a) and b), the observed currents are weaker, consistent with the observation in InSb/GaAs film. Adopted from M Frazier *et al.*, J. Appl. Phys. 106, 103513 (2009).

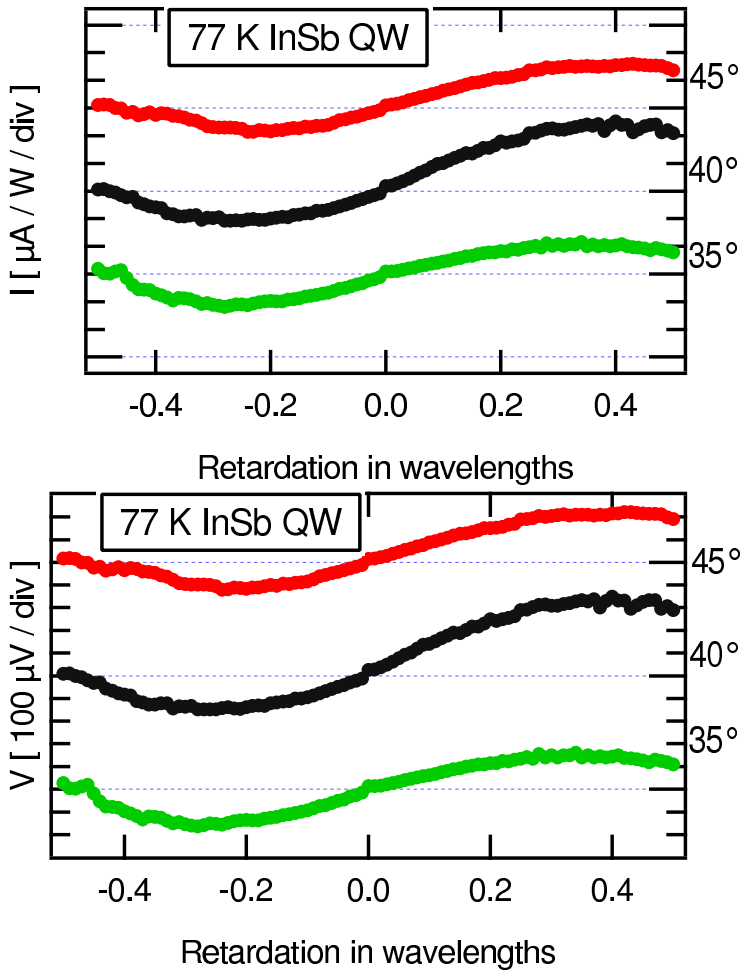

Figure 2.22: CPGE effect in an InSb QW at 77 K. The maximum signal was measured at $\theta = 40°$, approaching zero at $\theta = 30°$. The currents were observed only for $[1 \rightarrow 3]$ configuration. From the helicity-dependent photocurrent in (001) QW structures one expects to observe CPGE only at oblique incident radiation and in the zinc-blende-type materials, only in the plane of QWs. Adopted from M Frazier *et al.*, J. Appl. Phys. 106, 103513 (2009)

Bibliography

[1] S D Ganichev and W Prettl, J. Phys.:Condens. Matter **15** (2003) R935-R983

[2] S. D. Ganichev, E. L. Ivchenko, S. N. Danilov, J. Eroms, W. Wegscheider, D. Weiss, and W. Prettl, Phys. Rev. Lett. **86**, 4358 (2001)

[3] C. L. Yang, H. T. He, Lu Ding, L. J. Cui, Y. P. Zeng, J. N. Wang, and W. K. Ge, Phys. REv. Lett. 96, 186605 (2006)

[4] K.S. Cho, C.-T. Liang, and Y.F. Chen, Phys. Rev. B 75, 085327 (2007)

[5] K.S. Cho, Y.F. Chen, Y.Q. Tang and B. Shen, Appl. Phys. Lett. 90, 041909 (2007)

[6] Z. Zhang, R. Zhang, Z.L. Xie, B. Liu, M. Li, D.Y. Fu, H.N. Fang, X.Q. Xiu, H. Lu, Y.D. Zheng, Y.H. Chen, C.G. Tang, and Z.G. Wang Solid State Communications 149, 1004 1007 (2009)

[7] Manijeh Razeghi, *Fundamentals of Solid State Engineering*, 3rd Edition (Springer, 2002)

[8] S. A. Tarasenko, JETP Letters, **85**, No. 3, 182 (2007).

[9] G. A. Khodaparast, D. C. Larrabee, J. Kono, D. S. King, S. J. Chung, and M. B. Santos, Phys. Rev, B 67, 035307 (2003).

[10] N. Goel, J. Graham, J. C. Keay, K. Suzuki, S. Miyashita, M.B. Santos, Y. Hirayama, Physica E **26**, 455 (2005).

[11] Hong Chen, J. J. Heremans, J. A. Peters, N. Goel, S. J. Chung, and M. B. Santos, Appl. Phys. Lett. **86**, 032113 (2005).

[12] Hong Chen, J. J. Heremans, J. A. Peters, N. Goel, S. J. Chung, and M. B. Santos, Appl. Phys. Lett. **84**, 5380 (2004).

[13] G. A. Khodaparast, R. E. Doezema, S. J. Chung, K. J. Goldammer, and M. B. Santos Phys. Rev. B **70**, 155322 (2004).

[14] A. M. Gilbertson, W. R. Branford,M. Fearn, L. Buckle, P. D. Buckle, T. Ashley, and L. F. Cohen, Phys. Rev. B 79, 235333 (2009).

[15] N. S. Averkiev and M. I. D'yakonov Fiz. Tekh. Poluprov., **17** 629 (1983)(Engl. transl. Sov. Phys.Semicond. **17**, 393 (1983)).

[16] M. I. D'yakonov and V. I. Perel', Pis. Zh. Eksp. Teor. Fiz., **13**, 206 (1971)(Engl. transl. Sov. Phys. JETP **13**, 144 (1971)).

[17] V. Bel'kov, S. D. Ganichev, Petra Schneider, C. Back, M. Oestreich, J. Rudolph, D. Hägele, L. E. Golub, W. Wegscheider, and W. Prettl, Solid State Commun. **128**, 283 (2003).

[18] J. Zhou, J. L. Cheng, and M. W. Wu, Phys. Rev. B **75**, 045305 (2007).

[19] G. F. Dresselhaus, Phys. Rev. **100**, 580 (1955).

[20] Y.A. Bychkov and E.I. Rashba, J. Phys. C **17**, 6039 (1984); Y.A. Bychkov and E.E. Rashba, Pis'ma Zh. Eksp. Teor. Fiz. **39**, 66 (1984) [JETP Lett. **39**, 78 (1984)].

[21] L. E. Golub, Phys. Rev. B. **67**, 235320 (2003).

[22] R. Winkler, *Spin-Orbit Coupling Effects in Two-Dimensional Electron and Hole Systems , Springer Tracts in Modern Physics* (Springer, Berlin, 2003), Vol. 191, p. 216.

[23] R. Winkler in Handbook of Magnetism and Advanced Magnetic Materials, Edited by H. Kronmuller and S. Parkin, (Wiley, Chichester, 2007), Vol. V, p. 2830 Spintronics and Magnetoelectronics.

[24] M. W. Pelczynski, J. J. Heremans, and S. Schwed, Mat. Res. Soc. Symp. Proc., **607**, 65 (2000).

[25] K. J. Goldammer, W. K. Liu, G. A. Khodaparast, S. C. Lindstrom, M. B. Johnson , R. E. Doezema, M. B. Santos J. Vac. Sci. Technol. **B16**, 1367 (1998).

[26] P. Pfeffer and W. Zawadzki, Phys. Rev. B **68**, 035315 (2003).

[27] S. Giglberger, L. E. Golub, V. V. Belkov, S. N. Danilov, D. Schuh, C. Gerl, F. Rohlfing, J. Stahl, W. Wegscheider, D. Weiss, W. Prettl, and S. D. Ganichev, Phys. Rev. B **75**, 035327 (2007).

Chapter 3

Differential Transmission

3.1 Introduction

As the switching rates in electronic and opto-electronic devices are pushed to higher frequencies, it is crucial to probe carrier dynamics in semiconductors on femtosecond time-scales. Understanding the dynamical behavior of nonequilibrium carriers created by intense laser pulses can provide important information about different scattering mechanisms. Time resolved spectroscopy will allow us to understand the relaxation of photoexcited carriers; where after the initial photoexcitation, the nonequilibrium population of electrons and holes relax by a series of of scattering processes including, carrier-carrier and carrier-phonon scattering. The reported carrier scattering rates in semiconductors range from a few to thousands of femtoseconds [1].

For direct optical transitions, far from the exciton resonances, the absorption coefficient can be written as [1]:

$$\alpha = \alpha_0(1 - f_e - f_h) \tag{3.1}$$

Where f_e and f_h are the electrons and holes distribution functions; respectively and α_0 is the linear absorption coefficient in the absence of state filling. Using femtosecond short pulses, a narrow band of states can be excited, and as time progresses, the carrier-carrier interaction results in thermalization of the carrier distribution. In a longer time scale, by lattice-carrier interaction, the photoexcited carriers can reach equilibrium.

The energy-dependent absorption coefficient and the spectrum of pump pulses determine the initial carrier distribution, formulated as following [2, 3]:

$$\Delta\alpha(t) \propto \frac{-1}{\omega} \int d\hbar\omega \int dt\prime N(\hbar\omega, t - t') \sum |H_\nu(\hbar)|^2 \rho(\hbar\omega)[f_e(\hbar\omega, t') + f_h(\hbar\omega, t')] \tag{3.2}$$

Where $N(\hbar\omega, t - t')$ describes the transient photon-energy, $f(\hbar\omega, t')$ is the time dependent distribution of the electrons and holes for different photon energy, $|H_\nu(\hbar)|$ is the optical matrix element, and ρ_ν is the joint density of states for optical transitions. If the sample is thin compared to the absorption length, the differential transmission is directly proportional to the absorption change [2, 3], $\Delta T/T_0 \approx \Delta\alpha d$, where $\Delta\alpha$ is the induced absorption and d is the sample thickness.

Here we present several differential transmission schemes to probe carrier/spin dynamics in the InSb films where the spin-polarized currents were reported earlier in chapter 2.

3.2 Differential Transmission

Differential transmission (DT) provides information on the carrier relaxation time and can be extracted from experimental measurements, by subtracting the measured transmissions at the positive time delay from the transmission at the negative time delay T_0, dividing by T_0:

$$\Delta T(t) = \frac{T(t) - T_0}{T_0} \tag{3.3}$$

In our degenerate DT measurements, the laser source was a difference frequency generator (DFG), which mixes the signal and idler beams from an optical parametric amplifier (OPA). The OPA itself was pumped by an amplified Ti:sapphire oscillator with a repetition rate of 1 KHz. The pulses had a duration of $\sim$ 100 fs defining the resolution of the measurements. The differential transmissivity as a function of the time delay between the pump and probe pulses, using a liquid N2-cooled MCT detector was measured. Our experimental setup for a degenerate DT measurement, is featured in Figure 3.1.

In this scheme, the output pulses from the DFG, were passed through a beam splitter with a roughly 60:40 transmission-to-reflection ratio. The reflected beam, as the probe beam, was passed through a delay stage consisting of a retroreflector, mounted on computer control moving stage. The transmitted beam was directed through a set of mirrors to adjust the temporal overlap of the pump/probe beams. For Spin-Polarized DT measurements, both beams were passed through identical tunable quarter waveplates (ALPHALAS GMBH Model). Before focusing the pulses on the sample, the probe beam was filtered in order to

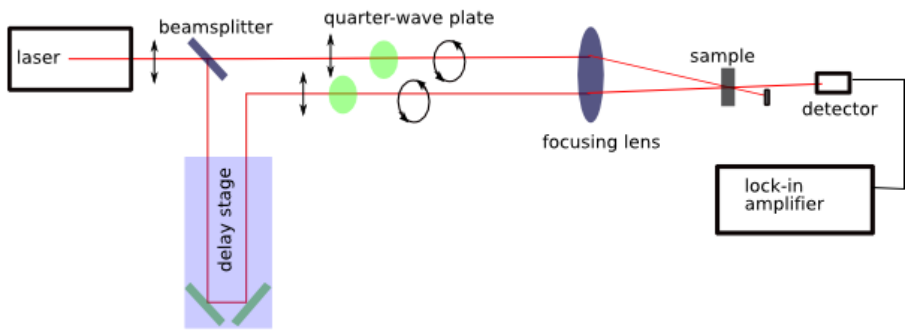

Figure 3.1: Experimental setup for our Degenerate Differential Transmission measurements. The laser source was a difference frequency generator (DFG) generating MIR pulses with a repetition rate of 1 KHz. The pulses had a duration of $\sim$ 100 fs defining the resolution of the measurements. A liquid N2-cooled MCT detector measured the transmissivity.

keep the pump:probe ratio about 1000:1. Both beams were focused onto the sample with a parabolic mirror with a spot size of around 150 μm for probe and slightly larger for the pump.

3.2.1 Degenerate Differential Transmission

In a degenerate pump/probe measurement the optical injection of carriers in semiconductors, following by the fast relaxation in the bands, can result in a saturation of the band-to-band absorption. High population of the photo-excited carriers can lead to formation of an electron-hole plasma which can alter the optical properties. [4]. For large densities of non-equilibrium photo-excited carriers, the exchange interactions between the electrons (or holes) in the same spin state arise due to spatial overlap of the wave functions, as well as the

correlations between charged particles of opposite spins or opposite charges and the same spins. The combination of these effects can result in the bandgap renormalization. The absorption change due to the band filling effect is always negative, whereas the bandgap renormalization results in a redshift in the absorption edge and an increase in absorption coefficient for a fixed photon energy.[5]

In addition, due to the Pauli exclusion principle, photoexcited electrons in the conduction band and holes in the valence band can reduce the interband optical transitions via the band and state filling. This leads to a decrease in the absorption, and a corresponding increase in the transmission, which is referred to as bleaching.[5]

The degenerate DT in our InSb/GaAs films was dominated by the photo-induced bleaching. The examples of the measurements are presented here. Figure 3.2 demonstrates two reproducible DT traces for the InSb/GaAs film at 290 K with the pump/probe fixed $\lambda = 3.1\mu$m. Two decay components are evident with an initial relaxation around 1-2 ps. The signal is not completely relaxed to the initial ($t < 0$) level in a time longer than 5 ps.

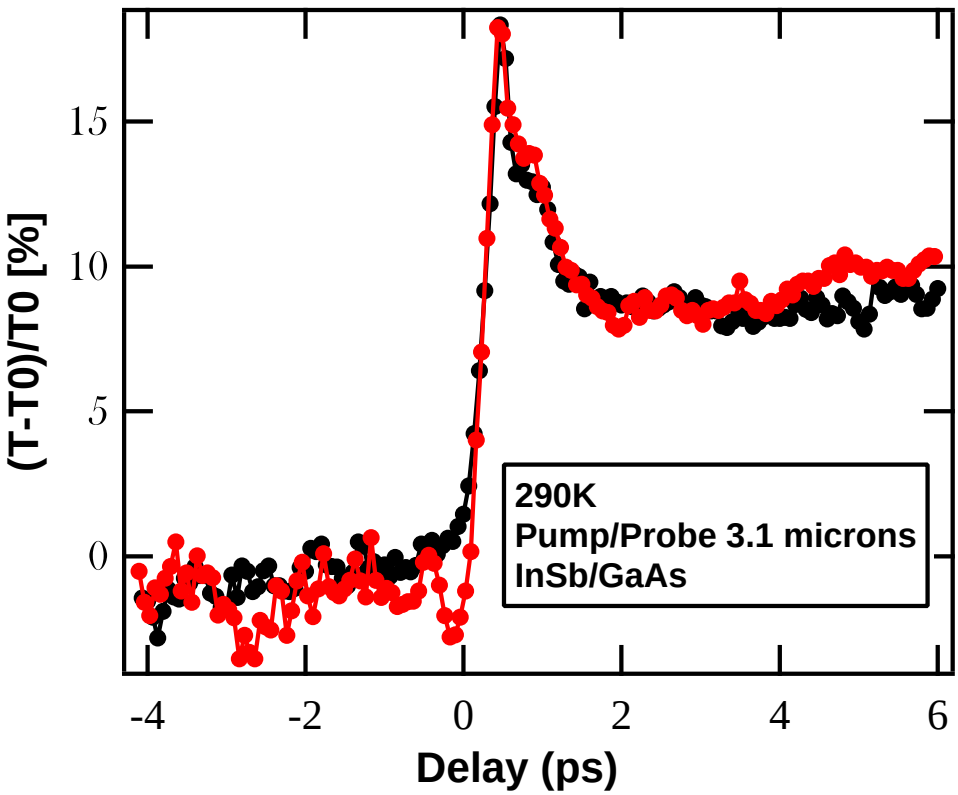

Figure 3.2: Differential transmission in the InSb/GaAs film at 290 K with the pump/probe fixed $\lambda = 3.1\mu$m. The carrier dynamic is dominated by bleaching. Two decay components are evident, with an initial relaxation around 1-2 ps. The signal is not completely relaxed to the initial ($t < 0$) state in a time longer than 5 ps.

The DTs in the InSb/GaAs film, for several pump/probe wavelengths in MIR, are plotted in Figure 3.3. For the measurements at 3.1 and 3.4 μm, the long relaxation components, were fit to exponential functions. The DT change at 3.3 μm was much smaller compared to the other wavelengths and didn't show an exponential decay.

An example of the DT at 77 K is plotted in Figure 3.4. Similar to the measurement at 290

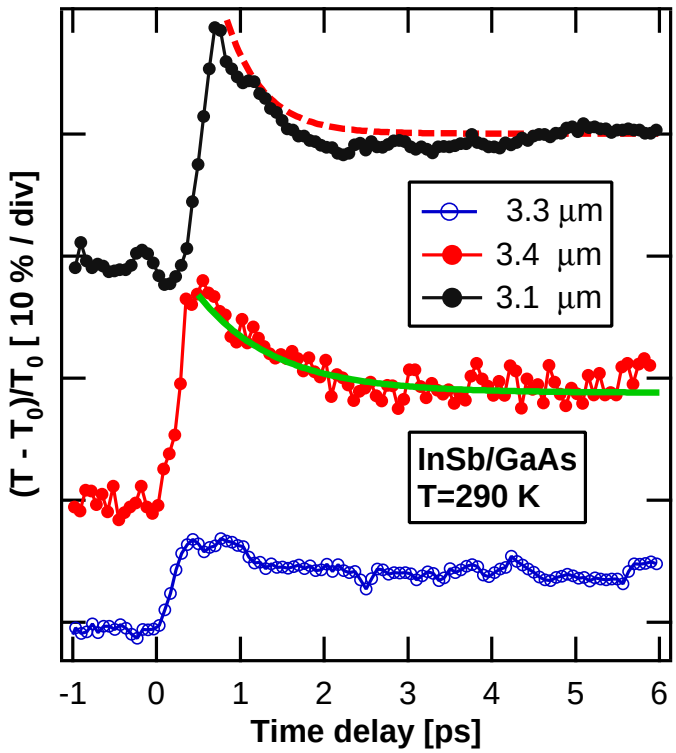

Figure 3.3: Differential transmission in the InSb/GaAs film at 290 K for different MIR wavelengths. For 3.1 and 3.4 μm, the long relaxation components were fit to exponential functions. The differential transmission change at 3.3 μm was less than 10 % and didn't show an exponential decay.

K, an initial fast relaxation of $\sim$ 2 ps following by a non exponential component is evident. The initial change in the DT is a factor of two larger than the observed changes at 290 K. The pump/probe pulses were fixed at 3.1 μ.

We repeated the degenerate DT measurements on an InSb/InP film where similarly, the photo-induced bleaching, dominated the carrier dynamic. In this sample, with identical experimental conditions as for InSb/GaAs film, the observed DTs were several order of the

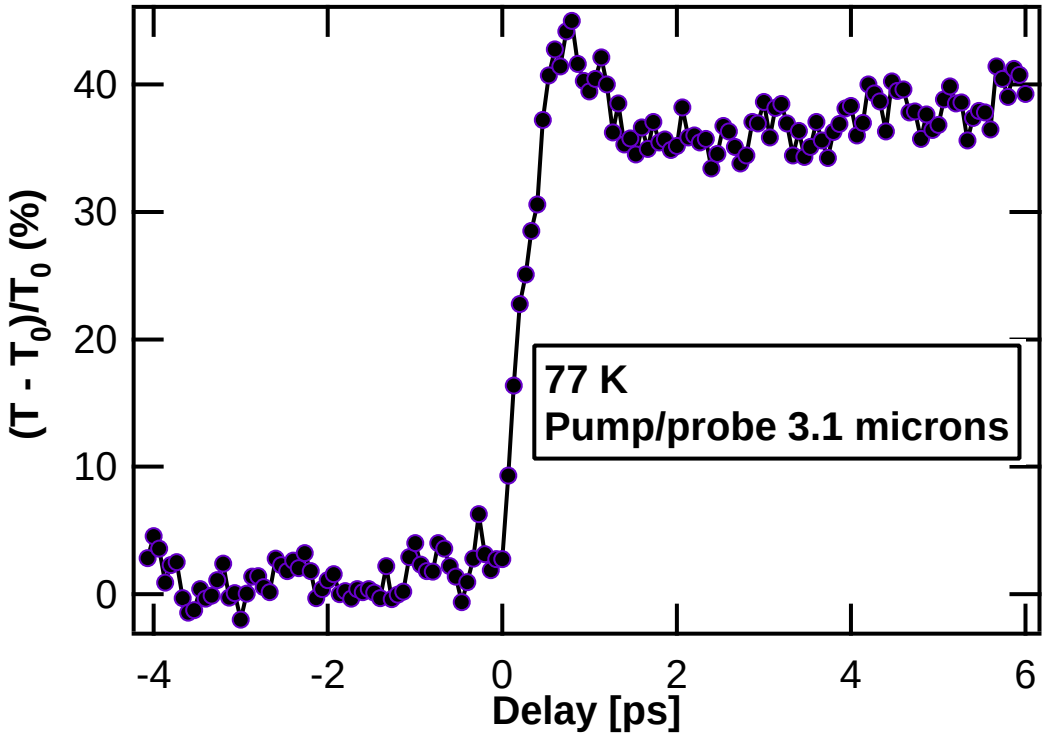

Figure 3.4: An example of the degenerate differential transmission at 77 K demonstrating a photo-induced bleaching. The pump/probe pulses were fixed at 3.1 μm.

magnitudes larger. The measurement for 3.1 and 3.3 μm are presented in Figure 3.5.

In order to further understand the carrier relaxation dynamics in these structures in the absence of photo-induced bleaching, we developed a non-degenerate DT technique where the pump/probe pulses were from different sources.

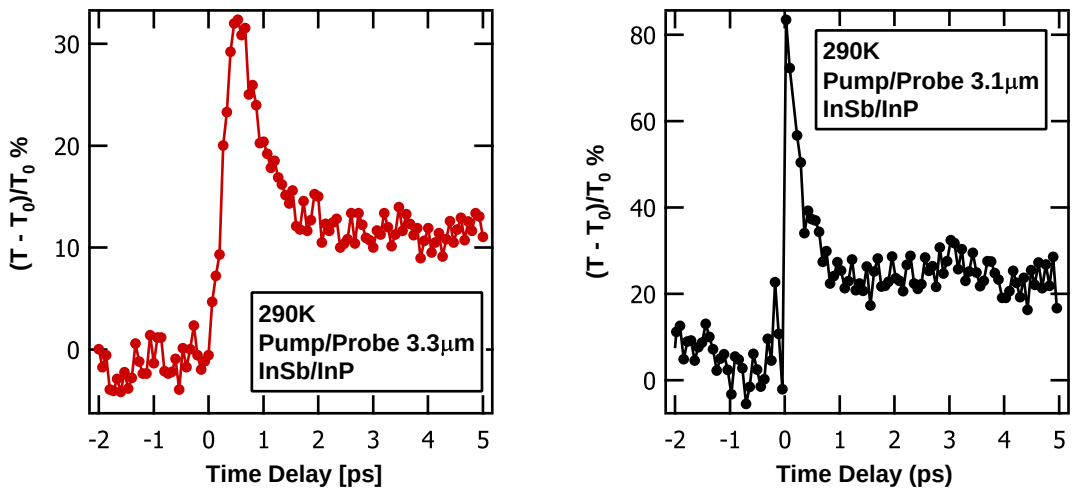

Figure 3.5: Degenerate Differential transmission at 290 K for an InSb film grown on InP substrate. The carrier dynamic demonstrated a similar pattern as the InSb/GaAs film.

3.2.2 Non-degenerate Differential Transmission

In a non-degenerate scheme when the pump pulses are above the band-gap, electrons that are sufficiently energetic have the possibility to scatter between the X, L, and Γ valleys in the conduction band resulting in a longer and more complex relaxation dynamics. In addition, due to the differences in effective masses, electrons in the satellite valleys have lower mobilities compared to the ones in the Γ valley. Understanding the intervalley scattering is important for phenomena such as the Gunn effect defining the behavior of several high-speed devices where electrons are transferred from one valley in the conduction band to another valley.

As shown in Figure 3.6 for InSb, the X and L valleys with the Eg_L =0.63 eV and Eg_X = 0.93 eV are accessible in the NIR optical range.

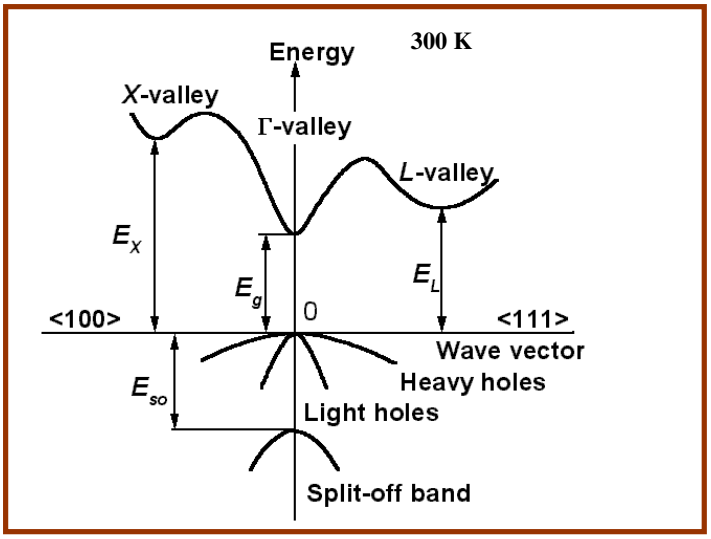

Figure 3.6: Band structure of bulk InSb at 300 K. The X, L, and Γ valleys are measured from the top of valence band. Adapted from http://www.ioffe.ru/SVA/NSM/ Semicond/InSb/Figs/921.gif

Figure 3.7 shows examples of our Non-degenerate Differential Transmission where the carriers are created by NIR pulses fixed at 800 nm above the InSb fundamental gap and probed by MIR pulses. The pump fluence is on the order of 5 mJ-cm^{-2} corresponding to a photo-excited carrier density of $\sim 5x10^{18}cm^{-3}$. The carriers were captured in the QW in a time scale of less than 1 ps. The selected MIR probe pulses allowed to probe the relaxation far from the excitation region and closer to the gap. As shown in 3.7, the differential transmission in this pump/probe regime is dominated by free carrier absorption.

Power dependence of the non-degenerate DT in InSb/GaAs film for the probe fixed at 3.467 μm, presented in Figure 3.8. For several possible pump intensities, we didn't observe a

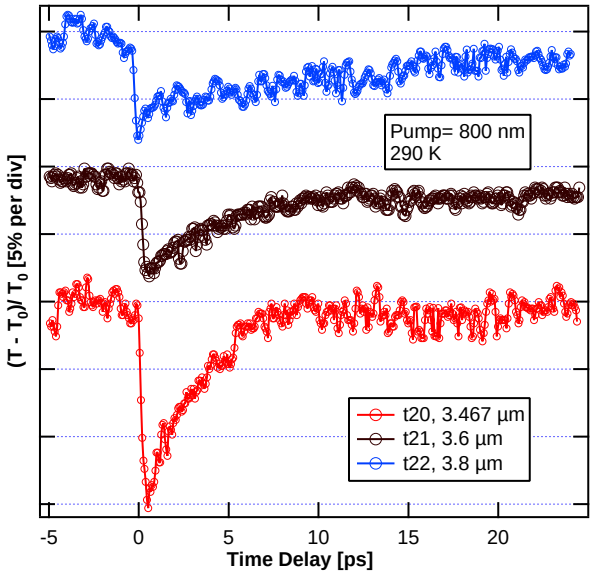

Figure 3.7: Two color Differential transmission. The carriers were created by NIR pulses fixed at 800 nm above the band gap of InSb and probed by MIR pulses. The pump fluence was on the order of 5 mJ-cm^{-2} corresponding to a photo-excited carrier density of $\sim 5 \times 10^{18} cm^{-3}$. Electrons that are sufficiently energetic have the possibility to scatter between the X, L, and Γ valleys in the conduction band, resulting in a longer relaxation time.

strong modification of the carrier relaxation time.

Figure 3.9 demonstrates the two-color DT measurements on the InSb (S360) QW, used in the spin-polarized current studies in Chapter 2. The carriers were captured in the QW in a time scale of $\sim$ 800 fs and not fully relaxed in a time scale longer than 20 ps. The selected MIR probe pulses, allowed us to probe the optical transitions only in the InSb well and avoiding the $Al_xIn_{1-x}Sb$ barrier layer. This fact is supported by earlier measurements that determined the concentration and temperature dependence of the fundamental energy gap

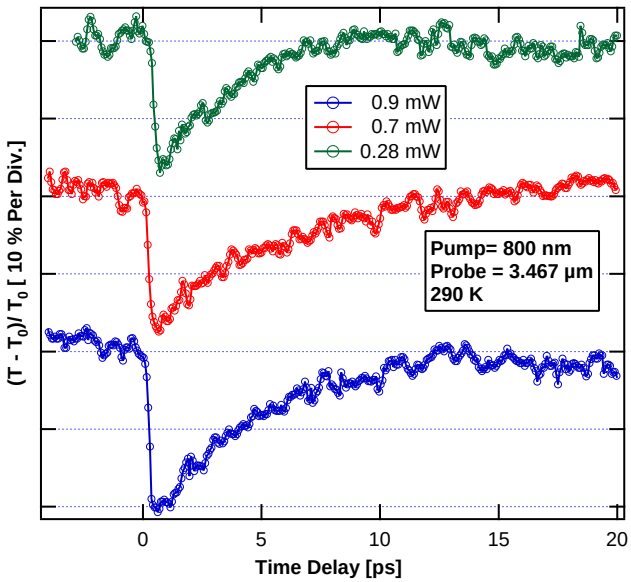

Figure 3.8: Power dependence of the two color Differential transmission measurements in the InSb/GaAs film.

in $Al_xIn_{1-x}Sb$ [6]. The sample structure is described in chapter 2.

3.2.3 Spin Polarized Differential Transmission

In III-V Zinc-Blend semiconductor structures, the transition probability from the heavy hole band is three times larger than the ones involved the light hole band. If the electrons in the conduction band are partially polarized where the polarization can be defined as: [13]:

$$P_n = \frac{(n_+ - n_-)}{(n_+ + n_-)}, \tag{3.4}$$

where $n_+(n_-)$ are the density of electrons for $m_j = 1/2$ (antiparallel $m_j = -1/2$).

If the light and heavy holes are degenerate then the recombination with unpolarized holes

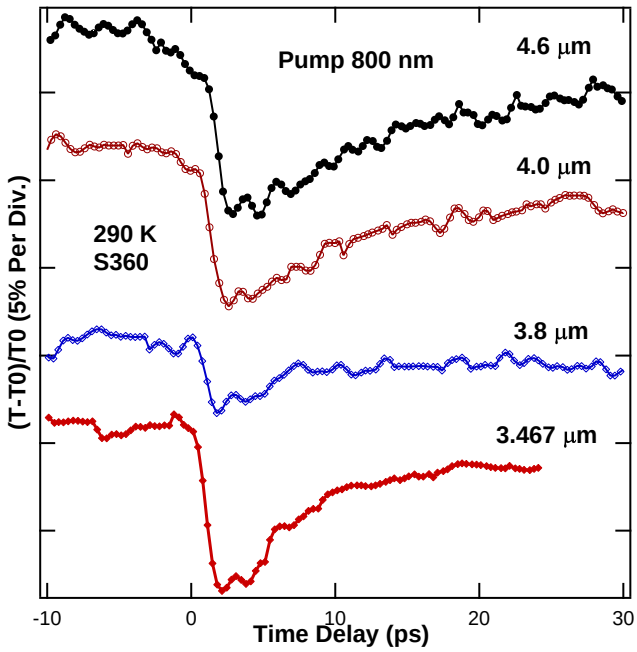

Figure 3.9: Two-color differential transmission measurements at 290 K. The pump excitation was fixed at 800 nm and the MIR probe beams were tuned at different possible interband transitions. Adapted from G. A. Khodaparast, M. Bhowmick, M. Frazier, R. N. Kini, K. Nontapot, T. D. Mishima, M. B. Santos, B. W. Wessels, Proceedings of SPIE Vol. 7608, 76080O (2010).

will result the polarization of the emitted radiation :

$$P_{circ} = \frac{(n_+ + 3n_-) - (3n_+ + n_-)}{(n_+ + 3n_-) + (3n_+ + n_-)} = -\frac{P_n}{2} = \frac{1}{4}. \tag{3.5}$$

We extended the DT measurements to probe the spin relaxation in the InSb films. The spin-polarized electrons were created/probed using circularly polarized pulses in the MIR. By monitoring the transmission of a weaker, delayed probe pulse, that has the same circular

polarization (SCP) or opposite circular polarization (OCP) as the pump pulse, the optical polarization P(t), proportional to the spin polarization, can be measured [8]:

$$\Delta P(t) = \frac{SCP - OCP}{SCP + OCP} \tag{3.6}$$

The spin polarized DT will show an exponential decay, with decay constant equal to the spin relaxation time. The optical polarization can be related to the spin lifetime as $P(t) = P_0 exp(-t/T1)$. where the magnitude of P_0 is a constant and can be 0.25 at best for bulk III-V semiconductors. [8]

The differential transmissivity as a function of the time delay between the pump and probe pulses for InSb/GaAs and InSb/InP at 290 K are shown here. A liquid N2-cooled MCT detector was used to measure the photo-induced transmission. In this pumping regime, both samples demonstrated relaxations in the sub-picoseconds. The spin-polarized photo-excited carrier density was on the order of $5 \times 10^{18} cm^{-3}$.

We probed the relaxations further in a lower fluence regime where the pump/probe were tuned in NIR creating photo-excited carrier densities in the order of $2 \times 10^{16} cm^{-3}$. In this scheme, the source of the pump and probe beams were a Ti-sapphire laser which generated (NIR) pulses with duration of $\sim$ 100 fs, at a repetition rate of 80 MHz, and average power of about 900 mW. The laser beam was split using a beam splitter into a pump (90%) and probe (10%) beam. A $\lambda/4$ plate was used to circularly polarize the pump beam to create spin polarized carriers and a $\lambda/2$ rotated the linearly polarized plane of the probe beam by 45°.

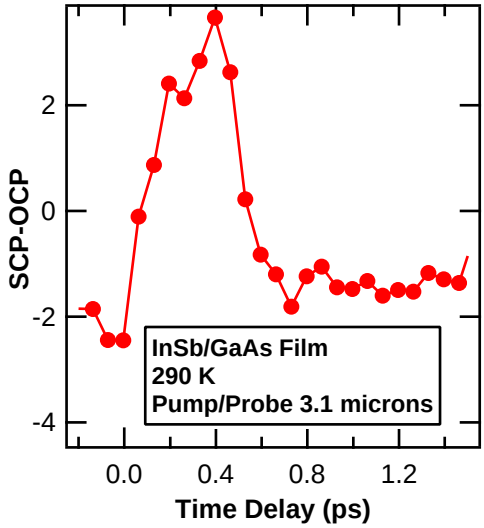

Figure 3.10: Spin Polarized Differential transmission of InSb/GaAs at 290 K. The pump/probe were fixed at 3.1 μm.

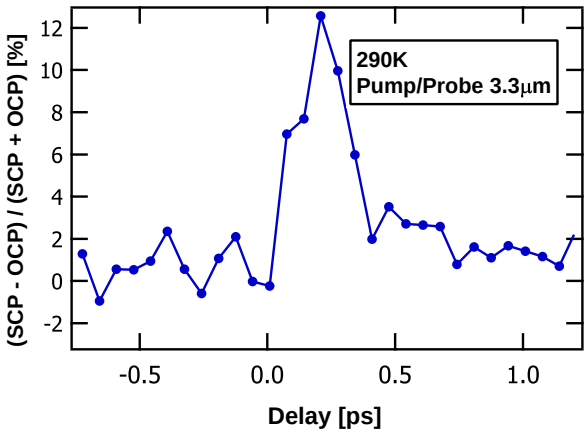

Figure 3.11: Spin Polarized Differential transmission of InSb/InP at 290 K. The pump/probe were fixed at 3.3 μm. The experimental conditions were the same as the measurements on the InSb/GaAs film.

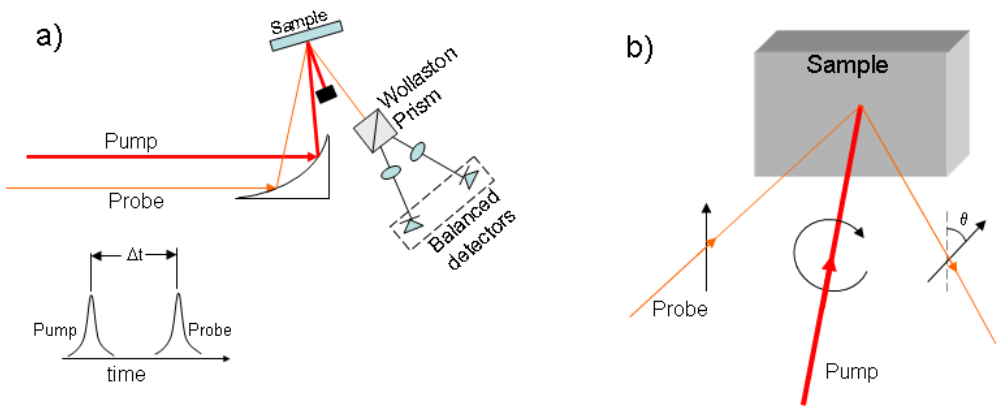

Figure 3.12: Schematic representation of the experimental setup used for time resolved MOKE experiments. The pump beam was circularly polarized and the probe beam was linearly polarized with the plane of polarization rotated 45 degrees. A Wollaston prism was used to split the reflected probe beam into the s- and p- components and detected using balanced detectors.

3.3 MOKE

3.3.1 Faraday Rotation

Linearly polarized light interacting with a material can experience a rotation of the transmitted and reflected light as a function of the magnetization of the material. For polarized light transmitted through the material, this rotation is known as Faraday rotation; the effect was first seen in the measurements performed by Faraday in 1845, with polarized light passing through glass immersed in a magnetic field. Rotation occurs when the path of the light is

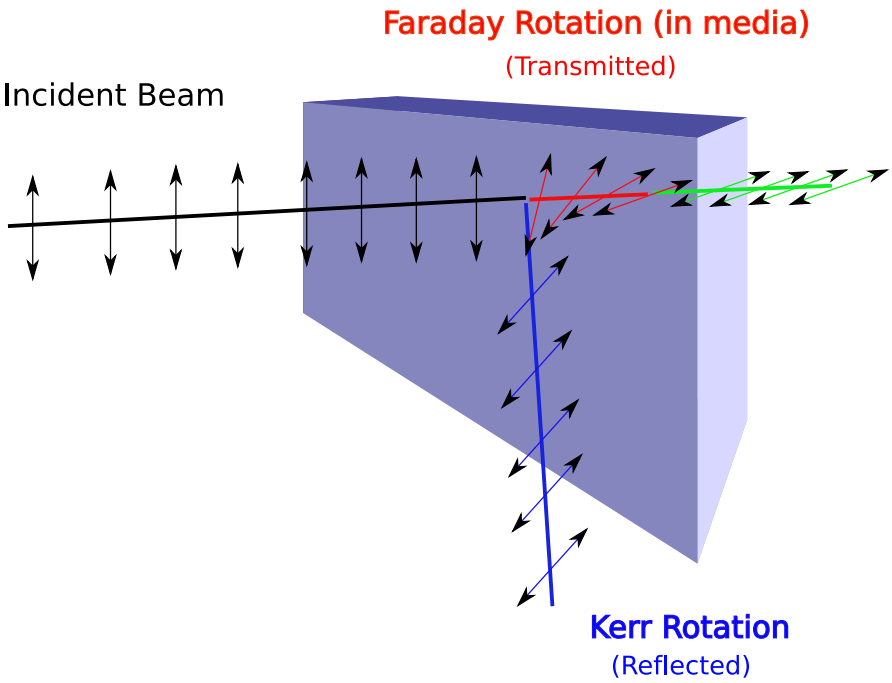

Figure 3.13: Rotation of polarization of light transmitted (Faraday) and reflected (Kerr) from a material. For transmitted light, The plane of polarization is rotated through an angle dependent on field strength and path length through the material. Reflected light experiences a Kerr rotation analogous to the Faraday rotation.

parallel to the applied field; the rotation [in a diamagnetic material] is given by

$$\theta_f = VHL \tag{3.7}$$

where θ_f is the angle of rotation, L the distance traveled by the light along the field, H the magnitude of the field, and V the Verdet constant: a property of the material given as the rotation per unit field strength per unit length. [9]

3.3.2 Kerr Rotation, MOKE

The magneto-optical Kerr effect (MOKE) is the analogous effect for reflected light; Kerr rotation is the change in the polarization of light upon reflection from a material possessing a magnetization. The Kerr rotation arises from the different optical coefficents for left-handed and right-handed circularly polarized light:

$$\eta_k + i\theta_k = \frac{-(\kappa^+ - \kappa^-)}{2n(n^2 - 1)} \tag{3.8}$$

where η_k and θ_k are the Kerr ellipticity and Kerr rotation, κ^+ and κ^- are the optical susceptibilities for right-handed (σ^+) and left-handed (σ^-) circularly polarized light, and n the index of refraction. [9] The $\kappa^+ - \kappa^-$ term is proportional to the magnetization; therefore, the Kerr rotation is a result of the magnetization, which can be an external field and/or an intrinsic magnetization (either spontaneously or optically induced). For time resolved MOKE measurements, a circularly polarized pump pulse is used to excite a population of spin-polarized electrons [as a consequence of the selection rules for inter-band absorption in semiconductors]. The spin-polarized electrons act as a net magnetization that decays as the spins relax. The Kerr rotation of a linearly polarized pump pulse is then measured as a function of the time delay between pump and probe pulses, which gives the spin relaxation time.

The MOKE signal originates from the difference between the optical coefficients of a material for left and right circularly polarized light which is proportional to the magnetization produced by the circularly polarized pump [10]. There are three different configurations of

MOKE, depending on the relative directions of the magnetization respect to the plane of incidence, as shown in Fig. 3.14. For the direction of the magnetization (a) parallel to the surface normal, (b) parallel to the surface and in the plane of incidence, or (c) parallel to the surface and perpendicular to the plane of incidence, MOKE is defined as (a) the polar , (b) the longitudinal, or (c) the transverse, Kerr, respectively. Using a Wollaston prism, the

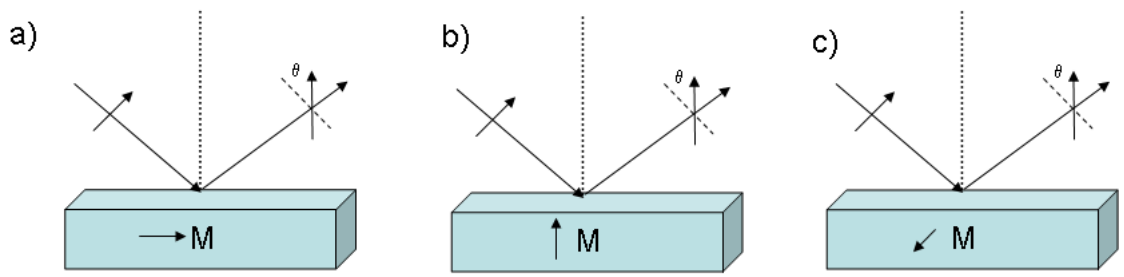

Figure 3.14: For the direction of the magnetization (a) parallel to the surface normal, (b) parallel to the surface and in the plane of incidence, or (c) parallel to the surface and perpendicular to the plane of incidence, MOKE is defined as (a) the polar , (b) the longitudinal, or (c) the transverse, Kerr; respectively.

reflected NIR pulses were separated into s- and p- components which are orthogonal and have equal intensities in the equilibrium spin density state. In the presence of non-equilibrium spin polarized carriers, the MOKE signal reflects the intensity difference between the s- and p- components of the reflected probe pulses. We monitored the signals using a Si balanced detector and a lock-in amplifier. In addition, under the same experimental conditions, the carrier dynamic was measured by probing the change of the transient reflectivity as a function of time delay.

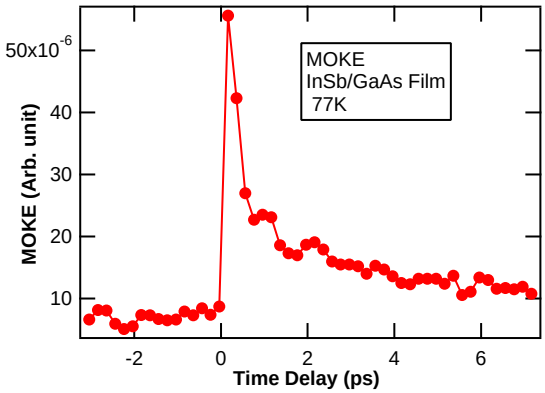

Figure 3.15: MOKE measurements of InSb/GaAs film at 77 K representing the spin relaxation time longer compared to the high fluence regime.

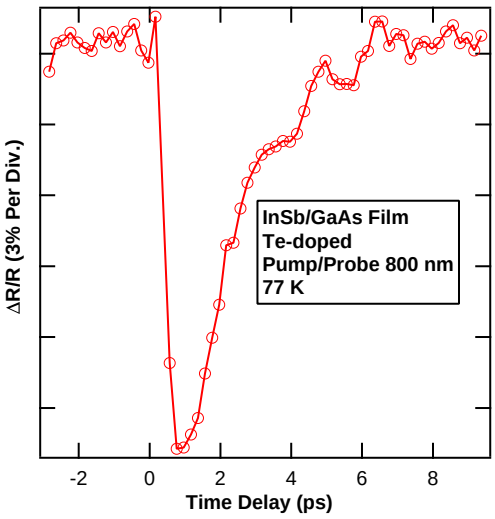

Figure 3.16: Degenerate Differential Reflectivity on InSb/GaAs at 77 K, under the same experimental condition as the MOKE measurements, representing the carrier relaxation. The initial sharp increase in the differential transmission can result from free carrier Drude absorption.

3.4 Experimental components

Ti:Sapphire laser

A Ti:Sapphire (titanium sapphire) laser contains a Sapphire (Al_2O_3) crystal doped with Titanium ions. Ti:Sapphire lasers are typically pumped with another laser such as Argon-ion laser or frequency-doubled Nd:YAG. The Ti-sapphire laser used in this work (Mia Tai, manufactured by Spectra physics, Inc.) generates NIR pulses with duration of 100 fs, tunable from 750 nm to 850 nm, with a repetition rate of 80 MHz, and an average power of about 900 mW.

Chirped pulse amplifier

Chirped pulse amplification (CPA) is widely used technique to amplify femtosecond pulses. The CPA used in this work (Legend-F, manufactured by Coherent Inc.) stretches 800 nm laser pulses from a Ti:Sapphire laser by a factor of 10^6 before amplifying the pulses. The CPA can generate linearly polarized pulses with the wavelength centered at 800 nm and energy pulses as high as 1 mJ with the repetition rate of 1 kHz.

OPA and DFG

An OPA can convert the output laser pulses from a CPA to tunable pulses in MIR. A small fraction of the laser pulses from CPA is focused into a non linear optical material to generate

white light. The rest of the beam is focused and recombine with the white light inside a non-centro-symmetric crystal. This process of nonlinear mixing is called optical parametric amplification (OPA) where different output wavelengths can be generated by varying the crystal angle.

The output of the OPA consists of two tunable beams called the Signal and the Idler. The Signal and Idler outputs are tunable from 1150-1600 nm and 1600-2999 nm respectively. Using the difference-frequency mixing of the Signal and Idler outputs from the OPA, tunable laser pulses in the mid-IR spectral region can be generated. The wavelength of the DFG can be controlled by changing the angle of the DFG crystal.

3.4.1 Optical components

Wave plate

In order to adjust the polarization of the pump and probe pulses, the beams were directed through waveplates. The waveplates consist of a birefringent crystal with a given thickness, with a "fast" axis parallel to the optical axis and a "slow" axis perpendicular to the optic axis, such that the index of refraction is smaller for light polarized parallel to the fast axis than it is for light polarized parallel to the slow axis ($n_{fast} < n_{slow}$). The components of the light polarized along the slow axis will have a retardation compared to the light polarized along the fast axis, with a relative phase difference

$$\Gamma = 2\pi\Delta n\frac{L}{\lambda} \tag{3.9}$$

where L is the plate thickness and λ the wavelength of the incident light. When the phase shift is one-quarter wavelength, the waveplate acts as a quarter waveplate, which can be used to change a linearly polarized light to circularly polarized. For a phase shift of one half wavelength, a half waveplate can rotate the plane of a linearly polarized light by 45°.

For our measurements, the waveplates used were tuned by varying the angle of incidence (to vary the thickness presented to the laser pulses) to act as a quarter wave plate at the particular wavelength. The waveplate operating on the pump beam was set with the fast axis at 45° to the linearly polarized light; the probe beam waveplate was also set with fast axis at 45° to the pulses; either parallel to the pump waveplate (SCP) or perpendicular (OCP).

Wollaston Prism

A Wollaston prism, invented by William Hyde Wollaston [12], can be used to separate randomly polarized or unpolarized light into two orthogonal, s- and p- polarized beams. The Wollaston prisms are typically made from two orthogonal calcite prisms, glued together into two right triangle prisms as shown in Figure. 3.17.

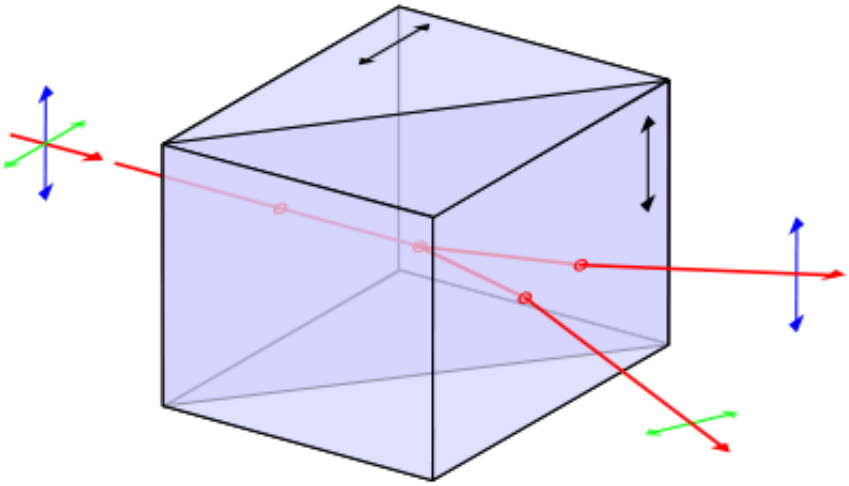

Figure 3.17: A Wollaston prism can separate unpolarized light into two orthogonal, s- and p- polarized components[12].

After randomly polarized light beams enter the Wollaston prism, the prism can separate them into two orthogonal polarized rays. The angle of divergence between the two separated beams depends on the prisms' wedged angle and the wavelength.

Detectors

In order to detect MOKE signal, the reflection of the polarized probe pulses were reflected off the sample and entered a Wollaston prism, which divides the beam into s- and p- polarized components. The orthogonally polarized beams were focused with an identical pair of lenses into a balanced detector. The initial linear polarization was adjusted at zero time delay to give equal s- and p- polarizations from the Wollaston prism, resulting in zero signal at the negative time delay. At a later time delay, an effective polarization due to the spin-

polarized carriers can result in a Kerr rotation, and a subsequent imbalance in the s- and p-components. The imbalance was measured by the balanced detector and fed into a lock-in amplifier, which detects the signal components coincident with the pulse arrival (using the chopping frequency as the input frequency).

The balanced detector used was a Nirvana Auto-Balanced Photoreceiver (model 2007, New Focus, Inc). This is comprised of a pair of equivalent detectors and differential preamplifier. The differential preamplifier acts to subtract the photocurrents of the detectors, and amplify the result. Noise common to both detectors is subtracted out, while the imbalance between the photocurrents (due to an imbalance in s- and p- polarization) is amplified. [13]

3.5 Summary

We measured carrier and spin relaxations in InSb based material systems. In the InSb thin films, the degenerate DT measurements were dominated by photo-induced bleaching, with a two-component relaxation: a fast component ∼1-2 ps and a slow component surviving beyond 5 ps. In the non-degenerate schemes where the pump and probe were tuned at different wavelengths, the DT was dominated by the free carrier absorption. In case of the InSb QW, the carriers were created by NIR pulses fixed at 800 nm above the band gap of the $Al_xIn_{1-x}Sb$ and InSb layers in the QW, and probed by MIR pulses. The photo-excited carriers were captured in the QW in a time scale of $\sim$ 800 fs and not fully relaxed in a time scale longer than 20 ps. Electrons that are sufficiently energetic have the possibility to

scatter between the X, L, and Γ valleys, resulting in a longer relaxation time and a more complex relaxation pattern. Using circularly-polarized pump and probe pulses, the spin-polarized DT measurements were performed, indicating a spin relaxation time on the order of 500 fs, much faster than the observed time scale using the MOKE measurements.

Bibliography

[1] W. H. Knox, C. Hirlimann, D. A. B. Miller, J. Shah, D. S. Chemla, and C. V. Shank, Phys. Rev. Lett **56**, 1191 (1986).

[2] D. W. Bailey, C. J. Stanton, K. Hess, Phys. Rev. B. **42**, 3423 (1990).

[3] C. J. Stanton, D. W. Bailey, K. Hess, Phys. Rev. Lett. **65**, 231 (1990).

[4] P.P. Paskov and L.I. Pavlov, Appl. Phys. B **54**, 113(1992).

[5] Semicond. Sci. Technol. **7**, 124(1992).

[6] N. Dia, F. Brown, R. E. Doezema, S. J. Chung, K. J. Goldammer, and M. B. Santos, Appl. Phys. Lett., 73 (1998) 3132

[7] Igor Zutic, Jaroslav Fabian, S. Das Sarma, Rev. Modern Phys. **76**, 323 (2004)

[8] Thomas F. Boggess, J. T. Olesberg, C. Yu, Michael E. Flatte , and Wayne H. Lau, Appl. Phys. Lett., 77 (2000) 1333.

[9] A. K. Zvezdin and V. A. Kotov, *Modern Magnetooptics and Magnetooptical Materials* (IoP Publishing, Bristol, 1997).

[10] A. K. Zvezdin and V. A. Kotov, *Modern Magnetooptics and Magnetooptical Materials* (IoP Publishing, Bristol, 1997).

[11] G. A. Khodaparast, M. Bhowmick, M. Frazier, R. N. Kini, K. Nontapot, T. D. Mishima, M. B. Santos, B. W. Wessels, Proceedings of SPIE Vol. 7608, 76080O (2010)

[12] `http://en.wikipedia.org/wiki/Wollaston_prism`

[13] http://www.newfocus.com/products/documents/manuals/20X7_Manual_RevC.pdf

Chapter 4

Magneto-Optical Kerr Effect in InMnSb Structures

4.1 Introduction

In light of the growing interest in spin-related phenomena and devices, ferromagnetic semiconductors have garnered attention as a possible candidate for utilizing both spin and charge properties. Current research activities in the area of ferromagnetic semiconductors have mainly been focused on III-Mn-V alloys with small lattice constants and large valence band effective masses, such as GaMnAs [1, 2, 3]. Various theoretical models have been proposed to explain the actual mechanism of ferromagnetism in III-Mn-Vs, but the microscopic mechanism is still a matter of controversy [1, 4, 5, 6, 7, 8, 9]. In particular, much has been said

regarding the inverse correlation of T_c and the lattice parameter, which has led to considerable research on GaMnN and related alloys. It is therefore important in this context to explore the opposite extreme of the III-Mn-V ternaries i.e., InMnSb, which has the largest lattice constant in this family of materials [10, 11].

An earlier work by Nontapot *et al.* [14] indicated the absence of a strong temperature dependence in the spin relaxation of the ferromagnetic InMnSb. This fact was attributed to lack of Mn ions' interaction with the photo-excited carriers; a similar observation was reported in a study by Kimel *et al.* [18] in GaMnAs. Therefore, both groups attributed the observed photo-induced carrier/spin dynamics entirely to the relaxation of photo-excited electrons in the conduction band.

In III-Mn-V ferromagnetic semiconductors the s-d coupling with the localized Mn ions is significantly weaker than p-d exchange coupling characterizing the valence band. This effect may have important consequences for applications of InMnSb in developing spin based devices, since this alloy has much higher hole mobility than the other III-Mn-V ferromagnetic semiconductors. However, strong temperature and field dependence have been reported by Wang *et al.* in InMnAs. [19].

In this work, we measured the magneto-optical response of optically-excited spins and carriers in a series of ferromagnetic InMnSb films in the presence of external magnetic fields. The observed carrier/spin dynamics in our InMnSb films were found to be more influenced by the nature of the samples, rather than by the Mn concentrations and the external fields. Before presenting the experimental observations, several theoretical models describing spin

relaxation will be presented.

4.2 Spin Relaxation

For a population of spin-polarized carriers, the spin relaxation time is the time necessary for the spins to lose their alignment. The two mechanisms (important to this discussion) of spin relaxation are the Elliot-Yafet (EY) mechanism, and the D'yakonov-Perel (DP) mechanism.

4.2.1 Elliot-Yafet Mechanism

In a crystal lattice, the Schrödinger equation can be written as

$$H\psi = [\frac{p^2}{2m} + V]\psi = E\psi \tag{4.1}$$

where V represents a regular, periodic potential with solutions taking the form of the Bloch functions

$$\psi = u_k e^{ik\cdot r} \tag{4.2}$$

where the u_k's have the same periodicity as the potential. Accounting for spin-orbit coupling gives a new term for the Hamiltonian as:

$$H' = \frac{\hbar}{4m^2c^2}(\nabla V \times p)\cdot\sigma \tag{4.3}$$

where the σ's are the Pauli spin matrices. This results in the wave functions being linear combinations of the spin eigenstates

$$u_k e^{ik\cdot r} = [a_k\,|\uparrow\rangle + b_k\,|\downarrow\rangle]e^{ik\cdot r} \tag{4.4}$$

It is important to note that these Bloch functions are not spin eigenstates. Typically, the spin-orbit coupling can be treated as a perturbation, such that the states can be considered "mostly up" or "mostly down", with a small amplitude for the opposite spin eigenstate. Elliot [12, 13] posited that scattering interactions could cause spin "up" states to flip to spin "down" states (and vice versa), at a rate

$$\frac{1}{T_1} \propto \frac{b^2}{\tau} \tag{4.5}$$

where b is the amplitude of the spin down state and τ is the momentum relaxation rate describing non-spin-flip scattering and relaxation. Yafet [13] demonstrated the temperature dependence of the relaxation time in this mechanism. Accounting for scattering from spin-orbit interactions with phonons and impurities, and scattering from interfaces, the relaxation rate follows the temperature dependence shown by resistivity:

$$\frac{1}{\tau_p(T)} \approx \langle b^2 \rangle \rho(T)$$

At high temperatures, $1/T_1 \propto T$, while at very low temperatures $1/T_1 \propto T^5$. More realistic relations can be developed by taking appropriate approximations for phonon's contribution and band structure. For III-V materials, one can find a relaxation time for conduction band electrons with energy E_k

$$\frac{1}{\tau_s(E_k)} = A \left(\frac{\Delta_{so}}{E_g + \Delta_{so}} \right)^2 \left(\frac{E_k}{E_g} \right)^2 \frac{1}{\tau_\rho(E_k)}$$

where Δ_{so} is the spin-orbit splitting,E_g the band-gap energy, E_k the kinetic energy, τ_p the momentum scattering time, and A is a numerical constant of order of 1, determined by

the dominant scattering mechanism [13]. It can be noted from the above equation that the relaxation rate due to the EY mechanism increases as Δ_{so} increases; for materials with large spin splitting (like InSb), EY becomes an important mechanism for spin relaxation.

4.2.2 D'yakonov-Perel Mechanism [13]

In crystals with lack of inversion symmetry, the spin-orbit interaction lifts the degeneracy between spin up and spin down states: for a given wavevector k, $E_{\uparrow}(k) \neq E_{\downarrow}(k)$, while $E_{\uparrow}(k) = E_{\downarrow}(-k)$ still holds. This non-degeneracy is equivalent to a k-dependent magnetic field (B(k)) about which the spins precess. The Hamiltonian describing this spin precession is

$$H(k) = \frac{1}{2}\hbar\hat{\sigma} \cdot \Omega(k) \tag{4.6}$$

$$\Omega(k) = \frac{e}{m}B(k) \tag{4.7}$$

where Ω is the Larmor frequency and σ the Pauli matrices. Momentum scattering changes the state from k to k' resulting in spin precession about the new field B(k'). The spins eventually lose their alignment, relaxing at a rate proportional to the momentum relaxation time

$$\frac{1}{T_1} \propto \tau \tag{4.8}$$

The manner in which the dephasing occurs is governed by the limiting cases $\tau_p\Omega_{avg} \geq 1$ and $\tau_p\Omega_{avg} \leq 1$: in the first case, the apparent field is stable, and the spins precess one full

revolution before scattering, with the dephasing time τ_p. In the second limit, the effective field fluctuates, with an exponential decay of the spin alignment described by a tensor $1/\tau_{s,ab}$

$$\frac{1}{\tau_{s,ii}} = \gamma_l^{-1}\tau_p(\bar{\Omega}^2 - \bar{\Omega}_i^2) \tag{4.9}$$

$$\frac{1}{\tau_{s,ij}} = -\gamma_l^{-1}\tau_p(\bar{\Omega}_i\bar{\Omega}_j) \tag{4.10}$$

where γ_l describes the effectiveness in randomization of Larmor frequency by scattering. For bulk III-V semiconductors, the Larmor frequency is given by

$$\Omega(k) = \alpha\hbar^2(2m_c^3E_g)^{-1/2}\vec{\kappa} \tag{4.11}$$

where

$$\kappa_x = k_x(k_y^2 - k_z^2)\ et\ cycl. \tag{4.12}$$

describes the lattice wavevector components. α is the Rashba parameter, giving the strength of the spin splitting. In 2-D III-V structures, there are two distinct contributions from the Hamiltonian: a bulk inversion asymmetry (BIA) term, and a structure inversion asymmetry (SIA) term. Both terms provide different effects to τ_s and contribute to spin splitting with a linear k dependence.

BIA The bulk Dresselhaus spin splitting is responsible for the BIA term, by treating k as an operator $\hat{k} = -i\nabla$. The spin dephasing tensor can be evaluated , resulting in:

$$\frac{1}{\tau_{s,ij}} = \frac{(\delta_{ij}Tr\hat{\nu} - \nu_{ij})}{\tau_s^0(E_k)}$$

$$\frac{1}{\tau_s^0(E_k)} = \frac{\alpha^2\hbar^2(k_n^2)^2}{2m_c^2E_g}E_k\tau_p(E_k)$$

where the tensor ν is related to the orientation of the crystal axes. [13]

SIA The SIA term arises from the Bychkov-Rashba spin splitting; the Hamiltonian is still formed from the precession vector, with a new precession given by:

$$\Omega(k) = 2\alpha(k \times n)$$

with α the spin-orbit coupling. [13] Similarly as for BIA, a spin relaxation time can be calculated as:

$$\frac{1}{\tau_s^0} = 4\frac{\alpha^2 m_c}{\hbar^2} E_k \tau_p \tag{4.13}$$

4.2.3 Earlier Studies

InMnAs - Wessels *et al.* **[15]** : Wessels *et al.* [15] examined the ferromagnetic properties of InMnAs samples grown by metalorganic vapor phase epitaxy (MOVPE); a technique that allows for growth of some materials at higher temperatures than molecular beam epitaxy. For InMnAs, ferromagnetic films were grown with a $T_c = 330K$. Figure 4.2.3 shows I-V curves for an InMnAs p-n junction, showing a linearly changing magnetoresistance for varying field between 0-18 T without saturation.

InMnSb - Parashar *et al.* **[16]** : Parashar *et al.* [16] investigated ferromagnetism in InMnSb films grown by MOVPE. Figure 4.2.3 shows hysteresis curves at room temperature in two films with different Mn concentrations. Figure 4.2.3 shows a) Hall resistivity and b) anomalous Hall resistivity at T=4 K and T=298 K versus field. The presence of a room temperature AHE indicated both spin-polarized carriers and anisotropy between the spin states induced by spin-orbit coupling; the observed hysteresis indicates room-temperature ferromagnetism that is carrier-mediated rather than from MnSb precipitate.

GaMnAs - Yee *et al.* **[17]** : Yee *et al.* investigated carrier dynamics in Ga(,Mn)As with the Mn content ranging from 2 to 5 percent. Using a degenerate pump-probe technique, with the wavelengths fixed at 780 nm, the time resolved absorption was measured. In the time scale of $\sim$ 1 ps, the authors observed a sharp drop in the absorption, after which the absorption signal gradually recovers to its equilibrium position. This behavior in the

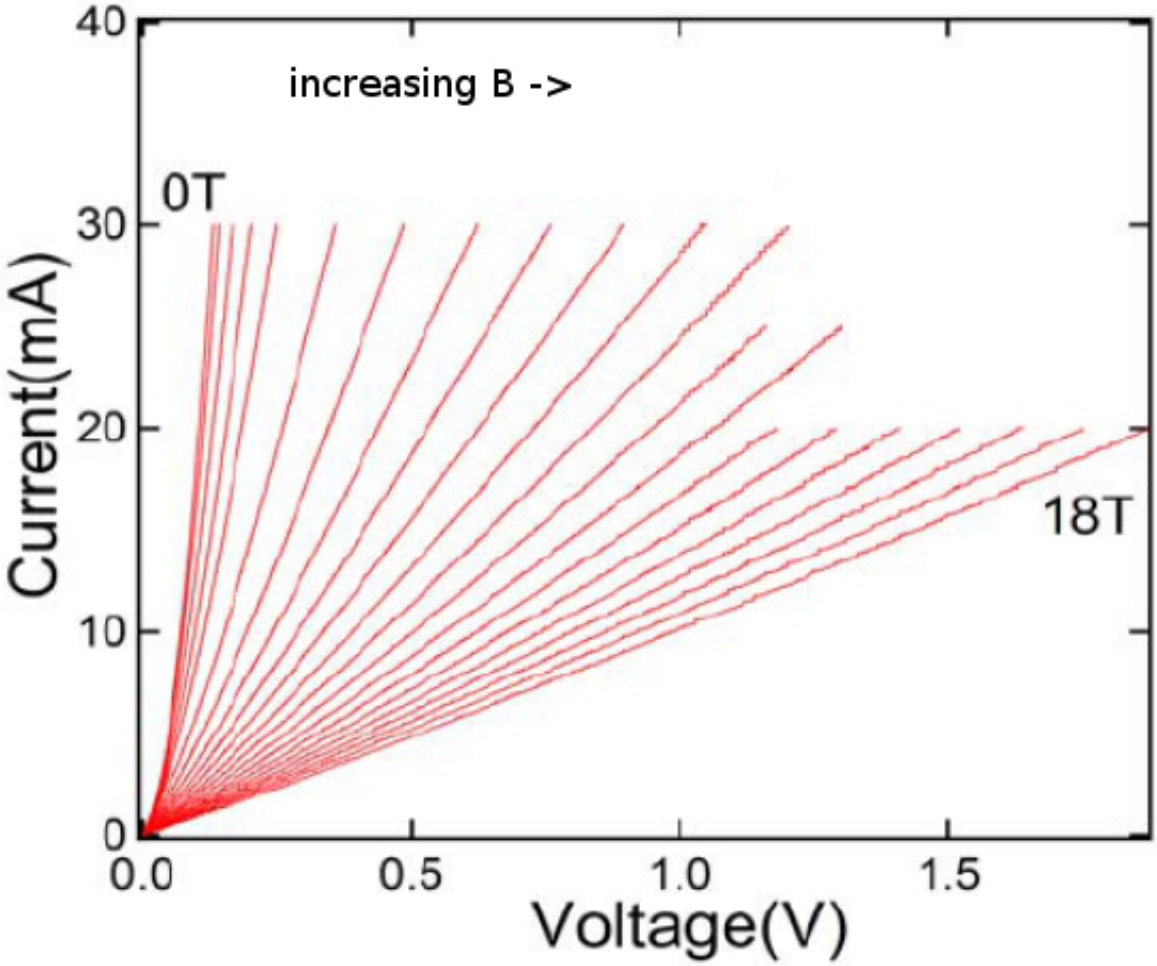

Figure 4.1: Current-voltage graph for an InMnAs p-n junction at 300 K, for varying field up to 18 T; indicating a giant magnetoresistance, with magnetoresistance linear in field without saturation. Adapted from B. W. Wessels "InMnAs Thin Films and Heterostructures", **Handbook of Spintronic Semiconductors** (World Scientific, 2010). *in press*

absorption was attributed to trapped carriers in defects re-excited by probe photons.

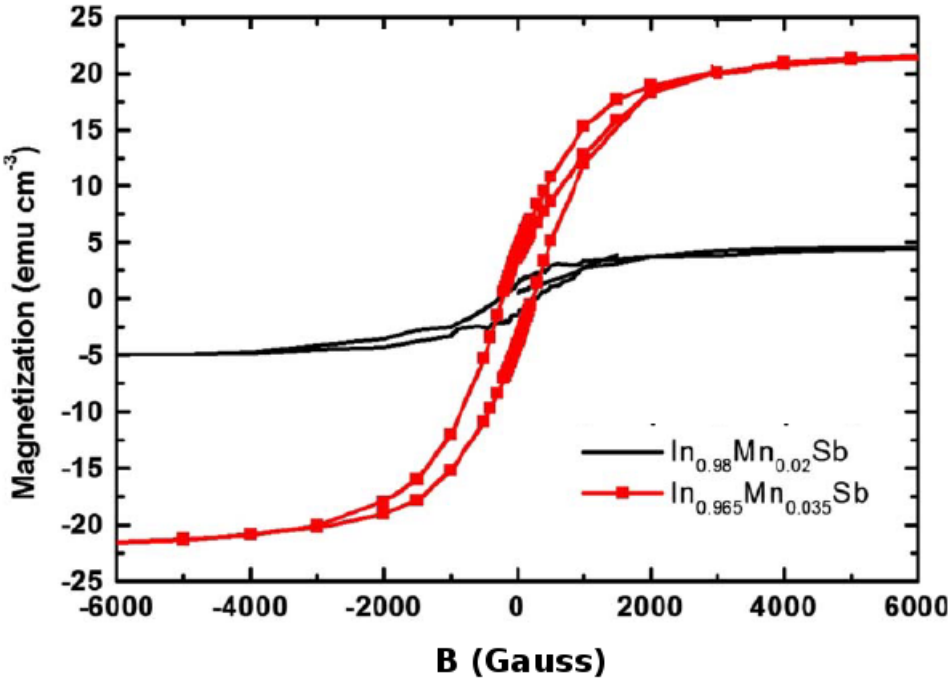

Figure 4.2: Hysteresis curves in InMnSb at room temperature, for two films with different Mn concentrations. Adapted from N. D. Parashar, N. Rangaraju V. K. Lazarov S. Xie and B. W. Wessels, Phys. Rev. B **81** *in press*

GaMnAs-Kimel *et al.* [**18**] : Kimel *et al.* performed MOKE measuremetns on Ga(Mn)As using a Ti:Sapphire laser operating between 1.49 and 1.66 eV (∼850 - 750 mn) with an external magnetic field of up to 100 mT and temperature down to ∼10 K. A relaxation of ∼ 30 ps of the Kerr rotation was seen at T = 10 K and T = 60 K. The long relaxation time, at both low and high temperatures, implies that the Mn ions do not interact with the photo-excited carriers.

InMnAs - Wang *et al.*: Wang *et al.* [19, 20] performed MOKE measurements on an InMnAs/GaSb heterostructure with a Curie temperature $T_c = 60$ K, using a 2 μm pump and 775 nm probe, varying the pump fluence, the sample's temperature, and the external field strength. As shown in Fig. 4.2.3, a strong temperature dependence was observed , with the signal disappearing above the $T_c = 60$ K. Increasing the pump fluence increased the change in the Kerr angle (as demonstrated in Fig. 4.7). The application of a small magnetic field ($\pm$ 0.7 mT, as shown in Fig. 4.8) altered the relaxation, possibly due to a strong interaction between the Mn ions and the photo-excited spins.

InMnSb-Nontapot *et al.* : Nontapot [14] *et al.* had performed measurements on LT-InSb based ferromagnetic and non-ferromagnetic films in different pumping regimes. They observed faster relaxations in the case of higher laser fluences that produce higher photo-generated carrier densities. This fact can be explained by the Elliot-Yafet [12] relaxation mechanism. On the other hand, in the InMnSb samples, varying the sample temperature from above to below the T_C modified the relaxations only slightly, suggesting a possible absence of interaction of photo-induced carriers with Mn ions. The authors attributed the observed photo-induced carrier/spin dynamics entirely to the relaxation of photo-excited *electrons* in the conduction band. In III-Mn-V ferromagnetic semiconductors the s-d coupling with the localized Mn ions is considered to be significantly weaker compared to the p-d exchange coupling, characterizing the valence band.

4.2.4 Experimental Setup

In these measurements, the source of intense near infrared pulses was a Ti:Sapphire laser which produces tunable radiations from 750 nm to 850 nm with a pulse duration of $\sim$ 100 fs and repetition rate of 80 MHz with average power of about 900 mW. A small portion of the beam was used as the probe beam. In order to avoid absorption by the GaAs substrate, we monitored the change in the reflectivity dynamics as a function of the time delay between the pump and the probe. A quarter wave plate was used to circularly polarize the pump beam to excite spin polarized carriers and a half wave plate was used to rotate the linearly polarized plane of the probe beam.

As a result of selection rules for interband transitions, spin-polarized carriers can be created using circularly polarized pump beams. The MOKE signal arises from the difference between the optical coefficients of a material for left and right circularly polarized light which is proportional to the magnetization produced by the circularly polarized pump. The application of external magnetic fields was performed using a split-coil magnet (Oxford Instruments). The magnet was capable of producing fields in the range of $\pm$ 10 T, with a homogeneity of 0.5 % / cm, by means of superconducting coils in a liquid helium bath.[21]

Detectors In the differential transmission measurements, an MCT detector operating at 77 K were used. For the MOKE measurement, the reflection of a linearly polarized probe beam from the sample was separated by a Wollaston prism into s- and p- polarizations. Then the beams were focused by two identical lenses into the two photo diodes of a Si-balance

detector. The Si-balance detector was a Nirvana Auto-Balanced Photo-receiver (model 2007, New focus inc.), composed of a differential preamplifier and a pair of equivalent detectors.

4.3 Samples

The measurements were performed on three InMnSb samples grown by low temperature molecular beam epitaxy with $T_c \sim$ 10 K . The samples were grown on a GaAs substrate, with CdTe layer of $\sim$ 4.5 μm, a buffer layer of InSb (0.1μm), and a 0.23 μm layer of InMnSb. The samples and their characteristics are listed in Table 1. In addition to different T_{Mn}, resulting in nominally different Mn fluxes, the samples during the growth might as well had slightly different substrate temperature, and Sb, and In fluxes. Since properties of III-Mn-V are to a large extent predetermined by the number of compensating defects, such as Mn interstitials, which in turn depend crucially on the growth conditions, the samples grown even at nominally the same conditions but in different days, might not be identical [10, 11, 22, 23].

Photo-induced Carrier Density The density of the optically excited carriers is governed by the absorption coefficient of the material, the volume in which photons are absorbed, and the fluence incident in that area. The number density can be calculated by

$$n = \frac{U}{\hbar\omega}\frac{1}{Sl_0}\left(1 - e^{-\alpha l_0}\right)$$

Sample	Density	Mobility	T_{Mn}	Mn Content
	cm^{-3}	cm^2/Vs	°C	%
InMnSb(A)	2×10^{20}	100	690	2.0
InMnSb(B)	2×10^{20}	100	700	2.0
InMnSb(D)	2×10^{20}	100	720	2.8

Table 4.1: List of the InMnSb samples studied. All samples have 0.23 μm of active layer and are p-type. T_{Mn} is the Mn effusion's cell temperature, which resulted in different Hall resistivities and hysteresis loops.

with U the pulse energy, $\hbar\omega$ the photon energy, S the surface area, l_0 the absorption thickness, and α the absorption coefficient.

Using a pulse power of $U = 10$ nJ and wavelength $\lambda = 800$ nm (typical for our measurements), and a focused spot size with radius of around 0.5 mm, we can calculate a carrier density

$$
\begin{aligned}
n &= \frac{u}{\hbar\omega}\frac{1}{sl_0}\left(1-e^{-\alpha l_0}\right) \\
&= \frac{u}{\frac{hc}{\lambda}}\frac{1}{\pi r^2}\left(\frac{1-e^{-\alpha l_0}}{l_0}\right) \\
&= \frac{10\times10^{-9}j}{\frac{(6.6\times10^{-34}J\cdot s)(3\times10^{8}m/s)}{800\times10^{-9}m}}\frac{1}{\pi(0.5\times10^{-3}m)}\left(\frac{1-e^{-\alpha l_0}}{l_0}\right) \\
&= 5.15\times10^{16}/m^2\left(\frac{1-e^{-\alpha l_0}}{l_0}\right) \\
&= 5.15\times10^{12}/cm^2\left(\frac{1-e^{-\alpha l_0}}{l_0}\right)
\end{aligned}
$$

considering only the active layer of our samples, we may take $l_0 = 1.3\mu m = 1.3 \times 10^{-4} cm$ This gives the carrier density as

$$\begin{aligned} n &= \frac{5.15 \times 10^{12}/cm^2}{1.3 \times 10^{-4} cm} \left(1 - e^{-\alpha l_0}\right) \\ &= 3.96 \times 10^{16}/cm^3 \left(1 - e^{-\alpha l_0}\right) \end{aligned}$$

Finally, using a value of $\alpha = 6.8 \times 10^3/cm$, the exponential term becomes $(1 - exp(-\alpha l_0)) = 0.586$, returning a carrier density $n = 2.32 \times 10^{16}/cm^3$.

4.4 MOKE measurements - results and discussion

Figure 4.11a demonstrates the MOKE signal for the sample D (with 2.8 % Mn) compared to the one observed in the sample A (with 2% Mn), and Fig. 4.11b shows the temperature dependence of the MOKE signal for the sample D. The observed signals for samples A and D show relaxation times of 1 ps and 1.8 ps. We believe the differences are influenced by the samples' individual characteristics as a result of the slight variation in their growth conditions. The data presented in Fig. 4.11b for sample D (with 2.8% Mn) shows no strong temperature dependence below and above the T_c.

Figure 4.12 presents measurements undertaken to investigate the effect of magnetic ordering on the photo-excited carriers. The spin relaxation is measured in a zero magnetic field twice, with the field ramped up in between measurements to well beyond the saturation field strength (H = 0.04 T) to ensure the alignment of the ion spins. With an external field of 0.7 T applied, the before and after traces so no change in the spin relaxation, indicating a lack of strong interaction between the spin of the photo-excited carriers and the spin of the Mn ions.

In order to really demonstrate the insensitivity of photo-exited carriers to the magnetic ordering, we performed time-resolved magneto-optical measurements using a superconducting magnet with optical access. We measured the spin relaxation at zero field and after applying a field. Earlier transport measurements on these structures demonstrated the saturation field of 0.04 T [10, 11], and as shown for the sample A in Fig. 4.12, our typical applied field was

larger (0.7 Tesla in this case). The field was set back to zero during the measurements. The absence of any strong modification in the MOKE signal after aligning the Mn ions implies lack of strong interaction between the ions and the spin of the photo-excited carriers via sp-d exchange interaction unlike to that observed in InMnAs [19].

In addition to the spin-dynamics features, we observed differences in the photo-induced carrier relaxations. Figure 4.13a demonstrates the carrier relaxations at several NIR pump/probe wavelengths. At 800 nm the initial recovery of the signal occurs at $\sim$ 1.3 ps compared to $\sim$ 3.7 ps for the other two wavelengths. One would expect such a wavelength dependence in GaMnAs where both band filling and induced absorption can contribute in the NIR range to the relaxation dynamic[17]; this fails to explain our observations of wavelength dependence; the pump and probe energies used are far larger than the bandgap for InMnSb. In addition the trapped electron states are considered to be formed in the mid-gap where the reabsorption must be insensitive for probe energy ranges used in this work.

A similar wavelength dependence as shown in Fig. 4.13a was observed in the sample A but not in sample D with 2.8% Mn content where the trapped states expect to exist as well. As shown in Fig. 4.13b we were not expecting the photo-induced carriers to interact strongly with the aligned Mn ions after applying an external field above and below the T_c. We see nearly identical traces, indicating no dependence on the temperature or applied field. Similarly, as shown in Fig. 4.14a for sample D (with 2.8% Mn), the temperature dependence of photo-induced carrier density is not significant similar to our earlier observations on InMnSb ferromagnetic films with 2.0% Mn concentration [14]. Lack of temperature and field

dependence has also been reported previously in GaMnAs containing 2% Mn [18].

In order to probe the possible contribution from the CdTe/GaAs layers to our measurements presented, temperature and wavelength dependence of the photo-induced carrier relaxations were measured on a template with CdTe $\sim 4.5\mu m$. No differential reflectivity signal was observed from the template sample in the temperature range of our measurements on the InMnSb films. In addition, as shown in Fig. 4.14b when a signal was detected, the relaxation in the CdTe/GaAs is significantly different compared to the ferromagnetic films. Therefore; neither the picture of trapped states which can explain the wavelength dependence in GaMnAs [17], nor the contribution from the substrate can explain the wavelength dependence observed in the samples A and B.

4.5 Summary

Our measurements investigated the magneto-optical response of optically-excited spins and carriers in a series of ferromagnetic InMnSb to probe the possible contribution of Mn ions to the relaxation dynamics which has been reported in InMnAs [19] with a larger remanent magnetization compared to InMnSb. The observed carrier/spin dynamics in our InMnSb were found to be influenced by the samples' growth conditions, rather than by the Mn concentrations. We observed no significant temperature or field dependence in the relaxation times supporting our earlier argument [14] to attribute the observed photo-induced carrier/spin dynamics entirely to the relaxation of photo-excited *electrons* in the conduction

band where the s-d coupling with the localized Mn ions is significantly weaker compared to the p-d exchange coupling. This effect can have important consequences for applications of narrow gap ferromagnetic semiconductors such as InMnSb in developing spin based devices, since these materials have much higher hole mobility than the other III-Mn-V ferromagnetic semiconductors.

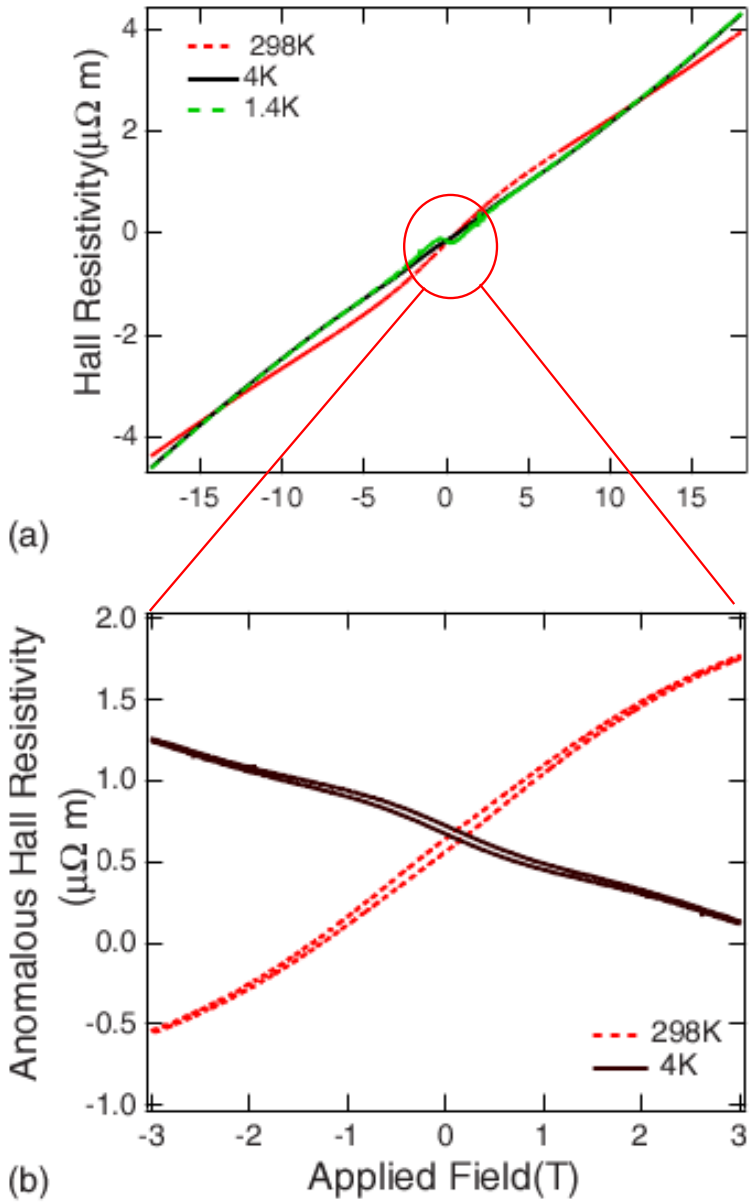

Figure 4.3: A) Hall resistivity vs. applied field in InMnSb at T = 4 K and T = 298 K. B) Anomalous Hall effect (AHE) at low field, separated form ordinary Hall effect; indicating presence of spin polarized carriers and spin-orbit coupling. Adapted from N. D. Parashar, N. Rangaraju V. K. Lazarov S. Xie and B. W. Wessels, Phys. Rev. B **81** *in press*

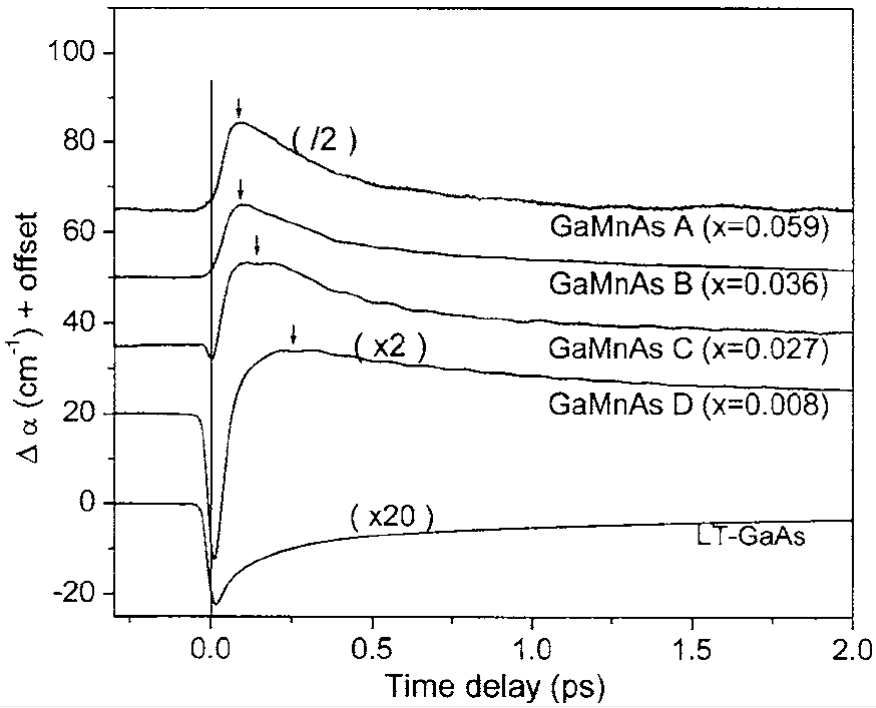

Figure 4.4: Absorption measurements performed by Yee *et al* to investigate carrier dynamics in GaMnAs; the observed pattern of the time resolved absorption implies a re-excitation of carriers trapped in mid-bandgap defects. Adapted from K. J. Yee, D. Lee, X. Liu, W. L. Lim, M.Dobrowolska, J. K. Furdyna, Y.S. Lim, K.G. Lee, Y. H. Ahn, and D.S. Kim, J. Appl. Phys. **98** 113509 (2005).

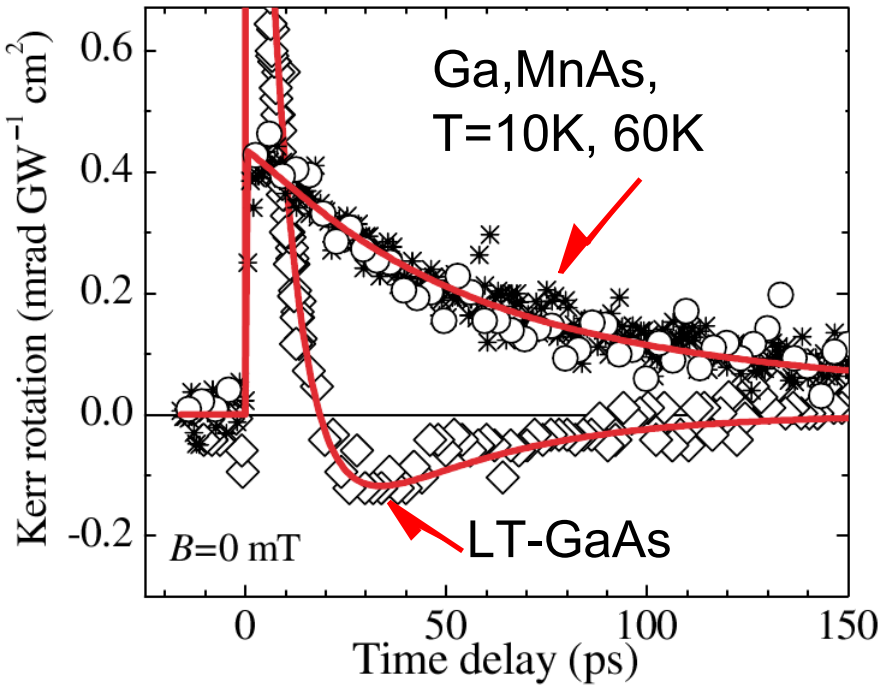

Figure 4.5: MOKE measurements performed by Kimel *et al* on GaMnAs, showing lack of temperature dependence crossing the critical temperature. Adapted from A. V. Kimel, G. V. Astakhov, G. M. Schott, A. Kirilyuk, D. R. Yakovlev, G. Karczewski, W. Ossau, G. Schmidt, L. W. Molenkamp, and Th. Rasing, Phys. Rev. Lett. **92**, 237203 (2004)

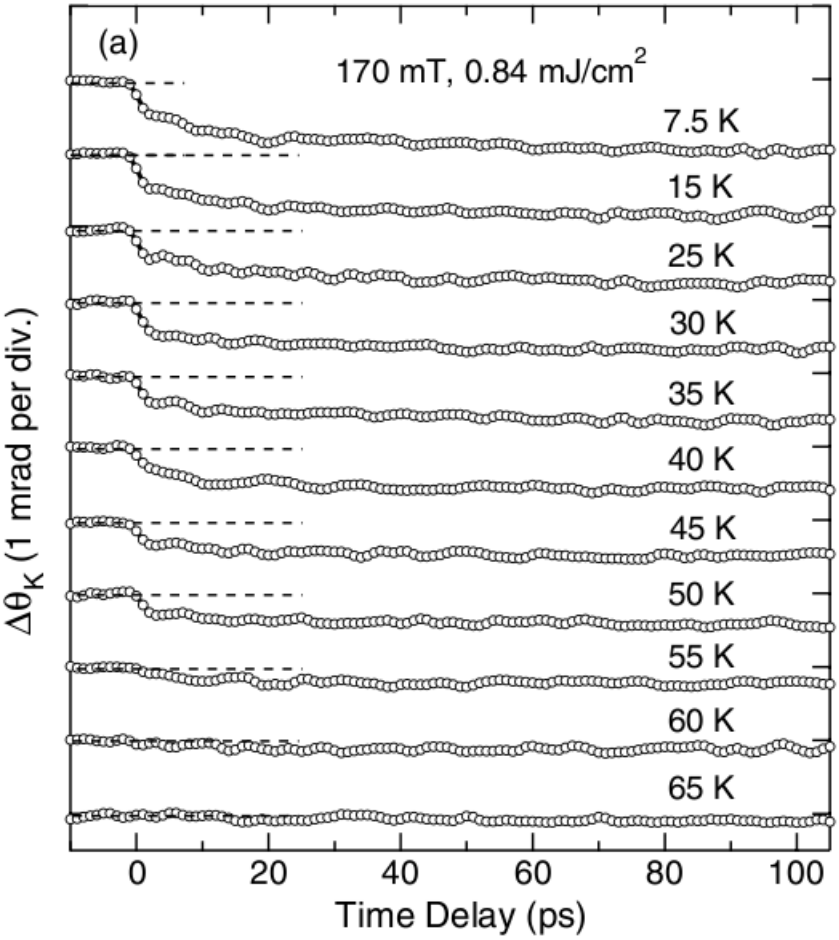

Figure 4.6: Temperature dependence of the MOKE measurements in InMnAs/GaSb. Above T_c, there is no excitation; below, there is a clear temperature dependence, with larger relaxation time at lower temperatures. Adapted from J. Wang, C. Sun, Y. Hashimoto, J. Kono, G. A. Khodaparast, L. Cywinski, L. J. Sham, G. D Sanders, C. J. Stanton, and H. Munekata, J. Phys.: Condens. Matter **18** R501(2006).

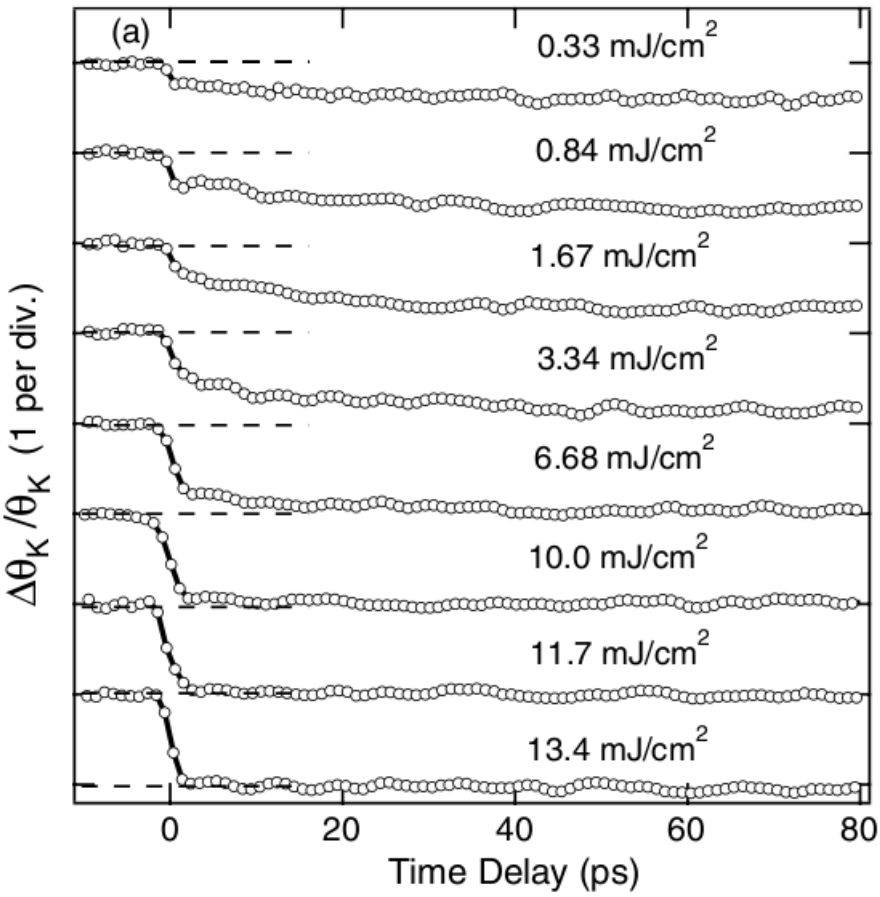

Figure 4.7: The normalized MOKE in the InMnAs/GaSb film, demonstrated a strong dependence to the pump fluence. At low fluence, fast and slow components are both evident; at high fluence, the fast component dominates. Adapted from J. Wang, C. Sun, Y. Hashimoto, J. Kono, G. A. Khodaparast, L. Cywinski, L. J. Sham, G. D Sanders, C. J. Stanton, and H. Munekata, J. Phys.: Condens. Matter **18** R501(2006).

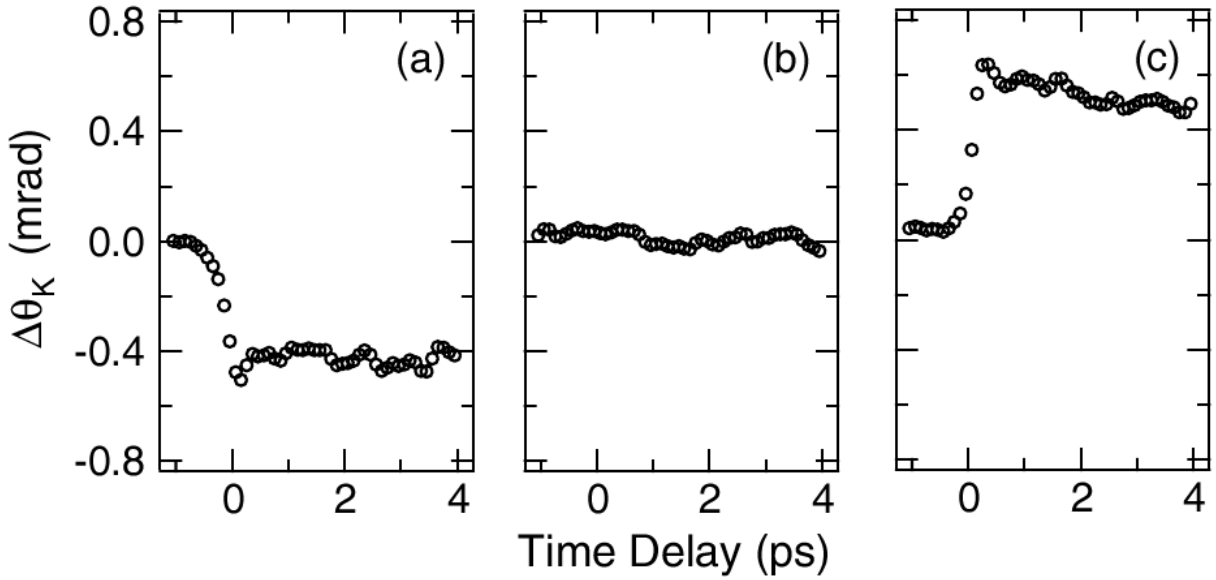

Figure 4.8: Early-time decay of Kerr angle with applied field: a) 7 mT b) 0 mT, c) -7 mT. the relaxation time is altered after applying an external magnetic field, indicating the possible interaction of the aligend Mn ions with the photoexcited spins. Adapted from J. Wang, C. Sun, Y. Hashimoto, J. Kono, G. A. Khodaparast, L. Cywinski, L. J. Sham, G. D Sanders, C. J. Stanton, and H. Munekata, J. Phys.: Condens. Matter **18** R501(2006).

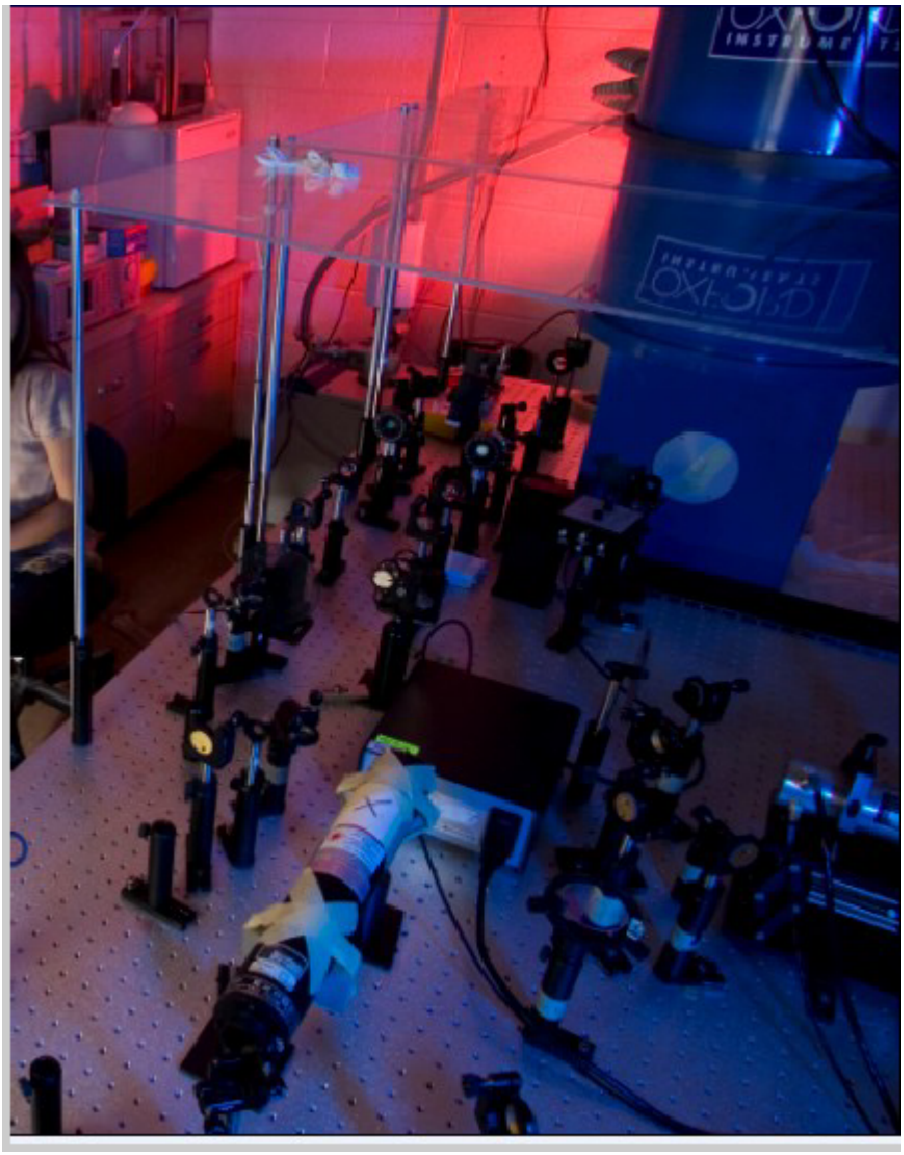

Figure 4.9: Our setup; showing magnet (top right), outside sample (top center), chopper (left), waveplates (center), and balanced detector for MOKE (right)

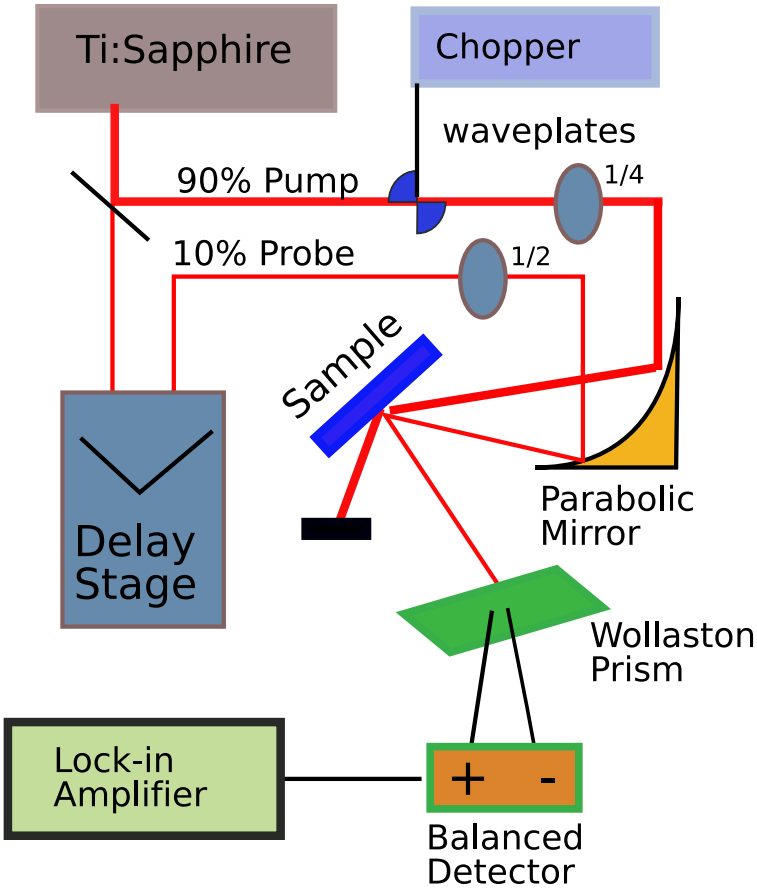

Figure 4.10: Schematic representation of the experimental setup used for the MOKE experiments. The pump pulses were circularly polarized and the probe beams were linearly polarized with the plane of polarization rotated 45 degrees. A Wollaston prism was used to split the reflected probe beam into the s- and p- components and detected using balanced detectors. Spin polarization appears as an imbalance in the detected polarization, which relaxes as the spins relax.

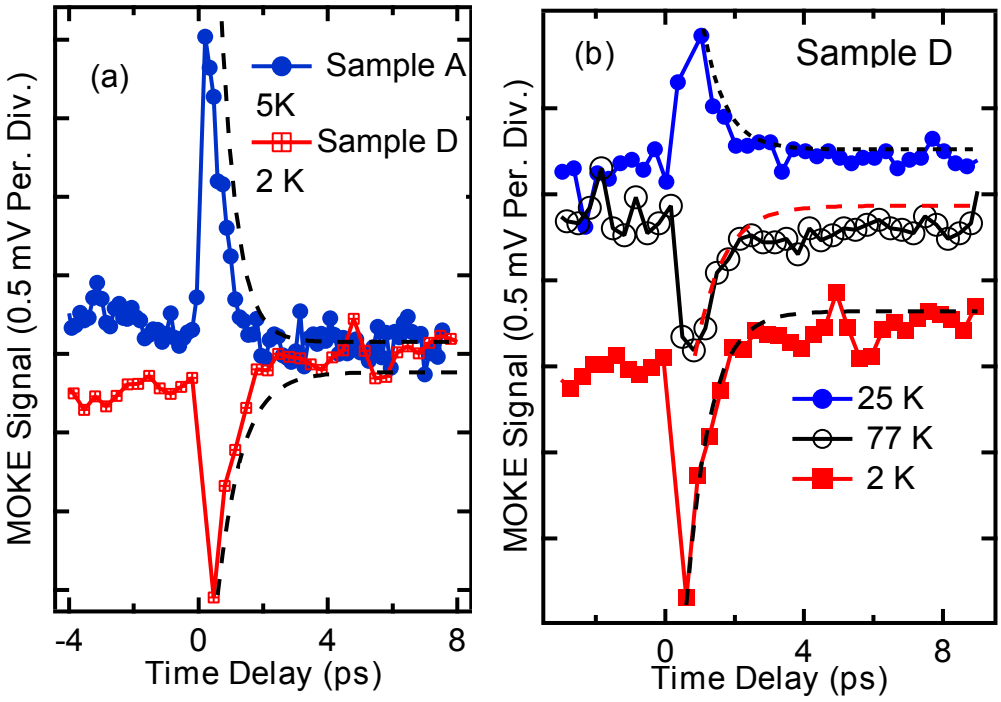

Figure 4.11: MOKE signal in InMnSb. A shows comparision between sample A (2% Mn) and sample D (2.8% Mn) at or below 5K. B shows temperature dependence in the MOKE signal for sample D. Adapted from: M Frazier *et al.* APL 92, 061911 (2008)

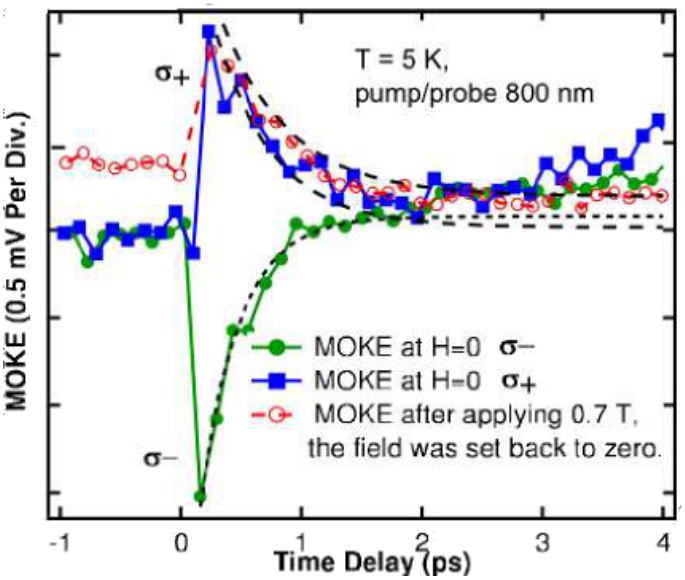

Figure 4.12: Insensitivity of photoexcited carriers to alignment of magnetic ordering of Mn ions, tested by aligning the Mn ions with a strong field between MOKE measurements. Adapted from: M Frazier *et al.* APL 92, 061911 (2008)

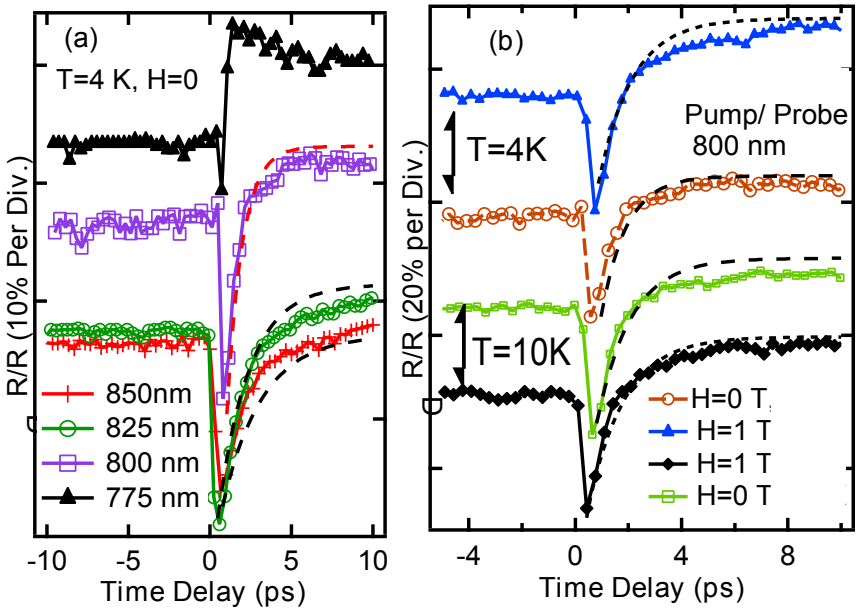

Figure 4.13: a) Wavelength dependence of carrier relaxation in sample B. b) Dependence on applied field below and above T_c. Adapted from: M Frazier *et al.* APL 92, 061911 (2008)

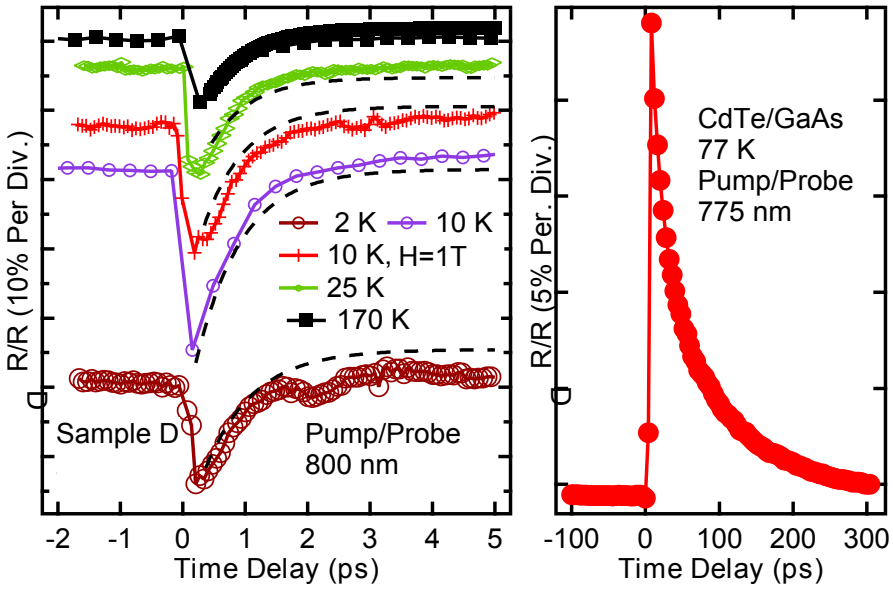

Figure 4.14: a) Temperature dependence of carrier relaxation in sample D b) Relaxation in CdTe template, to rule out effects from CdTe in our samples. Adapted from: M Frazier *et al.* APL 92, 061911 (2008)

Bibliography

[1] T. Dietl, H. Ohno, F. Matsukura, J. Cibert, and D. Ferrand, Science **287**, 1019 (2000).

[2] M. Nazmul, S. Kobayashi, S. Sugahara, and M. Tanaka, Physica E **21**, 937 (2004).

[3] E. Kojima, R. Shimano, Y. Hashimoto, S. Katsumoto, Y. Iye, M. Kuwata-Gonokami, Phys. Rev. B, **68**, 193203 (2003).

[4] H. Akai, Phys. Rev. Lett. **81**, 3002 (1998).

[5] J. Inoue, S. Nonoyama, and H. Itoh, Phys. Rev. Lett. **85**, 4610 (2000).

[6] J. König, Hsiu-Hau Lin, and A. H. MacDonald, Phys. Rev. Lett. **84**, 5628 (2000).

[7] V. I. Litvinov and V. K. Dugaev, Phys. Rev. Lett. **86**, 5593 (2001).

[8] A. Chattopadhyay, S. Das Sarma, and A. J. Millis, Phys. Rev. Lett. **87**, 227202 (2001). Chattopadhyay J. Schliemann and A. H. MacDonald, Phys. Rev. Lett. **88**, 137201 (2002).

[9] Gergely Zaránd and Boldizsár Jankó, Phys. Rev. Lett. **89**, 047201 (2002).

[10] T. Wojtowicz, G. Cywinski, W. L. Lim, X. Liu, M. Dobrowolska, J. K. Furdyna, K. M. Yu, W. Walukiewicz, G. B. Kim, M. Cheon, X. Chen, S. M. Wang, and H. Luo, Appl. Phys. Lett. **82**, 4310 (2003).

[11] T. Wojtowicz, W. L. Lim, X. Liu, G. Cywinski, M. Kutrowski, L. V. Titova, K. Yee, M. Dobrowolska, J. K. Furdyna, K. M. Yu, W. Walukiewicz, G. B. Kim, M. Cheon, X. Chen, S. M. Wang, H. Luo, I. Vurgaftman, J. R. Meyer, Physica E **20**, 325 (2004).

[12] R. J. Elliot, Phys. Rev.**96**, 266 (1954)

[13] Igor Zutic, Jaroslav Fabian, S. Das Sarma, Rev. Modern Phys. **76**, 323 (2004).

[14] K. Nontapot,R. N. Kini, A. Gifford, T. R. Merritt, G. A. Khodaparast, T. Wojtowicz, X. Liu, J. K. Furdyna, Appl. Phys. Lett. 90, 143109 (2007).

[15] B. W. Wessels "InMnAs Thin Films and Heterostructures", **Handbook of Spintronic Semiconductors** (World Scientific, 2010). *in press*

[16] N. D. Parashar, N. Rangaraju V. K. Lazarov S. Xie and B. W. Wessels, Phys. Rev. B **81** *in press*

[17] K. J. Yee, D. Lee, X. Liu, W. L. Lim, M.Dobrowolska, J. K. Furdyna, Y.S. Lim, K.G. Lee, Y. H. Ahn, and D.S. Kim , J. Appl. Phys. **98** 113509 (2005).

[18] A. V. Kimel, G. V. Astakhov, G. M. Schott, A. Kirilyuk, D. R. Yakovlev, G. Karczewski, W. Ossau, G. Schmidt, L. W. Molenkamp, and Th. Rasing, Phys. Rev. Lett. **92**, 237203 (2004).

[19] J. Wang, C. Sun, Y. Hashimoto, J. Kono, G. A. Khodaparast, L. Cywinski, L. J. Sham, G. D Sanders, C. J. Stanton, and H. Munekata, J. Phys.: Condens. Matter **18** R501(2006).

[20] J. Wang, C. Sun, J. Kono, A. Oiwa, H. Munekata, L. Cywinski, L.J.Sham. PRL 95, 167401 (2005)

[21] http://www.oxford-instruments.com/products/low-temperature/opticaland-spectroscopy/spectromag/Pages/spectromag.aspx

[22] M. Csontos, T. Wojtowicz, X. Liu, M. Dobrowolska, B. Jankó, J. K. Furdyna, and G. Mihály , Phys. Rev. Lett. **95**, 227203 (2005).

[23] M. Csontos, G. Mihály, B. Jankó, T. Wojtowicz, X. Liu, and J. K. Furdyna , Nature Materials **4**, 447 (2005).